Title	Difference in Dachsous Levels between Migrating Cells Coordinates the Direction of Collective Cell Migration(manuscript)
Author(s)	Arata, Masaki; Sugimura, Kaoru; Uemura, Tadashi
Citation	Developmental Cell (2017), 42(5): 479-497
Issue Date	2017-09-11
URL	http://hdl.handle.net/2433/227085
Right	© 2017. This manuscript version is made available under the CC-BY-NC-ND 4.0 license http://creativecommons.org/licenses/by-nc-nd/4.0/; The full-text file will be made open to the public on 11 September 2018 in accordance with publisher's 'Terms and Conditions for Self-Archiving'.; This is not the published version. Please cite only the published version.
Type	Journal Article
Textversion	author

The Difference in Dachsous amounts between migrating cells coordinates the direction of collective cell migration

Masaki Arata,[1] Kaoru Sugimura,[2, 3] and Tadashi Uemura[1, 4]

[1] Graduate School of Biostudies, Kyoto University, Yoshida Konoe-cho, Sakyo-ku, Kyoto, 606-8507, Japan
[2] Institute for Integrated Cell-Material Sciences (WPI-iCeMS), Kyoto University, Yoshida Honmachi, Sakyo-ku, Kyoto, 606-8501, Japan
[3] JST, PRESTO, 5 Sanban-cho, Chiyoda-ku, Tokyo, 102-0075, Japan

Author for correspondence: Tadashi Uemura
Graduate School of Biostudies, Kyoto University, South Campus Research Building (Building G), Kyoto University, Yoshida Konoe-cho, Sakyo-ku, Kyoto 606-8507, Japan
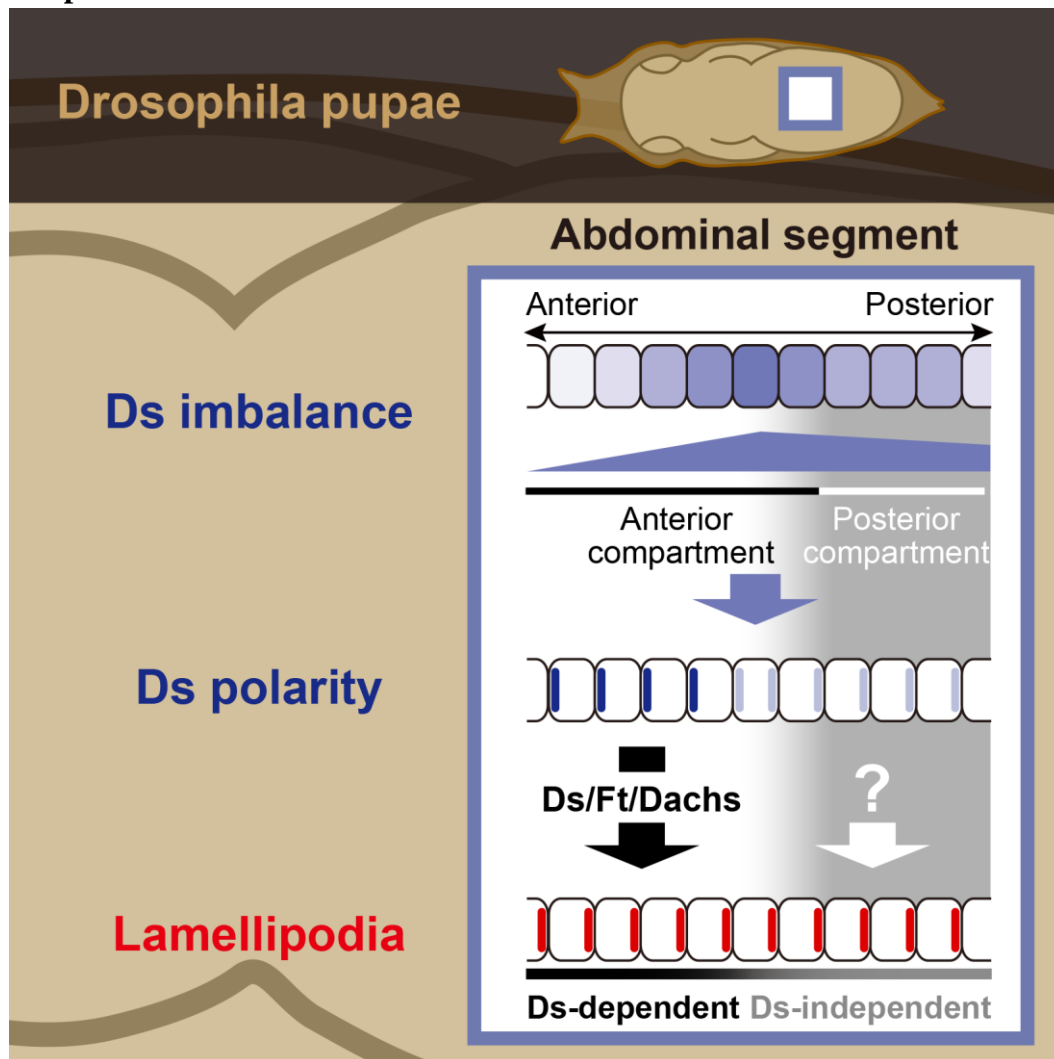(Phone) 81-75-753-9238
(Fax) 81-75-753-4265
(e-mail) tauemura@lif.kyoto-u.ac.jp

[4] Lead Contact

Running Title: Dachsous directs collective cell migration

Graphical abstract

Highlights

- Dachsous (Ds) and Fat cadherins and Dachs myosin control collective cell migration
- The amount of Ds in each migrating cell varies along the axis of migration
- This Ds imbalance polarizes Ds localization, which controls the migratory direction
- Ds and Dachs myosin at the rear restricts lamellipodia to the opposite cell end

eTOC Blurb

Arata et al. proposes a migrating cell group-autonomous mechanism of directing collective migration, where Dachsous and Fat cadherins and Dachs myosin play a pivotal role. The amount of Dachsous in each migrating cell varies along the axis of migration. This Dachsous imbalance polarizes its localization, which coordinates the migratory direction.

Summary

In contrast to extracellular chemotactic gradients, how cell-adhesion molecules contribute to directing cell migration remain more elusive. Here we studied the collective migration of Drosophila larval epidermal cells (LECs) along the anterior-posterior axis, and propose a migrating cell group-autonomous mechanism where an atypical cadherin Dachsous (Ds) plays a pivotal role. In each abdominal segment, the amount of Ds in each LEC varied along the axis of migration (Ds imbalance), which polarized Ds localization at cell boundaries. This Ds polarity was necessary for coordinating the migratory direction. Another atypical cadherin, Fat (Ft), and an unconventional myosin Dachs, both of which bind to Ds, also showed biased cell-boundary localizations, and both were required for the migration. Altogether, we propose that the Ds imbalance within the migrating tissue provides the directional cue, and that this is decoded by Ds-Ft mediated cell-cell contacts, which restricts lamellipodia formation to the posterior end of the cell.

Introduction

        In various developmental contexts, cells migrate together as a unit along the tissue axis. For example, the primordium of the zebrafish lateral line migrates toward the tail, and these migrating cells are tightly associated with each other during migration. Such cell migration of loosely or tightly associated cell groups is defined as collective migration. The direction of collective cell migration is highly regulated during normal development and its misregulation leads to abnormal organogenesis (Friedl and Gilmour 2009; Pocha and Montell 2014). In many tissues, cells sense graded concentrations of attractants and/or repellants in the extracellular environment and orient the direction of cell migration along the gradient (Haeger et al. 2015).

        In addition to such chemotactic mechanisms, direct contacts between migrating cells, which are mediated by cell adhesion molecules, also contribute to the directional migration (Rørth 2012; Mayor and Etienne-Manneville 2016). For instance, the directional migration of neural crest cells in Xenopus or zebrafish requires contact inhibition of locomotion (CIL), where the formation of filopodia or lamellipodia is inhibited at cell-cell contacts and is enhanced at the opposite side of the contacts (Carmona-Fontaine et al. 2008). In the process of CIL, cadherins such as N-cadherin transmit cell contact signals via homophilic binding between their ectodomains (Theveneau et al. 2013).

        Dachsous (Ds) is an evolutionarily conserved atypical cadherin (Clark et al. 1995; Rock et al. 2005; Thomas and Strutt 2012; Sharma and McNeill 2013; Shi et al., 2016). In epithelial cells, Ds is localized at apical cell boundaries and binds to another atypical cadherin Fat (Ft) in a heterophilic fashion (Strutt and Strutt 2002; Ma et al. 2003; Matakatsu and Blair 2004; Ishiuchi et al. 2009). The extracellular domains of Ds and Ft are phosphorylated by a Golgi kinase, Four-jointed (Fj), which modulates Ds-Ft binding (Ishikawa et al. 2008; Sopko et al. 2009; Feng and Irvine 2009; Brittle et al. 2010; Simon et al. 2010). In various tissues, expression of *ds* and *fj* forms counter gradients along the tissue axes in such a way that cells with high *ds* express low *fj* (referred to as the Ds landscape hereafter; Villano and Katz 1995; Zeidler, Perrimon, and Strutt 2000; Yang, Axelrod, and Simon 2002; Ma et al. 2003). Moreover, the imbalance of Ds or Fj amount between cells polarizes the localizations of Ds, Ft, and an unconventional myosin Dachs, which binds to the intracellular domain of Ds, at cell boundaries along the tissue axes (Brittle et al. 2012; Bosveld et al. 2012; Mani et al. 2013; Jolly et al. 2014; Hale et al. 2015).

        Ds is well known for its roles in establishing planar cell polarity (PCP; Adler et al. 1998; Harumoto et al. 2010; Mao et al. 2011; Matis and Axelrod 2013;), orienting cell

divisions and cell rearrangements (Baena-López et al. 2005; Mao et al. 2011; Bosveld et al. 2012), and controlling cell proliferation as an upstream component of the Hippo pathway (Bennett and Harvey 2006; Cho et al. 2006; Silva et al. 2006; Willecke et al. 2008; Degoutin et al. 2013). Furthermore, there is emerging evidence that Ds controls the collective migration of various cell types, including Drosophila larval epidermal cells (LECs; Bischoff 2012), mouse facial branchiomotor (FBM) neurons (Zakaria et al. 2014), epicardial-derived cells (EPDCs) during human heart valve formation (Durst et al. 2015), and pre-chondrogenic mesenchymes during the development of the sternum (Mao et al., 2016). However, the detailed mechanism by which Ds directs the migration of these diverse cell clusters is still unclear. Moreover, it is an open question how similar such Ds-dependent mechanisms are to each other among various types of migrating cells.

To address the above questions, we revisited Drosophila LECs whose Ds-dependent mechanism has not been fully elucidated. LECs cover the entire abdominal surface, which makes LECs suitable for monitoring how Ds regulates the migration by live-cell imaging. During metamorphosis at the pupal stage, they migrate as a group and are eventually replaced by adjacent proliferating histoblast cells that are founders of adult epidermis (Madhavan and Madhavan 1980; Ninov et al. 2010; Bischoff 2012). In the dorsal part of each abdominal segment, LECs first move posteriorly, which depends on Ds, and then they turn dorsally, migrating toward the midline; these movements take place essentially without breaking cell-to-cell adhesion (Bischoff 2012; Figure 1 and Figure S1). LECs produce lamellipodia-like protrusions on their apical surfaces in the direction of their movement (Figure S1A), and it is suggested that these protrusions propel LECs, presumably by generating forces on the apical extracellular matrix, the cuticle (Ninov et al. 2010; Bischoff 2012). It should be emphasized that the entire dorsal LEC sheet moves in the posterior direction and that most of the LECs produce lamellipodia. This anatomical context makes a striking contrast to other well-characterized model systems of collective cell migration such as Drosophila border cells, and the zebrafish lateral line primordium, where a limited number of cells at the leading edge form lamellipodia and propel the movement of the cell cluster (Mayor and Etienne-Manneville 2016; Pocha and Montell 2014; Bussmann and Raz 2015). In this study, we analyzed the Ds-dependent mechanism of the LEC migration in the posterior direction.

Results

Quantitative analysis of LEC movements

To quantitatively characterize LEC movements, we tracked the movements of LEC nuclei around the dorsal midline in abdominal segments A2-A3 (Figure 1A-A" and Figure S1B), and measured the angle, directionality, and velocity of their movements (Figure 1B and S2A-D4). In the wild type pupa, LECs started to move posteriorly at around 24 hours after puparium formation (hr APF); and from approximately 28 hr APF onwards, they moved dorsally (Figure 1C1-C4 and Movie S1; Bischoff 2012). To evaluate how strongly the movements of LECs are aligned in each pupa, we calculated the circular variance of the movement angles (see STAR methods for details). The value of circular variance ranges from 0 (totally unidirectional) to 1 (no bias). We calculated this value for every possible two-hour window within individual recordings and determined the representative two-hour window that scored the minimum value. This time window corresponded to the posterior movement phase in the wild-type LECs (Figure 1E). Therefore, if the posteriorly directed movement is impaired, the value of the minimum circular variance is expected to increase.

Ds is required for the alignment of lamellipodia-dependent cell movement, but not for apoptosis, cell rearrangement, or cell-shape change

To evaluate the contribution of Ds to the LEC movement, *ds* was knocked down in most, if not all, LECs and, by contrast, only rarely in histoblast cells (see details in STAR Methods). We confirmed that the *ds* RNAi line employed in this study reduced the amount of endogenous Ds at cell boundaries of LECs (data not shown). The coordinated posterior movement of LECs was perturbed by the *ds* knockdown, while their dorsal movement was not (compare Figure 1C1-C4 and 1D1-D4, and Figure 1E and 1F; Figure 1G and Movie S1), which was consistent with the previous study (Bischoff 2012). We noticed that some of LECs moved in the opposite anterior direction (cyan tracks in Figure 1D2; also explained later in Figure 6A and A'). Distributions of directionality and velocity are similar between the control and the knockdown during 24-26 hr APF (Figure S2E1 and S2E2), which indicates that *ds*-depleted LECs did not stop moving. We also found that there was no difference in the values of velocity between *ds*-depleted LECs which moved in the anterior direction and those in the posterior direction during 24-26 hr APF (data not shown). During 26-28 hr APF, *ds* knockdown rendered directionality lower than that of control LECs (Figure S2E3), that is, cells moved non-processively.

To provide conclusive evidence that LECs are propelled by the Ds-dependent

migration, we first evaluated the effect of *ds* knockdown on the direction of lamellipodia formation by labeling LECs with a lamellipodia marker. We then ruled out the possibility that Ds is necessary for morphogenetic processes other than cell migration, which could trigger posterior cell movement.

Expression of F-actin markers, such as Lifeact:GFP (Riedl et al. 2008) or Moesin:GFP (Chihara et al. 2003), disrupted the posterior movement of LECs (data not shown), whereas a fusion protein of GFP and the PH domain of Grp1 (GPH; Britton et al. 2002) did not have such an effect. GPH has been shown to label the leading edge of migrating epidermal cells during dorsal closure in the Drosophila embryo (Pickering et al. 2013). We showed that GPH indeed labeled apical protrusions of LECs (Figure S3A and A') and that *ds* knockdown resulted in mislocalized GPH-labelled protrusions in LECs (Movie S2). In addition to GPH, we found a novel landmark for the front-rear cell axis, β-heavy Spectrin (β$_H$-Spec)/Karst (Kst) that is a candidate of Dachs-binding proteins (Kwon et al., 2013; Figure S3). β$_H$-Spec was localized at the rear in the apical domain of each wild-type LEC during migration (Figure S3C1-D4; Movie S3), but not before migration (Figure S3B1-B3). The unidirectional arrangement of the cell axis was significantly disorganized by *ds* knockdown (Figure S3F1-G4). These results suggest that *ds* knockdown abolished the coordinated front-rear polarity of migrating LECs.

Next, we examined whether the posterior movement of LECs was due to translational motion, not to deformation of a tissue around the dorsal midline. Tissue deformation is a summation of division, cell shape change, cell rearrangement, and apoptosis (Guirao et al. 2015). Since LECs are postmitotic, we quantified three other cell behaviors in control or *ds* knockdown cells. We also measured the width of the abdominal segment as an index of tissue deformation. As summarized in Figure S4, none of these indices was significantly affected by *ds* knockdown. However, we visually noticed abnormally elongated cells under the *ds* knockdown condition (yellow cells in Figure S4B'). Since these cells tended to locate along boundaries between cells that migrate oppositely (explained later in Figure 6A and A'), this cell shape change may occur as a result of the divergence of the migration orientations. Furthermore, *ds* overexpressing or knockdown clones did not move posteriorly even when they were surrounded by wild-type LECs (Movie S4). This clone-autonomous abnormal behavior indicates that external pushing or pulling forces, if they are exerted from other parts of the body, such as proliferating histoblast cells, do not play a dominant role in the posterior movement of LECs, at least in A2 and A3 that we observed. Taken together, Ds coordinates the direction of apical lamellipodia and thereby effects the unidirectional posterior migration of LECs.

Ds is localized at the A-P cell boundaries during the posterior migration

In the developing Drosophila wing or notum, Ds localization is polarized along the body axis at cell boundaries, and this promotes directional behavior of cells, such as oriented cell rearrangements (Brittle et al. 2012; Bosveld et al. 2012). We asked whether Ds localization in LECs would be similar; therefore, we monitored the subcellular distribution of Ds during the Ds-dependent phase of LEC migration. In the *ds:EGFP* knock-in strain at 26 hr APF (Brittle et al. 2012), Ds:EGFP signals in migrating LECs were enriched at A-P cell boundaries while they were weak at dorso-ventral (D-V) boundaries (Figure 2A and A'); and this provides a sharp contrast to a more uniform distribution of *D*E-cadherin:GFP at the same stage (Figure 2B and B'; see STAR methods for quantification; Huang et al. 2009). We also noticed that the subcellular localization of Ds:EGFP dynamically changed before and after the onset of the posterior migration (Figure S1E1-E4).

The polarized localization of Ds is required for the posterior migration of LECs

To assess the relevance of the polarized distribution of Ds to the posterior migration of LECs, we attempted to make the Ds distribution less polarized and to analyze how that affected the LEC migration. First, we overexpressed untagged Ds in all LECs of the *ds:EGFP* knock-in strain. Overexpression of untagged Ds severely reduced the amount of Ds:EGFP at cell boundaries, and consequently it was difficult to judge whether the Ds:EGFP distribution became less polarized or not (data not shown). As an alternative, we analyzed the distribution of Ft:EGFP, expressed under its own promotor, as an indirect indicator of Ds localization. In control LECs, the subcellular localization of Ft:EGFP was polarized along the A-P axis (Figure 2C and C'), and *ds* overexpression reduced this bias, which suggests that Ds polarity also became less biased (Figure 2D and D'). This genetic manipulation abrogated the directional collective cell migration (compare Figure 2E1-E3 and 2F1-F3; quantification in Figure 2G).

We then overexpressed the Golgi kinase Four-jointed (Fj; Figure 3), which regulates the binding affinity between Ds and Ft (Ishikawa et al. 2008; Sopko et al. 2009; Feng and Irvine 2009; Brittle et al. 2010; Simon et al. 2010). Neither the Ds polarity nor the posterior migration was affected noticeably when the kinase-dead form of Fj (Fj^{GGG}; Ishikawa et al. 2008) was broadly expressed by a *tubulin-Gal4* driver (Figure 3A, A', and S5A1-A2; compared with Figure 2A, A', and 1C1-C4, respectively). By contrast, overexpression of the wild-type form of Fj (Fj^{WT}) rendered Ds:EGFP less polarized (Figure 3B and B') and impaired the directional migration (Figure 3E, S2E1-E4 and

8

S5B1-C2). The effect of Fj^{WT} OE was similar to that of the *ds* knockdown; that is, Fj^{WT} OE increased the number of LECs moving in the reverse orientation during 24-26 hr (Figure S5B1 and S5C1) and that of cells moving non-processively during 26-28 hr APF (compare Fj^{GGG} OE and Fj^{WT} OE in Figure S2E3). Furthermore, phenotypes of *fj* knockdown were also similar to those of *ds* knockdown, as shown by the fact that both knockdowns alleviated or disrupted the polarized localization of Ft:EGFP (Figure 3C-D' and 7D-E) and reduced directionality during 26-28 hr APF ("Directionality" in Figure 3G-G' and S2E3). Although the circular variance of angles of LEC movements were not significantly increased by the *fj* knockdown (Figure 3F), a cluster of *fj*-depleted LECs migrated in the reverse, anterior direction (cyan tracks in Figure 3I1).

It has been shown that Fj not only regulates Ds polarity but also controls transcriptional activity via the Hippo pathway in the Drosophila wing disc (Cho et al. 2006; Rogulja et al. 2008; Willecke et al. 2008). However, overexpression of Fj^{WT} in LECs did not affect the expression of *Diap1-GFP* (Zhang et al. 2008), one of Hippo pathway target genes, whereas overexpression of the active form of the key Hippo pathway transcriptional coactivator Yorkie did increase *Diap1-GFP* expression (data not shown). Thus, the contribution of Fj^{WT} overexpression to transcriptional regulation is unlikely to explain the uncoordinated migration of LECs. Taken together, our results are consistent with the notion that the polarized localization of Ds at A-P cell boundaries is required for the posterior migration of LECs.

The amount of Ds at A-P cell boundaries reaches a maximum in the middle of the abdominal segment

As noted above, Ds localization in LECs was aligned along the A-P axis. This raised the question of how the global information along the A-P axis is linked to the subcellular localization of Ds. We speculated that *ds* and/or *fj* might be expressed in a graded manner in the epidermis, and that such tissue-wide differential expression patterns might cause the polarized localization of Ds at the A-P cell boundaries, on the basis of what has been shown in the wing disc or notum (Brittle et al. 2012; Bosveld et al. 2012). We examined whether there was in fact such an imbalance in the amounts of Ds between migrating LECs, which we will refer to hereafter as the Ds imbalance (Figure 4 and S6).

We found that, in each abdominal segment of the *ds:EGFP* knock-in strain, Ds:EGFP signals at A-P cell boundaries were stronger in the middle of the segment and weaker towards both anterior and posterior segment borders (Figure 4B; segment borders: yellow broken lines in Figure 4; quantified in Figure 4F1-F3, S6B, and S6E1-F5), while signals of *D*E-cadherin:GFP did not show such an imbalance (Figure 4A; quantified in

9

Figure S6A and S6C1-D5). Visually, we noticed that the anterior slope (referred to as the "uphill" slope) of the Ds imbalance was steeper than the posterior slope ("downhill") in the segment (Figure 4B). We captured images of two adjacent regions that straddled either the segment border or the A-P compartment border (Figure 4C). The Ds:EGFP amounts peaked at a position one-to-two cells anterior to the A-P compartment border (cyan broken lines and cyan arrowheads in Figure 4E-E'), whereas it was minimal or hardly detected at around the segment border (Figure 4D-D', 4F1-F3, S6B, and S6E1-F5). To summarize, each segment provides an A-to-P triangle wave-like Ds:EGFP landscape, with the amounts of Ds:EGFP rising with a steep uphill, peaking in the middle of the segment, then falling off with a shallow downhill ("Ds imbalance" in Figure 4G). This Ds landscape in LECs is reminiscent of that in histoblast-derived adult abdominal epidermis (Casal et al. 2002). We also found that the localization of EGFP-Dach myosin (EGFP-Dachs; Brittle et al., 2012) was polarized at opposite cell edges in the anterior and posterior compartments (Figure 4H1-H3 and S7H1-H3). Since it is widely accepted that the imbalance of Ds is necessary and sufficient for the polarized distribution of Dachs myosin (Mao et al. 2006; Rogulja et al. 2008), this observation supports our documentation of the endogenous Ds imbalance.

We addressed whether this Ds landscape was generated at the transcriptional level by using *ds* enhancer trap lines (*ds-GAL4*: Matakatsu and Blair 2006; *ds-lacZ*: Spradling et al. 1999). We attempted to detect mCD8:3xEGFP expressed by *ds-GAL4* or *β*-Gal made from *ds-lacZ*; however, imaging signals in those LECs were technically challenging due to weak EGFP signals and high backgrounds with immunohistochemistry (data not shown). Therefore, we could not establish whether graded transcription of *ds* exists in LECs. However, regarding *fj* expression, we could confirm that the *fj* expression level was high around the segment borders by using the *fj-Gal4* line (*fj^{VG1}*; Tang and Sun 2002; Figure S5D1-E4), which was largely complementary to the Ds landscape (Figure S5F-H).

With the ascending and descending slopes of the Ds amount within the segment in mind, we sought to determine whether Ds is preferentially located at the anterior and/or posterior boundaries in each posteriorly-migrating LEC (Figure S7). We found that in the anterior uphill region (Figure S7C1-E4), Ds:EGFP was enriched at the anterior cell boundaries, which corresponds to the rear of the migrating LECs (Figure S7C4, D4, and E4; illustrated in "Ds polarity" in Figure 7I). In the posterior shallow downhill region (Figure S7F1-G4), Ds:EGFP appeared to be slightly more abundant on the posterior cell boundaries (Figure S7F4 and G4), although our analysis could not provide definitive proof. The localization of EGFP-Dachs, which binds to the intracellular domain of Ds, at

10

opposite cell edges in the anterior and posterior compartments also supports our results of Ds localization (Figure 4H1-H3 and S7H1-H3).

Ectopic imbalance of Ds repolarizes the distribution of Ds

At this point, our model for Ds-dependent posterior migration of LECs can be summarized as follows (Figure 7I): [1] Along the A-P axis in each segment, there is an imbalance in the amount of Ds between LECs ("Ds imbalance" in Figure 4G and 7I). [2] This imbalance polarizes the distribution of Ds ("Ds polarity" in Figure 7I). [3] The Ds polarity biases the emergence of lamellipodia at the posterior cell boundary, driving the posterior migration (the bottom of Figure 7I). So far, our results show the necessity for the causal relationship in our model. However, three obvious questions needed to be addressed. First, is the imbalance of Ds sufficient to polarize the Ds distribution and direction of migration? Second, if the Ds imbalance governs the direction of migration, how do LECs in both the A-to-P uphill region and those in the downhill region migrate in the same (posterior) direction? Third, what are the molecular mechanisms that link Ds polarity and the direction of lamellipodia formation?

To examine the sufficiency of the Ds imbalance, we generated an ectopic imbalance along the D-V axis that is perpendicular to the intrinsic axis, and analyzed its effect on Ds localization in adjacent LECs and their migration. In LECs that are dorsally adjacent to Ds-overexpressing LECs, Ds:EGFP and Dachs:GFP were ectopically enriched at D-V cell boundaries (arrows in Figure 5A1-A4 and 5B-E3), consistent with the notion that the Ds imbalance was sufficient to repolarize Ds in adjacent cells. Next, we assessed the effect on LEC migration (Figure 5F1-F6"). We could at least find within the clones that (1) some LECs showed decreased directionalities (blue and magenta particles in Figure 5F4) compared to the comparable regions in the contralateral side and (2) some LECs migrated up on the ectopic hill of Ds, away from the midline (yellow tracks in Figure 5F6-F6", the enlarged view of 5F5; see also the legend), which is the reverse orientation of the wild-type cells. However, this was not always the case: other cells migrated in the posterior direction, similar to the control situation (data not shown; discussed later).

A subset of LECs in the anterior compartment depend on Ds for their posterior migration, but LECs in the posterior compartment do not

We then addressed how both LECs on the uphill and those on the downhill sides of the Ds imbalance moved in the same posterior direction. When we re-examined the migration phenotype of the *ds* knockdown carefully (Figure 1D2), we noticed that the

11

defect in the posterior migration appeared to be regionally restricted within each segment. This suggests the possibility that a subset of LECs migrate in a Ds-dependent manner. If so, where do these Ds-dependent LECs locate within each abdominal segment? We knocked down *ds* in most, if not all LECs, and mapped LECs that migrated posteriorly within the segment, and those that did not (Figure 6A–A'; see details in the legend). Notably, a subset of LECs that were located posterior to the segment border migrated in the opposite anterior direction (blue cells in Figure 6A'; cells possibly just around the segment border are marked with yellow dots in Figure 6A-A').

Additionally, we performed a region-selective knockdown of *ds* by using *engrailed* (*en*)-*GAL4* or *pannier* (*pnr*)-*GAL4*. *en-GAL4* drives transgene expression in the posterior compartment (the *en* domain), while LECs expressing *pnr-GAL4* (*pnr* domain) straddle the A-P compartment border and comprise a large subset of the anterior compartment (Figure 6B and S1F1-F3). LECs depleted of Ds still migrated posteriorly within the *en* domains (Figure 6C1-C4 and Movie S5). By contrast, the results of *ds* knockdown in the *pnr* domains were intriguing (Figure 6D1-D4): the posterior edge of the *pnr* domain, which belongs to the P compartment, did move posteriorly irrespective of the knockdown (magenta dotted lines in Figure 6D1-6D4), whereas the anterior edge of the *pnr* domain either did not move as well or moved in the opposite direction (green dotted lines in Figure 6D1-6D4; see also Movie S6). Although *ds* knockdown in the *pnr* domain seemed to narrow the domain along the A-P axis (compare Figure 6D3 and 6D4), the spatial relationship between the *pnr* domain and the *en* domain was unaffected (data not shown).

These results, when superimposed on those presented in Figure 4G, indicate that each abdominal segment consists of two distinct types of LECs: Ds-dependent cells (a subset of LECs in the anterior compartment; unshaded cells in Figure 7I), which presumably overlap with the steep uphill of the Ds imbalance, and those that do not require Ds in their posterior migration (LECs at least in the posterior compartment; shaded cells in Figure 7I). It should be noted that we did not identify the exact border between the Ds-dependent and Ds-independent LECs; nonetheless, our analyses at least roughly mapped the border relative to the *en* and *pnr* domains in the segment. Two isoforms of a core PCP protein, Spiny-legs (Sple) and Prickle (Pk) contribute to the difference in the Ds dependent and independent establishment of PCP (Ayukawa et al., 2014; Olofsson et al., 2014; Merkel et al., 2014; Ambegaonkar and Irvine, 2015). We hypothesized that a similar Sple/Pk dependent mechanism underlies the difference between the Ds-dependent and independent migration of LECs. However, none of our experimental results strongly supported this hypothesis (see details in the legend of Figure

S1C).

Molecular mechanism of Ds-dependent migration

Our final question was how the polarized distribution of Ds directs lamellipodia formation. To address this question, we searched for candidate molecules that potentially participate in the Ds-dependent migration. These candidates belong to four categories: Ds binding proteins, including Ft and Dachs (Strutt and Strutt 2002; Ma et al. 2003; Matakatsu and Blair 2004; Ishiuchi et al. 2009; Tsukasaki et al. 2014; Bosveld et al. 2012); core PCP proteins (Adler et al., 1998; Lawrence and Casal 2013; Vladar et al. 2009; Goodrich and Strutt 2011; Vichas and Zallen 2011; Wallingford 2012); components of the Hippo pathway downstream of Ds, Ft, and Dachs (Bennett and Harvey 2006; Cho et al. 2006; Silva et al. 2006; Willecke et al. 2006); and phosphatidyl inositol (3,4,5)-triphosphate (PIP3) kinase. Some core PCP proteins and Hippo pathway components are not only related to Ds functionally, but are also known to regulate the collective migration of border cells in the Drosophila egg chamber (Bastock and Strutt 2007; Lucas et al. 2013; Lin et al. 2014).

Knockdown of *ft* or *dachs* disrupted the posterior migration as severely as the *ds* knockdown (*ft* RNAi and *dachs* RNAi in Figure 7A). Intriguingly, a subset of LECs did migrate in the normal posterior direction (Movie S7), as we showed under the *ds* knockdown condition (Figure 6A and A'). Dachs:GFP that was expressed by its own promotor (Bosveld et al. 2012) was enriched at the A-P cell boundaries of posteriorly migrating LECs (Figure 7B and B'), much as Ds:EGFP and Ft:EGFP were (Figure 2A and 2C). Ds recruits Dachs to the same plasma membrane domain but is not required for the membrane localization of Dachs per se (Bosveld et al. 2012; Brittle et al. 2012). As expected, when *ds* was knocked down, tight localization of Ft:EGFP at cell boundaries was lost (Figure 7D and E) and Dachs:GFP was uniformly distributed at all cell boundaries (Figure 7B-C'). In addition, ectopic imbalance of Ds repolarized the subcellular localization of Dachs (Figure 5B-E3). Moreover, we focused on the published interactome data of the Hippo signaling pathway that includes Ds, Ft, and Dachs myosin, and in particular the list of candidate proteins that bind to Dachs myosin (Kwon et al., 2013). We knocked down a total of 10 genes (see the STAR methods) individually to search for those that are necessary for the directional migration of LECs. However, none of those knockdowns disrupted the LEC migration (data not shown).

The knockdown phenotype of a core PCP gene *frizzled* (*fz*) was variable (*fz* RNAi in Figure 7A), and *fz* overexpression did not disrupt LEC migration (*fz* OE in Figure 7A). We also studied the subcellular localization of another core PCP protein, Flamingo (Fmi),

the Drosophila seven-pass transmembrane cadherin (Usui et al. 1999; Harumoto et al. 2010) in the wild-type migrating LECs, and found that its distribution was not polarized at cell boundaries during the posterior migration (data not shown). These results suggest that core PCP proteins are not involved in the posterior migration of LECs. Moreover, knockdown of Hippo pathway components did not interfere with the posterior migration (*wts*, *hpo* and *yki* RNAi in Figure 7A).

As shown above, we found that a PIP3 reporter, GPH, labeled apical protrusions at the front of LECs (Figure S3A-A') and that a *ds* knockdown resulted in mislocalized GPH-labeled protrusions in LECs (Movie S2). In *Dictyostelium* and neutrophils, it has been widely accepted that actin protrusions are formed at the cell edge where the PIP3 level is the highest (Iijima and Devreotes, 2002; Funamoto et al., 2002), and that polarization of PIP3 within the cell results from spatial variations in the activity of PI3K (phosphatidylinositol-3 kinase). Taken together, we came up with a plausible idea that Ds and Dachs myosin may control the subcellular distribution or the activity of PI3K in migrating LECs. We misexpressed an active version (PI3K-CAAX) or a dominant negative form (PI3K^{DN}) of PI3K (Leevers et al., 1996) in LECs and found that both variants affected the posterior migration of LECs (PI3K-CAAX OE and PI3K^{DN} OE in Figure 7A and Figure 7F1-H4). PI3K-CAAX or PI3K^{DN} misexpression abrogated the posterior migration of LECs irrespective of whether they locate in the anterior or the posterior compartment (indicated by white boxes in Figure 7G1-G2 or 7H2-H3). In particular, misexpression of PI3K^{DN} remarkably decreased velocities, which means cells stopped moving (PI3K^{DN} OE in Figure S2E2 and S2E4). This finding is consistent with the notion that the PI3K system acts as the effector in the collective migration of LECs. Although we addressed whether PI3K is localized in migrating LECs by visualizing the EGFP-tagged regulatory subunit, PI3K-p60 (Sarov et al., 2016), the localization of PI3K-p60 at cell boundaries was not polarized along the A-P axis in the wild-type LECs, in contradistinction to Ds/Ft/Dachs (data not shown). We would like to interpret this observation carefully, because it has not been verified whether this PI3K-p60 fusion protein is functional or not.

Taken together, we propose that the segment-wide slope of the Ds imbalance within migrating LECs polarizes the subcellular distribution of Ds/Ft/Dachs and the polarized distribution of Ds/Ft/Dachs biases the activity or the distribution of PI3K in each LEC, thereby restricting the formation of lamellipodia to the posterior edge (Figure 7I).

Discussion

Ds-dependent directional information resides within migrating LECs

One classic view of the underlying mechanism directing collective cell migration is that an extracellular chemotactic gradient dictates the migratory direction (Haeger et al. 2015). Our study on the directional migration of LECs has revealed a novel mechanism: the Ds-dependent directional information resides selectively within the migrating cells. Specifically, it is the imbalance of the amount of Ds in each abdominal segment (the Ds landscape) that provides the directional cue, which is decoded by Ds-Ft mediated direct cell-cell contacts.

It has been shown that Ds plays an important role in shaping various organs or tissues in both Drosophila and vertebrates (Aigouy et al. 2010; Bosveld et al. 2012; Mao et al. 2011; Cappello et al. 2013; Zakaria et al. 2014; Bagherie-Lachidan et al. 2015; Durst et al. 2015; Mao et al. 2016), and that morphogenesis of at least some of those is primarily mediated by Ds-dependent collective cell migration. Examples include migration of four cell types: mouse facial branchiomotor (FBM) neurons (Zakaria et al. 2014), epicardial-derived cells (EPDCs) during human heart valve formation (Durst et al. 2015), sternal cells (Mao et al., 2016) and LECs (Bischoff 2012 and this study). An advantage of the LEC system is better access to *in vivo* live imaging, which allowed us to perform quantitative analyses of the Ds-dependent migration at subcellular, cellular, and tissue levels. Our results highlight the apparent mechanistic differences among the above four distinct contexts of Ds-dependent migration. First, the Ds imbalance resides within migrating LECs and sternal cells themselves, whereas FBM neurons and EPDCs migrate into and within other cells that exhibit imbalances of the Ds ortholog, Dchs1. Second, we found that the localization of Ds is polarized at cell boundaries along the body axis in LECs, but such polarity has not been directly visualized in other contexts of Ds imbalance-dependent migration. Third, with respect to the direction of migration, LECs and valve cells migrate toward Ds/Dchs1-high cells, while FBM neurons migrate toward Dchs1-low cells and sternal cells undergo directed intercalation along a Dchs1 gradient. Finally, regarding the molecular machinery, Drosophila Dachs is not conserved in mammals, although it is possible that there is an alternative counterpart. In spite of the above differences, the key common feature of the four distinct developmental contexts would be the imbalance of the Ds amount between adjacent cells. Intriguingly, the migration of FBM neurons requires the Ds imbalance in the surrounding neuroepithelium (Zakaria et al., 2014), implying that the manner in which the Ds/Dchs1 imbalance is decoded to fix the migratory direction may depend on the cell type.

15

In this study, we also showed that the Ds imbalance between LECs in normal development was necessary for the posterior migration. However, when we generated an artificial imbalance of Ds along the dorsal-ventral axis, we could not show conclusively that such an ectopic imbalance sufficiently reorients LEC migration: some of the adjacent cells migrated towards the Ds-overexpressing LECs, but others did not. In larval epidermis, the effect of clonal Ds overexpression on reorienting cells has been tested by using the polarity of denticles (actin filament-rich apical cell protrusions) as a readout (Repiso et al. 2010; Rovira et al. 2015). The conclusion drawn from those experiments was that its effect does not propagate over multiple cells, but is restricted to adjacent cells (Rovira et al. 2015). Furthermore, even if Ds is mislocalized in a cell, the orientation of lamellipodia could be corrected by neighbors that migrate in the normal orientation. This assumption is based on previous reports that mechanical cues direct the front-rear polarization of cells (Ladoux et al., 2016). Therefore, if only the cells adjacent to the Ds-overexpressing LECs were subject to the ectopic Ds imbalance in our experiment, such reoriented movements might be difficult to detect.

How is the movement of LECs coordinated throughout the large epidermal sheet?

In vitro wound healing assays with cultured cells revealed how the leading edge cells drag a relatively passive mass of follower cells, how the followers respond to the forces exerted by the leading cells, and how the followers also participate in generating pulling forces (Mayor and Etienne-Manneville 2016; Das et al. 2015; Ladoux et al., 2016). In one of these *in vitro* assays, the migration of an epithelial monolayer was well coordinated over a distance of about 200µm (Angelini et al. 2010; Petitjean et al. 2010; Das et al. 2015). By contrast, our system actually comprised the movement of the entire abdominal epidermis, which reaches up to 2-3 mm along the A-P axis. Therefore, the traction force exerted by a small number of cells, such as those at the posterior-end of the abdomen, would likely be insufficient to coordinate the movements of LECs. How then do LECs move as a whole and achieve such a long-range coordination of the movement? One important feature would be that most of the LECs produce lamellipodia and move actively (Bischoff 2012). Another would be segmentation: a large group of cells is separated into several segments along the A-P axis, and the coordination of cell movement is achieved in each segment by the triangle wave-like Ds landscape.

Our novel finding is that LECs comprise two spatially segregated populations of LECs that possess mechanistically distinct propelling devices. One population of LECs is located in the anterior compartment and orients their lamellipodia in a Ds-dependent manner, whereas the other population orients their lamellipodia by an unknown, Ds-

independent mechanism. This bimodal system is reminiscent of the PCP system in the adult abdomen. Abdominal epithelial cells in the tergites produce hair-like structures (trichomes) at their apical surfaces, and these trichomes are pointed posteriorly. Between the anterior and posterior compartment in each abdominal segment, the polarization of trichomes is dependent on distinct protein isoforms that are made from the *pk-sple* locus (Casal et al. 2002; Lawrence et al. 2004; Casal et al. 2006; Ayukawa et al. 2014; Ambegaonkar and Irvine 2015). In the context of the posterior migration, a subset of LECs may have developed the Ds-dependent engine by taking advantage of their location in the steep uphill slope of the Ds landscape. By contrast, LECs in the other region in the segment (the shallow downhill slope) may not be able to use the Ds engine, but rely on a distinct propelling device. This similarity between the mechanisms underlying the abdominal PCP and LEC migration might suggest that such an alternate arrangement of two (or more) different cell types is helpful for the long-range coordination of orienting cells.

Molecular mechanisms of the Ds dependent migration

Our results suggest that Ds is localized at the rear (the anterior cell boundary) in each of the migrating LECs, and it controls lamellipodia formation. But how? We identified Dachs as a possible effector of Ds-dependent migration. *In vivo*, a biased distribution of Dachs, which binds to the intracellular domain of Ds, generates anisotropy of tension at cell boundaries and contributes to the oriented cell rearrangements (Bosveld et al. 2012). Interestingly, it has been reported that membrane tension inhibits the formation of protrusions (Keren et al. 2008; Houk et al. 2012; Reffay et al. 2014). Taken together, one possible role of Dachs in the LEC migration would be that Dachs increases the junction tension at the rear of LECs and inhibits the formation of lamellipodia. However, the rear of a LEC is attached to the front of an adjacent LEC. If Dachs increases the junction tension at the rear of a LEC, it should simultaneously increase the tension at the front of a neighbor. Therefore, Dachs may play other roles in LEC migration. *In vitro* analysis suggests that Dachs acts as a scaffold protein but not as a molecular motor (Cao et al. 2014). One naive hypothesis would be that Dachs at the one end of a LEC (the future rear) biases the distribution of other molecules that inhibit or promote lamellipodia formation. One such candidate is PI3K (Figure 7). In *Dictyostelium* and neutrophils, actin protrusions are formed at the cell edge where the PIP3 level is the highest (Iijima and Devreotes, 2002; Funamoto et al., 2002), and that polarization of PIP3 within the cell results from spatial variations in the activity of PI3K. Full dissection of the molecular mechanism that connects Ds/Ft/Dachs to PI3K awaits future studies.

17

Our study sheds light on the migrating cell group-autonomous mechanism of directing collective cell migration. Such a system, in principle, would be able to achieve a robust unidirectional movement of cells without a requirement of extracellular guidance cues, although we do not deny a contribution of such hypothetical cues in the posterior migration of LECs. The migrating cell group-autonomous mechanism might underlie other developmental contexts with special geometry, where extracellular cues might be ineffective to orchestrate collective migration, such as tissue rotation (e.g. Drosophila ovarian follicle epithelial cells; Haigo and Bilder 2011; Cetera and Horne-Badovinac 2015; Aurich and Dahmann 2016). Intriguingly, *ds* is expressed in gradients in many tissues (Thomas and Strutt 2012; Rock et al. 2005; Mao et al. 2011). Therefore, it will be interesting to investigate whether the Ds imbalance-dependent and migrating cell group-autonomous mechanism underlies the morphogenesis of other organs, and it should be clarified whether the imbalance resides within and/or outside of the migrating groups.

Author contributions

MA and KS, conception and design, acquisition of data (contribution of KS is Figure 6A-A' and S4), analysis and interpretation of data, drafting the article. TU, conception and design, analysis and interpretation of data, drafting the article.

References

Adler, P.N. Charlton, J., and Liu, J. (1998). Mutations in the cadherin superfamily member gene dachsous cause a tissue polarity phenotype by altering frizzled signaling. Development *125*, 959–968.

Aigouy, B. Farhadifar, R., Staple, D.B., Sagner, A., Röper, J.C., Jülicher, F., and Eaton, S. (2010). Cell Flow Reorients the Axis of Planar Polarity in the Wing Epithelium of Drosophila. Cell *142*, 773–786.

Ambegaonkar, A.A., and Irvine, K.D. (2015). Coordination of planar cell polarity pathways through Spiny legs. eLife *4*, e09946.

Angelini, T.E., Hannezo, E., Trepat, X., Fredberg, J.J., and Weitz, D.A. (2010). Cell migration driven by cooperative substrate deformation patterns. Phys. Rev. Lett. *104*, 1–4.

Aurich, F., and Dahmann, C. (2016). A Mutation in fat2 Uncouples Tissue Elongation from Global Tissue Rotation. Cell Rep. *14*, 2503–2510.

Ayukawa, T., Akiyama, M., Mummery-Widmer, J.L., Stoeger, T., Sasaki, J., Knoblich, J. a, Senoo, H., Sasaki, T., and Yamazaki, M. (2014). Dachsous-Dependent Asymmetric Localization of Spiny-Legs Determines Planar Cell Polarity Orientation in Drosophila. Cell Rep. *8*, 610–621.

Baena-López, L.A., Baonza, A., and García-Bellido, A. (2005). The orientation of cell divisions determines the shape of Drosophila organs. Curr. Biol. *15*, 1640–1644.

Bagherie-Lachidan, M., Reginensi, A., Zaveri, H.P., Scott, D.A., Helmbacher, F., and McNeill, H. (2015). Stromal Fat4 acts non-autonomously with Dachsous1/2 to restrict the nephron progenitor pool. Development *142*, 2564–73.

Bastock, R., and Strutt, D. (2007). The planar polarity pathway promotes coordinated cell migration during Drosophila oogenesis. Development *134*, 3055–3064.

Bennett, F.C., and Harvey, K.F. (2006). Fat Cadherin Modulates Organ Size in Drosophila via the Salvador/Warts/Hippo Signaling Pathway. Curr. Biol. *16*, 2101–2110.

Bischoff, M. (2012). Lamellipodia-based migrations of larval epithelial cells are required for normal closure of the adult epidermis of Drosophila. Dev. Biol. *363*, 179–190.

Bosveld, F., Bonnet, I., Guirao, B., Tlili, S., Wang, Z., Petitalot, A., Marchand, R., Bardet, P.-L., Marcq, P., Graner, F., and Bellaiche, Y. (2012). Mechanical Control of Morphogenesis by Fat/Dachsous/Four-Jointed Planar Cell Polarity Pathway. Science. *336*, 724–727.

Boutros, M., Mihaly, J., Bouwmeester, T., and Mlodzik, M. (2000). Signaling specificity by Frizzled receptors in Drosophila. Science *288*, 1825–1828.

Brittle, A., Thomas, C., and Strutt, D. (2012). Planar polarity specification through asymmetric subcellular localization of fat and dachsous. Curr. Biol. *22*, 907–914.

Brittle, A.L., Repiso, A., Casal, J., Lawrence, P.A., and Strutt, D. (2010). Four-jointed modulates growth and planar polarity by reducing the affinity of dachsous for fat. Curr. Biol. *20*, 803–10.

Britton, J.S., Lockwood, W.K., Li, L., Cohen, S.M., and Edgar, B.A. (2002). Drosophila's insulin/PI3-kinase pathway coordinates cellular metabolism with nutritional conditions. Dev. Cell *2*, 239–249.

Buckles, G.R., Rauskolb, C., Villano, J.L., Katz, F.N. (2001). Four-jointed interacts with dachs, abelson and enabled and feeds back onto the Notch pathway to affect growth and segmentation in the Drosophila leg. Development *128*, 3533–3542.

Bussmann, J., and Raz, E. (2015). Chemokine-guided cell migration and motility in zebrafish development. EMBO J. *34*, 1309–1318.

Buszczak, M., Paterno, S., Lighthouse, D., Bachman, J., Planck, J., Owen, S., Skora, A.D., Nystul, T.G., Ohlstein, B., Allen, A., et al. (2007). The carnegie protein trap library: A versatile tool for drosophila developmental studies. Genetics *175*, 1505–1531.

Calleja, M., Moreno, E., Pelaz, S., and Morata, G. (1996). Visualization of gene expression in living adult Drosophila. Science *274*, 252–255.

Cao, Y., White, H.D., and Li, X.-D. (2014). Drosophila myosin-XX functions as an actin-binding protein to facilitate the interaction between Zyx102 and actin. Biochemistry *53*, 350–60.

Cappello, S., Gray, M.J., Badouel, C., Lange, S., Einsiedler, M., Srour, M., Chitayat, D., Hamdan, F.F., Jenkins, Z. a, Morgan, T., et al. (2013). Mutations in genes encoding the cadherin receptor-ligand pair DCHS1 and FAT4 disrupt cerebral cortical development. Nat. Genet. *45*, 1300–8.

Carmona-Fontaine, C., Matthews, H.K., Kuriyama, S., Moreno, M., Dunn, G.A., Parsons, M., Stern, C.D., and Mayor, R. (2008). Contact inhibition of locomotion in vivo controls neural crest directional migration. Nature *456*, 957–61.

Casal, J., Lawrence, P.A., and Struhl, G. (2006). Two separate molecular systems, Dachsous/Fat and Starry night/Frizzled, act independently to confer planar cell polarity. Development *133*, 4561–4572.

Casal, J., Struhl, G., and Lawrence, P.A. (2002). Developmental compartments and planar polarity in Drosophila. Curr. Biol. *12*, 1189–1198.

Cetera, M., and Horne-Badovinac, S. (2015). Round and round gets you somewhere: collective cell migration and planar polarity in elongating Drosophila egg chambers. Curr. Opin. Genet. Dev. *32*, 10–15.

Chihara, T., Kato, K., Taniguchi, M., Ng, J., and Hayashi, S. (2003). Rac promotes epithelial cell rearrangement during tracheal tubulogenesis in Drosophila. Development *130*, 1419–1428.

Cho, E., Feng, Y., Rauskolb, C., Maitra, S., Fehon, R., and Irvine, K.D. (2006). Delineation of a Fat tumor suppressor pathway. Nat. Genet. *38*, 1142–1150.

Chou, T.B., and Perrimon, N. (1996). The autosomal FLP-DFS technique for generating germline mosaics in Drosophila melanogaster. Genetics *144*, 1673–1679.

Clark, H.F., Brentrup, D., Schneitz, K., Bieber, A., Goodman, C., and Noll, M. (1995). Dachsous encodes a member of the cadherin superfamily that controls imaginai disc morphogenesis in Drosophila. Genes Dev. *9*, 1530–1542.

Clarkson, M., R. Saint. (1999). A His2AvDGFP fusion gene complements a lethal His2AvD mutant allele and provides an in vivo marker for Drosophila chromosome behavior. DNA Cell Biol. *18*, 457–462.

Classen, A.-K., Aigouy, B., Giangrande, A., and Eaton, S. (2008). Imaging Drosophila pupal wing morphogenesis. Methods in Molecular Biology (Clifton, N.J.) *420*, 265–275.

Das, T., Safferling, K., Rausch, S., Grabe, N., Boehm, H., and Spatz, J.P. (2015). A molecular mechanotransduction pathway regulates collective migration of epithelial cells. Nat Cell Biol *17*, 276–287.

Degoutin, J.L., Milton, C.C., Yu, E., Tipping, M., Bosveld, F., Yang, L., Bellaiche, Y., Veraksa, A., and Harvey, K.F. (2013). Riquiqui and minibrain are regulators of the hippo pathway downstream of Dachsous. Nat. Cell Biol. *15*, 1176–85.

Durst, R., Sauls, K., Peal, D.S., deVlaming, A., Toomer, K., Leyne, M., Salani, M., Talkowski, M.E., Brand, H., Perrocheau, M., et al. (2015). Mutations in DCHS1 cause mitral valve prolapse. Nature *525*, 109-13.

Feng, Y., and Irvine, K.D. (2009). Processing and phosphorylation of the Fat receptor. Proc. Natl. Acad. Sci. U. S. A. *106*, 11989–94.

Funamoto, S., Meili, R., Lee, S., Parry, L., and Firtel, R.A. (2002). Spatial and temporal regulation of 3-phosphoinositides by PI 3-kinase and PTEN mediates chemotaxis. Cell *109*, 611–623.

Friedl, P., and Gilmour, D. (2009). Collective cell migration in morphogenesis, regeneration and cancer. Nat. Rev. Mol. Cell Biol. *10*, 445–457.

Gates, J. (2012). Drosophila egg chamber elongation: insights into how tissues and organs are shaped. Fly (Austin). *6*, 213–227.

Goodrich, L.V., and Strutt, D., (2011). Principles of planar polarity in animal development. Development *138*, 1877–1892.

Gubb, D., Green, C., Huen, D., Coulson, D., Johnson, G., Tree, D., Collier, S., and Roote,

J. (1999). The balance between isoforms of the Prickle LIM domain protein is critical for planar polarity in Drosophila imaginal discs. Genes Dev. *13*, 2315–2327.

Guirao, B., Rigaud, S.U., Bosveld, F., Bailles, A., Lopez-Gay, J., Ishihara, S., Sugimura, K., Graner, F., and Bellaïche, Y. (2015). Unified quantitative characterization of epithelial tissue development. eLife *4*, e08519.

Haeger, A., Wolf, K., Zegers, M.M., and Friedl, P. (2015). Collective cell migration: Guidance principles and hierarchies. Trends Cell Biol. *25*, 556–566.

Haigo, S.L., and Bilder, D., (2011). Global tissue revolutions in a morphogenetic movement controlling elongation. Science *331*, 1071–1074.

Hale, R., Brittle, A.L., Fisher, K.H., Monk, N. A M, and Strutt, D., (2015). Cellular interpretation of the long-range gradient of Four-jointed activity in the Drosophila wing. eLife *4*, e05789.

Harumoto, T., Ito, M., Shimada, Y., Kobayashi, T.J., Ueda, H.R., Lu, B., and Uemura, T. (2010). Atypical cadherins dachsous and fat control dynamics of noncentrosomal microtubules in planar cell polarity. Dev. Cell *19*, 389–401.

Hayashi, S., Ito, K., Sado, Y., Taniguchi, M., Akimoto, A., Takeuchi, H., Aigaki, T., Matsuzaki, F., Nakagoshi, H., Tanimura, T., Ueda, R., Uemura, T., Yoshihara, M., and Goto, S. (2002). GETDB, a database compiling expression patterns and molecular locations of a collection of gal4 enhancer traps. Genesis *34*, 58–61.

Houk, A.R., Jilkine, A., Mejean, C.O., Boltyanskiy, R., Dufresne, E.R., Angenent, S.B., Altschuler, S.J., Wu, L.F., and Weiner, O.D. (2012). Membrane tension maintains cell polarity by confining signals to the leading edge during neutrophil migration. Cell *148*, 175–88.

Huang, J., Zhou, W., Dong, W., Watson, A.M., and Hong, Y. (2009). From the Cover: Directed, efficient, and versatile modifications of the Drosophila genome by genomic engineering. Proc. Natl. Acad. Sci. U. S. A. *106*, 8284–8289.

Iijima, M., and Devreotes, P. (2002). Tumor suppressor PTEN mediates sensing of chemoattractant gradients. Cell *109*, 599–610.

Ishikawa, H.O., Takeuchi, H., Haltiwanger, R.S., and Irvine, K.D. (2008). Four-jointed Is a Golgi Kinase That Phosphorylates a Subset of Cadherin Domains. Science *321*, 401–404.

Ishiuchi, T., Misaki, K., Yonemura, S., Takeichi, M., and Tanoue, T. (2009). Mammalian Fat and Dachsous cadherins regulate apical membrane organization in the embryonic cerebral cortex. J. Cell Biol. *185*, 959–967.

Ito, K., Awano, W., Suzuki, K., Hiromi, Y., and Yamamoto, D. (1997). The Drosophila mushroom body is a quadruple structure of clonal units each of which contains a virtually

identical set of neurones and glial cells. Development *124*, 761–771.

Jolly, M.K., Rizvi, M.S., Kumar, A., and Sinha, P. (2014). Mathematical modeling of sub-cellular asymmetry of fat-dachsous heterodimer for generation of planar cell polarity. PLoS One *9*, e97641.

Kakihara, K., Shinmyozu, K., Kato, K., Wada, H., and Hayashi, S. (2008). Conversion of plasma membrane topology during epithelial tube connection requires Arf-like 3 small GTPase in Drosophila. Mech. Dev. *125*, 325–336.

Kamei, Y., Suzuki, M., Watanabe, K., Fujimori, K., Kawasaki, T., Deguchi, T., Yoneda, Y., Todo, T., Takagi, S., Funatsu, T., and Yuba, S. (2009). Infrared laser-mediated gene induction in targeted single cells in vivo. Nat. Methods *6*, 79–81.

Keren, K., Pincus, Z., Allen, G.M., Barnhart, E.L., Marriott, G., Mogilner, A., and Theriot, J. A. (2008). Mechanism of shape determination in motile cells. Nature *453*, 475–480.

Koto, A., Kuranaga, E., and Miura, M. (2009). Temporal regulation of Drosophila IAP1 determines caspase functions in sensory organ development. J. Cell Biol. *187*, 219–231.

Kwon, Y., Vinayagam, A., Sun, X., Dephoure, N., Gygi, S.P., Hong, P., and Perrimon, N. (2013). The Hippo signaling pathway interactome. Science *342*, 737–40.

Ladoux, B., Mège, R., and Trepat, X. (2016). Front–Rear Polarization by Mechanical Cues: From Single Cells to Tissues. Trends Cell Biol. *26*, 420–433.

Lawrence, P. A., Casal, J., and Struhl, G. (2004). Cell interactions and planar polarity in the abdominal epidermis of Drosophila. Development *131*, 4651–4664.

Lawrence, P.A., and Casal, J. (2013). The mechanisms of planar cell polarity, growth and the Hippo pathway: some known unknowns. Dev. Biol. *377*, 1–8.

Lee, T., and Luo, L. (1999). Mosaic analysis with a repressible cell marker for studies of gene function in neuronal morphogenesis. Neuron *22*, 451–61.

Leevers, S.J., Weinkove, D., MacDougall, L.K., Hafen, E., and Waterfield, M.D. (1996). The Drosophila phosphoinositide 3-kinase Dp110 promotes cell growth. EMBO J. *15*, 6584–6594.

Lin, T.H., Yeh, T.H., Wang, T.W., and Yu, J.Y. (2014). The hippo pathway controls border cell migration through distinct mechanisms in outer border cells and polar cells of the drosophila ovary. Genetics *198*, 1087–1099.

Lucas, E.P., Khanal, I., Gaspar, P., Fletcher, G.C., Polesello, C., Tapon, N., and Thompson, B.J. (2013). The Hippo pathway polarizes the actin cytoskeleton during collective migration of Drosophila border cells. J. Cell Biol. *201*, 875–85.

Ma, D., Yang, C., McNeill, H., Simon, M.A., and Axelrod, J.D. (2003). Fidelity in planar cell polarity signalling. Nature *421*, 543–547.

Mao, Y., Rauskolb, C., Cho, E., Hu, W.-L., Hayter, H., Minihan, G., Katz, F.N., and Irvine,

K.D. (2006). Dachs: an unconventional myosin that functions downstream of Fat to regulate growth, affinity and gene expression in Drosophila. Development *133*, 2539–2551.

Madhavan, M.M., and Madhavan, K. (1980). Morphogenesis of the epidermis of adult abdomen of Drosophila. J. Embryol. Exp. Morphol. *60*, 1–31.

Mani, M., Goyal, S., Irvine, K.D., and Shraiman, B.I. (2013). Collective polarization model for gradient sensing via Dachsous-Fat intercellular signaling. Proc. Natl. Acad. Sci. U. S. A. *110*, 20420–5.

Mao, Y., Kuta, A., Crespo-Enriquez, I., Whiting, D., Martin, T., Mulvaney, J., Irvine, K.D., and Francis-West, P. (2016). Dchs1–Fat4 regulation of polarized cell behaviours during skeletal morphogenesis. Nat. Commun. *7*, 11469.

Mao, Y., Mulvaney, J., Zakaria, S., Yu, T., Morgan, K.M., Allen, S., Basson, M.A., Francis-West, P., and Irvine, K.D. (2011). Characterization of a Dchs1 mutant mouse reveals requirements for Dchs1-Fat4 signaling during mammalian development. Development *138*, 947–57.

Matakatsu, H., and Blair, S.S. (2006). Separating the adhesive and signaling functions of the Fat and Dachsous protocadherins. Development *133*, 2315 –2324.

Matakatsu, H., and Blair, S.S. (2004). Interactions between Fat and Dachsous and the regulation of planar cell polarity in the Drosophila wing. Development *131*, 3785–3794.

Matis, M., and Axelrod, J.D. (2013). Regulation of PCP by the Fat signaling pathway. Genes Dev. *27*, 2207–20.

Mayor, R., and Etienne-Manneville, S. (2016). The front and rear of collective cell migration. Nat. Rev. Mol. Cell Biol *17*, 97-109.

Meijering, E., Dzyubachyk, O., and Smal, I. (2012). Methods for cell and particle tracking. Methods Enzymol. *504*, 183–200.

Merkel, M., Sagner, A., Gruber, F.S., Etournay, R., Blasse, C., Myers, E., Eaton, S., and Jülicher, F. (2014). The Balance of Prickle/Spiny-Legs Isoforms Controls the Amount of Coupling between Core and Fat PCP Systems. Curr. Biol. *24*, 2111–23.

Nagarkar-Jaiswal, S., Deluca, S.Z., Lee, P.T., Lin, W.W., Pan, H., Zuo, Z., Lv, J., Spradling, A.C., and Bellen, H.J. (2015). A genetic toolkit for tagging intronic MiMIC containing genes. eLife *4*, 2–9.

Ninov, N., Menezes-cabral, S., Weiss, A., Prat-rojo, C., Manjo, C., Pyrowolakis, G., and Affolter, M. (2010). Dpp Signaling Directs Cell Motility and Invasiveness during Epithelial Morphogenesis. Curr. Biol. *20*, 513–520.

Oh, H., and Irvine, K.D. (2009). In vivo analysis of Yorkie phosphorylation sites. Oncogene *28*, 1916–1927.

Olofsson, J., Sharp, K. a, Matis, M., Cho, B., and Axelrod, J.D., (2014). Prickle/spiny-legs isoforms control the polarity of the apical microtubule network in planar cell polarity. Development *141*, 2866–74.

Paré, A.C., Vichas, A., Fincher, C.T., Mirman, Z., Farrell, D.L., Mainieri, A., and Zallen, J.A. (2014). A positional Toll receptor code directs convergent extension in Drosophila. Nature *515*, 523–527.

Patel, N.H., Martin-Blanco, E., Coleman, K.G., Poole, S.J., Ellis, M.C., Kornberg, T.B., and Goodman, C.S. (1989). Expression of engrailed proteins in arthropods, annelids, and chordates. Cell *58*, 955–68.

Petitjean, L., Reffay, M., Grasland-Mongrain, E., Poujade, M., Ladoux, B., Buguin, A., and Silberzan, P. (2010). Velocity fields in a collectively migrating epithelium. Biophys. J. *98*, 1790–1800.

Pickering, K., Alves-Silva, J., Goberdhan, D., and Millard, T.H. (2013). Par3/Bazooka and phosphoinositides regulate actin protrusion formation during Drosophila dorsal closure and wound healing. Development *140*, 800–9.

Pocha, S.M., and Montell, D.J. (2014). Cellular and Molecular Mechanisms of Single and Collective Cell Migrations in Drosophila: Themes and Variations. Annu. Rev. Genet. *48*, 295–318.

Reffay, M., Parrini, M.C., Cochet-Escartin, O., Ladoux, B., Buguin, A., Coscoy, S., Amblard, F., Camonis, J., and Silberzan, P. (2014). Interplay of RhoA and mechanical forces in collective cell migration driven by leader cells. Nat. Cell Biol. *16*, 217–23.

Repiso, A., Saavedra, P., Casal, J., and Lawrence, P.A. (2010). Planar cell polarity: the orientation of larval denticles in Drosophila appears to depend on gradients of Dachsous and Fat. Development *137*, 3411–3415.

Riedl, J., Crevenna, A.H., Kessenbrock, K., Yu, J.H., Neukirchen, D., Bista, M., Bradke, F., Jenne, D., Holak, T.A., Werb, Z., Sixt, M., and Wedlich-Soldner, R. (2008). Lifeact: a versatile marker to visualize F-actin. Nat. Methods *5*, 605–7.

Rock, R., Schrauth, S., and Gessler, M. (2005). Expression of mouse dchs1, fjx1, and fat-j suggests conservation of the planar cell polarity pathway identified in Drosophila. Dev. Dyn. *234*, 747–55.

Rogulja, D., Rauskolb, C., and Irvine, K.D. (2008). Morphogen Control of Wing Growth through the Fat Signaling Pathway. Dev. Cell *15*, 309–321.

Rørth, P. (2012). Fellow travellers: emergent properties of collective cell migration. EMBO Rep. *13*, 984–991.

Rovira, M., Saavedra, P., Casal, J., and Lawrence, P.A. (2015). Regions within a single epidermal cell of Drosophila can be planar polarised independently. eLife *4*, e06303.

Sarov, M., Barz, C., Jambor, H., Hein, M.Y., Schmied, C., Suchold, D., Stender, B., Janosch, S., Kj, V.V., Krishnan, R.T., Krishnamoorthy, A., Ferreira, I.R.S., Plewka, N., Vinis, E., Schloissnig, S., Knust, E., (2016). A genome-wide resource for the analysis of protein localisation in Drosophila. eLife *5*, e12068.

Sharma, P., McNeill, H., (2013). Regulation of long-range planar cell polarity by Fat-Dachsous signaling. Development *140*, 3869–81.

Shi, D., Komatsu, K., Hirao, M., Toyooka, Y., Koyama, H., Tissir, F., Goffinet, A.M., Uemura, T., and Fujimori, T. (2014). Celsr1 is required for the generation of polarity at multiple levels of the mouse oviduct. Development *141*, 4558–68.

Shi, D., Arata, M., Usui, T., Fujimori, T., and Uemura, T. (2016). Seven-pass transmembrane cadherin CELSRs, and Fat4 and Dchs1 cadherins: from planar cell polarity to three-dimensional organ architecture. In The Cadherin Superfamily, S. Suzuki and S. Hirano eds. (Springer Publishing Company), pp. 251-276.

Shimono, K., Fujimoto, A., Tsuyama, T., Yamamoto-Kochi, M., Sato, M., Hattori, Y., Sugimura, K., Usui, T., Kimura, K., Uemura, T., 2009. Multidendritic sensory neurons in the adult Drosophila abdomen: origins, dendritic morphology, and segment- and age-dependent programmed cell death. Neural Dev. *4*, 37.

Silva, E., Tsatskis, Y., Gardano, L., Tapon, N., and McNeill, H. (2006). The Tumor-Suppressor Gene fat Controls Tissue Growth Upstream of Expanded in the Hippo Signaling Pathway. Curr. Biol. *16*, 2081–2089.

Simon, M. a., Xu, A., Ishikawa, H.O., and Irvine, K.D. (2010). Modulation of Fat:Dachsous Binding by the Cadherin Domain Kinase Four-Jointed. Curr. Biol. *20*, 811–817.

Sopko, R., Silva, E., Clayton, L., Gardano, L., Barrios-Rodiles, M., Wrana, J., Varelas, X., Arbouzova, N.I., Shaw, S., Saburi, S., et al. (2009). Phosphorylation of the Tumor Suppressor Fat Is Regulated by Its Ligand Dachsous and the Kinase Discs Overgrown. Curr. Biol. *19*, 1112–1117.

Spradling, A.C., Stern, D., Beaton, A., Rhem, E.J., Laverty, T., Mozden, N., Misra, S., and Rubin, G.M. (1999). The Berkeley Drosophila Genome Project gene disruption project: Single P-element insertions mutating 25% of vital Drosophila genes. Genetics *153*, 135–177.

Strutt, H., and Strutt, D. (2002). Nonautonomous planar polarity patterning in Drosophila: Dishevelled-independent functions in frizzled. Dev. Cell *3*, 851–863.

Tang, C.-Y., and Sun, Y.H. (2002). Use of mini-white as a reporter gene to screen for GAL4 insertions with spatially restricted expression pattern in the developing eye in drosophila. Genesis *34*, 39–45.

Terada, S.-I., Matsubara, D., Onodera, K., Matsuzaki, M., Uemura, T., and Usui, T. (2016). Neuronal processing of noxious thermal stimuli mediated by dendritic Ca $^{2+}$ influx in *Drosophila* somatosensory neurons. eLife *5*, 1–26.

Theveneau, E., Steventon, B., Scarpa, E., Garcia, S., Trepat, X., Streit, A., and Mayor, R. (2013). Chase-and-run between adjacent cell populations promotes directional collective migration. Nat. Cell Biol. *15*, 763–772.

Thomas, C., and Strutt, D. (2012). The roles of the cadherins Fat and Dachsous in planar polarity specification in Drosophila. Dev. Dyn. *241*, 27–39.

Toba, G., Ohsako, T., Miyata, N., Ohtsuka, T., Seong, K.H., and Aigaki, T. (1999). The gene search system. A method for efficient detection and rapid molecular identification of genes in Drosophila melanogaster. Genetics *151*, 725–37.

Tsukasaki, Y., Miyazaki, N., Matsumoto, A., Nagae, S., Yonemura, S., Tanoue, T., Iwasaki, K., and Takeichi, M. (2014). Giant cadherins Fat and Dachsous self-bend to organize properly spaced intercellular junctions. Proc. Natl. Acad. Sci. *111*, 16011–16016.

Usui, T., Shima, Y., Shimada, Y., Hirano, S., Burgess, R.W., Schwarz, T.L., Takeichi, M., and Uemura, T. (1999). Flamingo, a seven-pass transmembrane cadherin, regulates planar cell polarity under the control of Frizzled. Cell *98*, 585–595.

Villano, J., and Katz, F. (1995). four-jointed is required for intermediate growth in the proximal-distal axis in Drosophila. Development *121*, 2767–2777.

Vincent, J.P., and O'Farrell, P.H. (1992). The state of engrailed expression is not clonally transmitted during early Drosophila development. Cell *68*, 923–931.

Vladar, E.K., Antic, D., and Axelrod, J.D. (2009). Planar cell polarity signaling: the developing cell's compass. Cold Spring Harb. Perspect. Biol. *1*, a002964.

Wallingford, J.B. (2012). Planar cell polarity and the developmental control of cell behavior in vertebrate embryos. Annu. Rev. Cell Dev. Biol. *28*, 627–53.

Wang, W., and Yoder, J.H. (2011). Drosophila Pupal Abdomen Immunohistochemistry. J. Vis. Exp. e3139.

Willecke, M., Hamaratoglu, F., Sansores-Garcia, L., Tao, C., and Halder, G. (2008). Boundaries of Dachsous Cadherin activity modulate the Hippo signaling pathway to induce cell proliferation. Proc. Natl. Acad. Sci. U. S. A. *105*, 14897–14902.

Xu, T., and Rubin, G.M. (1993). Analysis of genetic mosaics in developing and adult Drosophila tissues. Development *117*, 1223–1237.

Yang, C.H., Axelrod, J.D., and Simon, M.A. (2002). Regulation of Frizzled by Fat-like cadherins during planar polarity signaling in the Drosophila compound eye. Cell *108*, 675–688.

Zakaria, S., Mao, Y., Kuta, A., Ferreira De Sousa, C., Gaufo, G.O., McNeill, H., Hindges,

R., Guthrie, S., Irvine, K.D., and Francis-West, P.H. (2014). Regulation of neuronal migration by Dchs1-Fat4 planar cell polarity. Curr. Biol. *24*, 1620–1627.

Zeidler, M.P., Perrimon, N., and Strutt, D.I. (2000). Multiple roles for four-jointed in planar polarity and limb patterning. Dev. Biol. *228*, 181–96.

Zhang, L., Ren, F., Zhang, Q., Chen, Y., Wang, B., and Jiang, J. (2008). The TEAD/TEF family of transcription factor Scalloped mediates Hippo signaling in organ size control. Dev. Cell *14*, 377–387.

Figure 1
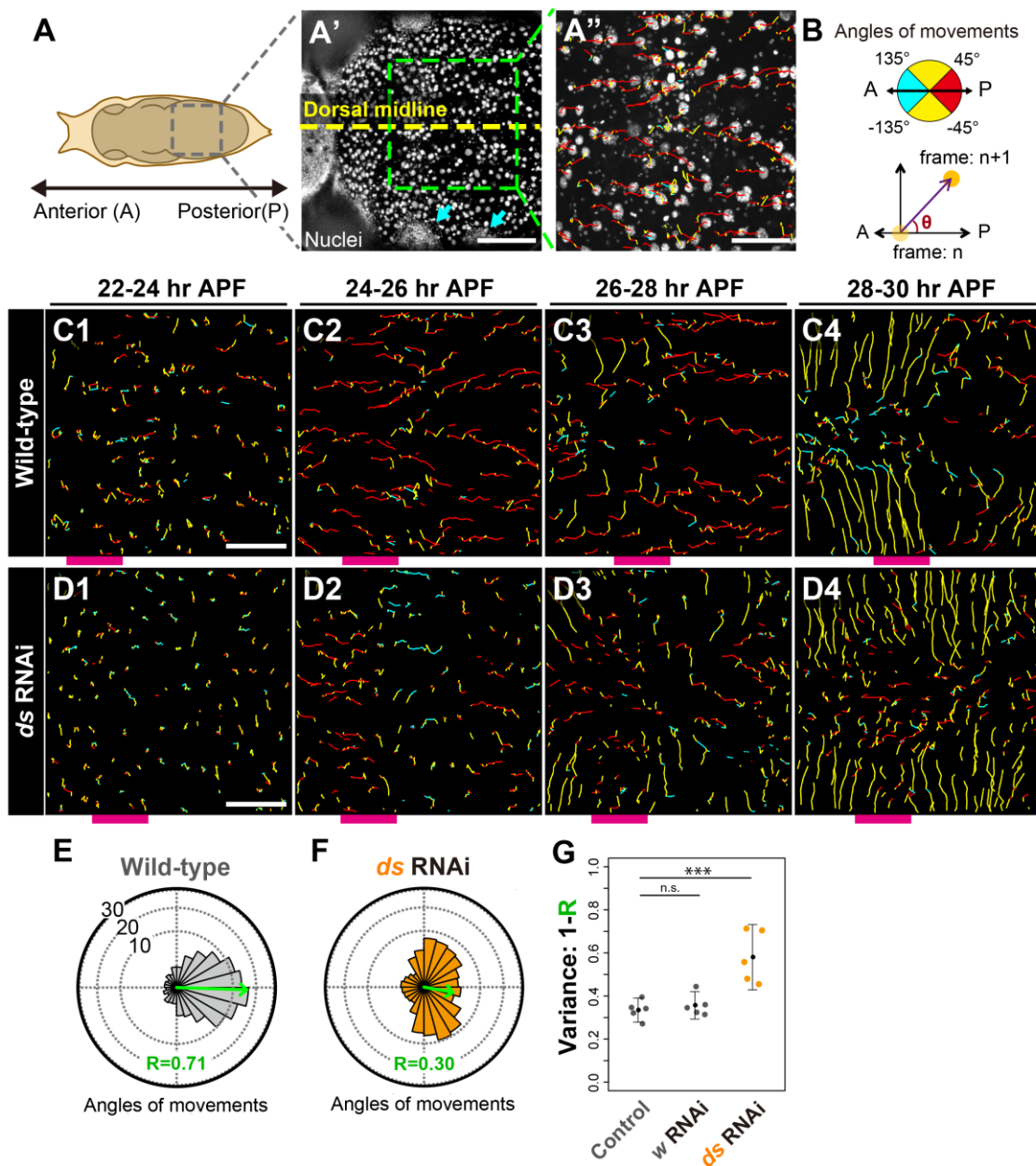
Figure 1. Imaging and quantitative analysis of Ds-dependent posterior migration of LECs

(**A-B**) A diagram of a dorsal front view of a Drosophila pupa (**A**). Anterior is to the left, posterior is to the right and all photos are dorsal front views hereafter, unless described otherwise. A region of the pupal case was peeled off to image an abdominal subregion (the gray boxed area is shown in **A'**). (**A'-B**) Images of His2Av:GFP^{S65T} at 22 hr APF (**A'**) and 26 hr APF (**A''**). (**A'**) A yellow dotted line indicates the dorsal midline, and cyan arrows mark histoblast nests. (**A''**) A high-power image of the green boxed area (**A'**)

spanning abdominal segments A2 and A3, where trajectories of individual LEC nuclei during 24-26 hr APF are indicated by colored lines. (**B**) Red, cyan, and yellow represent posterior, anterior, and dorso-ventral movements, respectively.

(**C-D**) Trajectories of wild-type LECs (**C1-C4**) and those of *ds*-depleted LECs (**D1-D4**) during indicated 2 hr intervals. Magenta bars: estimated positions of the posterior compartment (see Figure S1**D1-D3** and its legend).

(**E-G**) Angles of the movements of LEC nuclei between consecutive frames of each movie were calculated relative to the A-P axis of the body. The data of representative wild-type (**C1-C4**) and *ds*-depleted (**D1-D4**) pupae during the two-hour window, which scored the minimum circular variance, are plotted on rose diagrams (**E** and **F**, respectively). Posterior movements are to the right side of each diagram. The mean angles are represented by arrows and the arrow length "R" indicates one minus circular variance. The rose diagram consists of 24 bins of 15° each and dotted concentric circles are drawn in 10% increments. Ages of "E" and "F" are 24:40-26:40 and 29:30-31:30 hr APF, respectively. Circular variance is defined as the value that gives the best coordination during the recording (see details in STAR methods), which is seen at 29:30-31:30 hr APF in the *ds* knockdown pupa (**D1-D4**). The coordination at 24-26 hr (**D2**) was even worse because Ds-dependent LECs moved in the opposite anterior direction (cyan tracks in **D2**). (**G**) A plot of circular variances of the control, *white*-depleted (*w*; another control), and *ds*-depleted pupae. The data sets are identical to those in Figure S1**C**. See STAR methods for details including how we defined representative values of circular variances of individual pupae. The variance was significantly increased by *ds* depletion (Dunnett's test; ***: $p < 0.001$, n.s.: not significant). Data are shown as a dot plot with the mean (black dot) $\pm$ 95% confidence interval (CI). Scale bar: 200 μm (**A'**) and 100 μm (**A", C1** and **D1**). See also Movie **S1**.
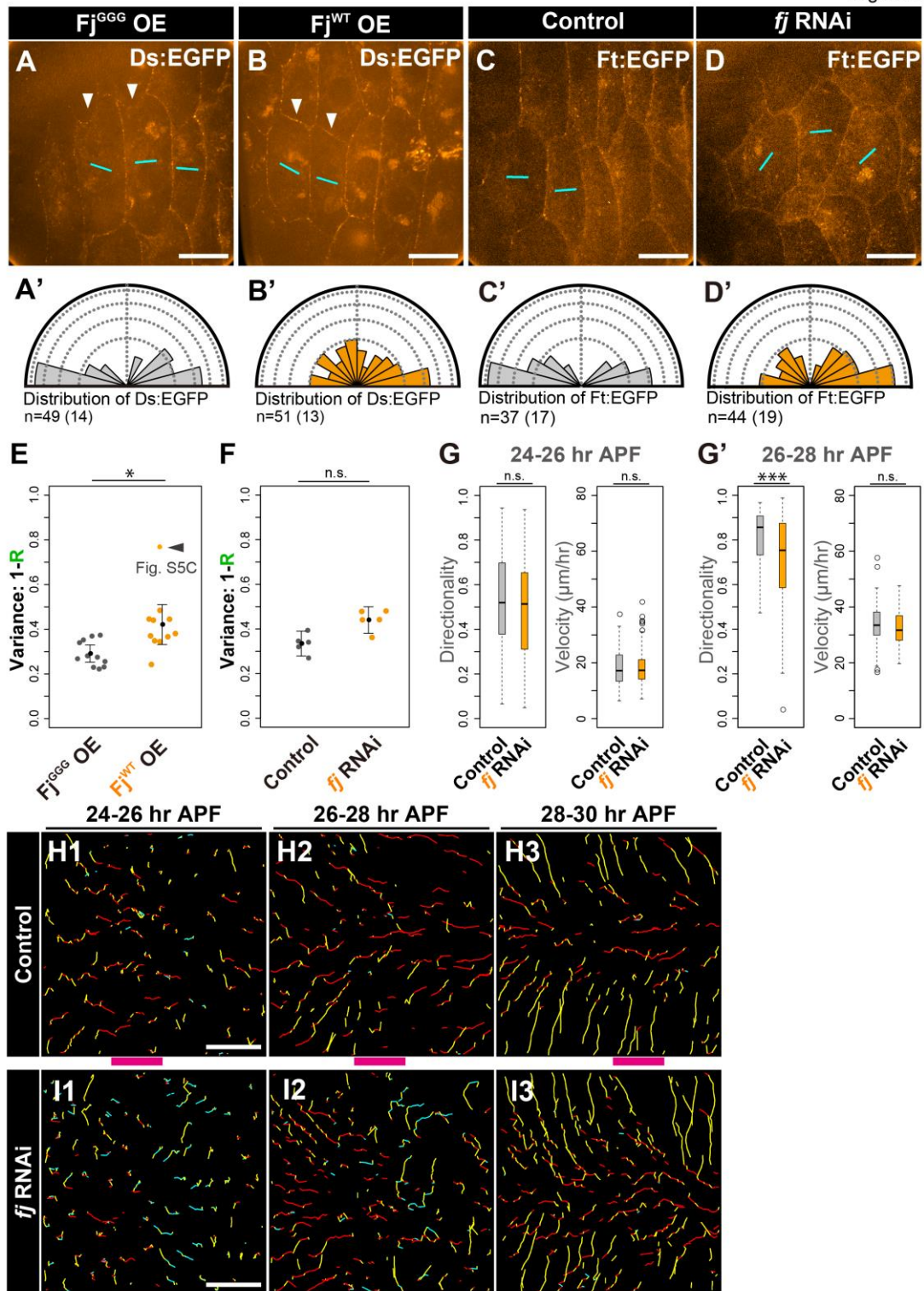
Figure 2
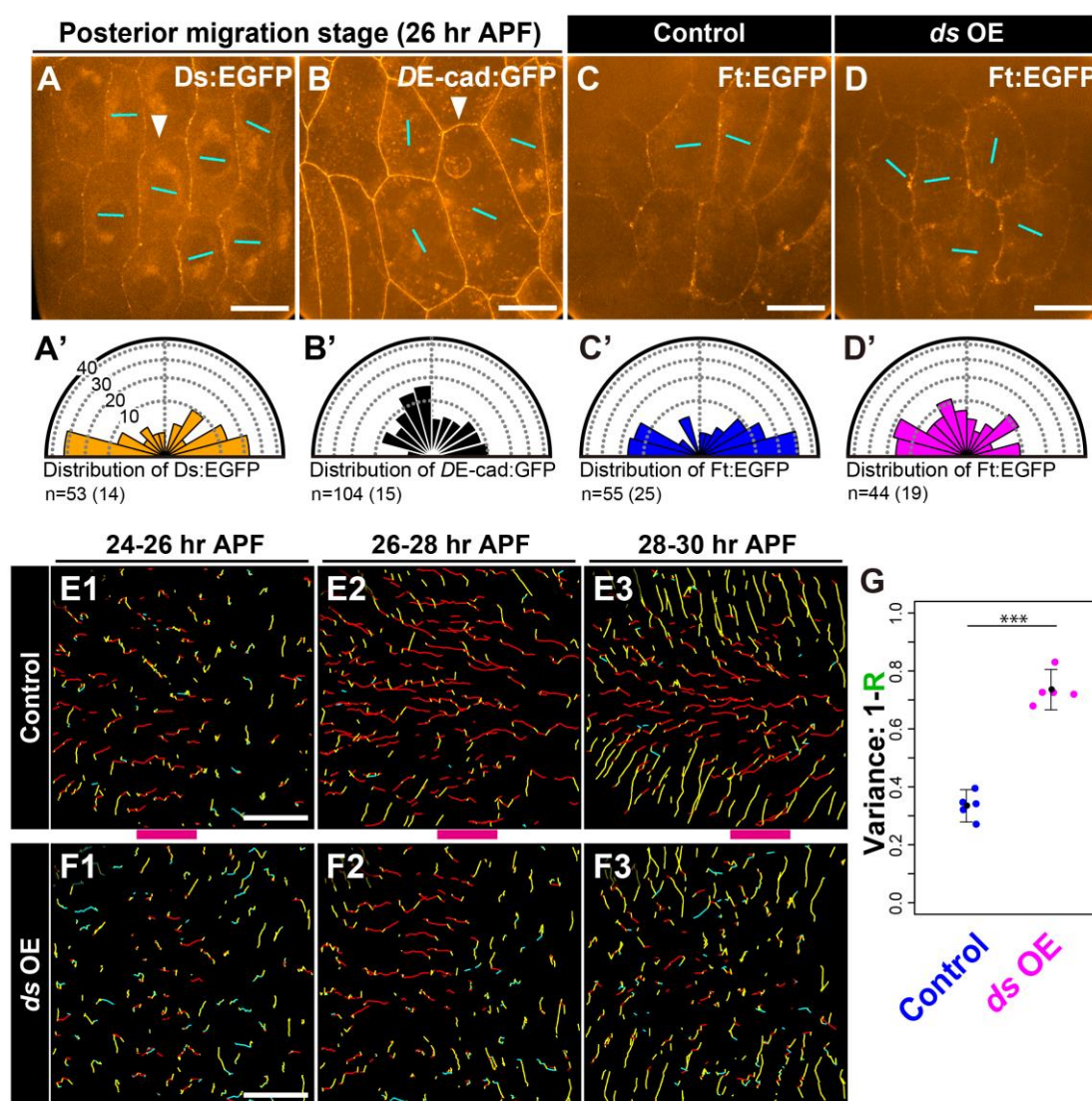
Figure 2. Polarized localization of Ds and Ft, and effects of *ds* overexpression on Ft localization and posterior migration of LECs

(**A-B'**) Subcellular localizations of Ds:EGFP and *D*E-cadherin:GFP (*D*E-cad:GFP) in LECs at 26hr APF (**A** and **B**, respectively). Ds:EGFP was enriched at A-P cell boundaries in contrast to relatively uniform *D*E-cad:GFP. Arrowheads point to D-V boundaries where *D*E-cad:GFP is present (**B**) but Ds:EGFP appears to be missing (**A**). Angles of cyan bars represent axes of the polarity of protein localization in individual cells and the directional distributions of bar angles are plotted on rose diagrams (**A'** and **B'**; Aigouy et al., 2010). Indicated at the lower left-hand corner of each diagram are the number of cells analyzed and that of pupae from which the data were collected (in parentheses). Dotted concentric circles are drawn in 10% increments in rose diagrams.

(**C-G**) *ds* overexpression (OE) abrogated A-P polarized localization of Ft:EGFP (**C-D'**, 26hr APF) and the posterior movement of LECs (**E-G**). See detailed explanations of markings and the rose diagrams (**C-D'**) in the legend above, and those of the trajectories and the plot (**E-G**) in the Figure 1 legend. In **G**, The data sets are identical to those in Figure S1**C**. ***: Dunnett's test, p< 0.001. Data are shown as a dot plot with the mean (black dot) $\pm$ 95% CI. Magenta bars: estimated positions of the posterior compartment. Scale bars: 30 µm (**A-D**) and 100 µm (**E1** and **F1**). See also Figure S1.

Figure 3. Effect of *fj* overexpression or knockdown on Ds or Ft localization and posterior migration of LECs

(**A-B'**) Effect of Fj overexpression on Ds localization at 26hr APF. (**A** and **A'**).

Overexpression of the kinase-dead Fj^{GGG}:mCherry (a fusion of the kinase-dead form of Fj with mCherry) did not affect the polarized localization of Ds (compare with Figure 2**A** and 2**A'**). (**B** and **B'**) In contrast, overexpression of Fj^{WT}:mCherry (a fusion of the wild-type form of Fj with mCherry) abrogated A-P enriched Ds localization. Also see explanations in the legend of Figure 2**A**-2**B'**.

(**C-D'**) Polarized localization of Ft:EGFP (**C** and **C'**) was abrogated when *fj* was knocked down (**D** and **D'**).

(**E**) The overexpression of Fj^{GGG}:mCherry hardly affected posterior movements of LECs (Fj^{GGG} OE in **E**). In contrast, that of Fj^{WT}:mCherry made the movement less biased (Fj^{WT} OE in **E**). * in **E**: Welch's t-test, p < 0.05. Data are shown as a dot plot with the mean (black dot) $\pm$ 95% CI. The arrowhead marks the pupa that gave the largest value of variance and trajectories of its LECs are shown in Figure S5C. Without this pupa, the difference from Fj^{GGG} OE is still significant (p < 0.01).

(**F-I3**) Effects of *fj* knockdown on LEC migration are analyzed in terms of the circular variance (**F**), and the directionality and the velocity (**G** and **G'**). (**G** and **G'**) Directionalities and mean velocities of LEC movements during 24-26 (**G**) or 26-28 hr APF (**G'**). Data of the indicated genotypes are shown as box-and-whisker plots. Details of directionality and the velocity are in Figure S2. *fj* knockdown affected the directionality, but not the velocity of LEC movements or the circular variances (n.s. in **F**: Dunnett's test). n = 214 and 124 cells (5 pupae) for control (**G** and **G'**, respectively), and 191 and 111 cells (5 pupae) for *fj* RNAi. *** in **G'**: Dunnett's test, p < 0.001. The data sets in **F**, **G** and **G'** are identical to those in Figure S1**C**, S2**E1-E2** and S2**E3-E4**, respectively, and detailed explanations are as in the legend of Figure 1**G** or S2**E1-E4**. (**H1-I3**) Trajectories of representative control LECs (**H1-H3**) and those of *fj*-depleted LECs (**I1-I3**). See detailed explanations of trajectories in the legend of Figure 1**B**-1**D4**.

Scale bars: 30 µm (**A-D**) and 100 µm (**H** and **I**). See also Figure **S5** (**A1-C2**).

Figure 4
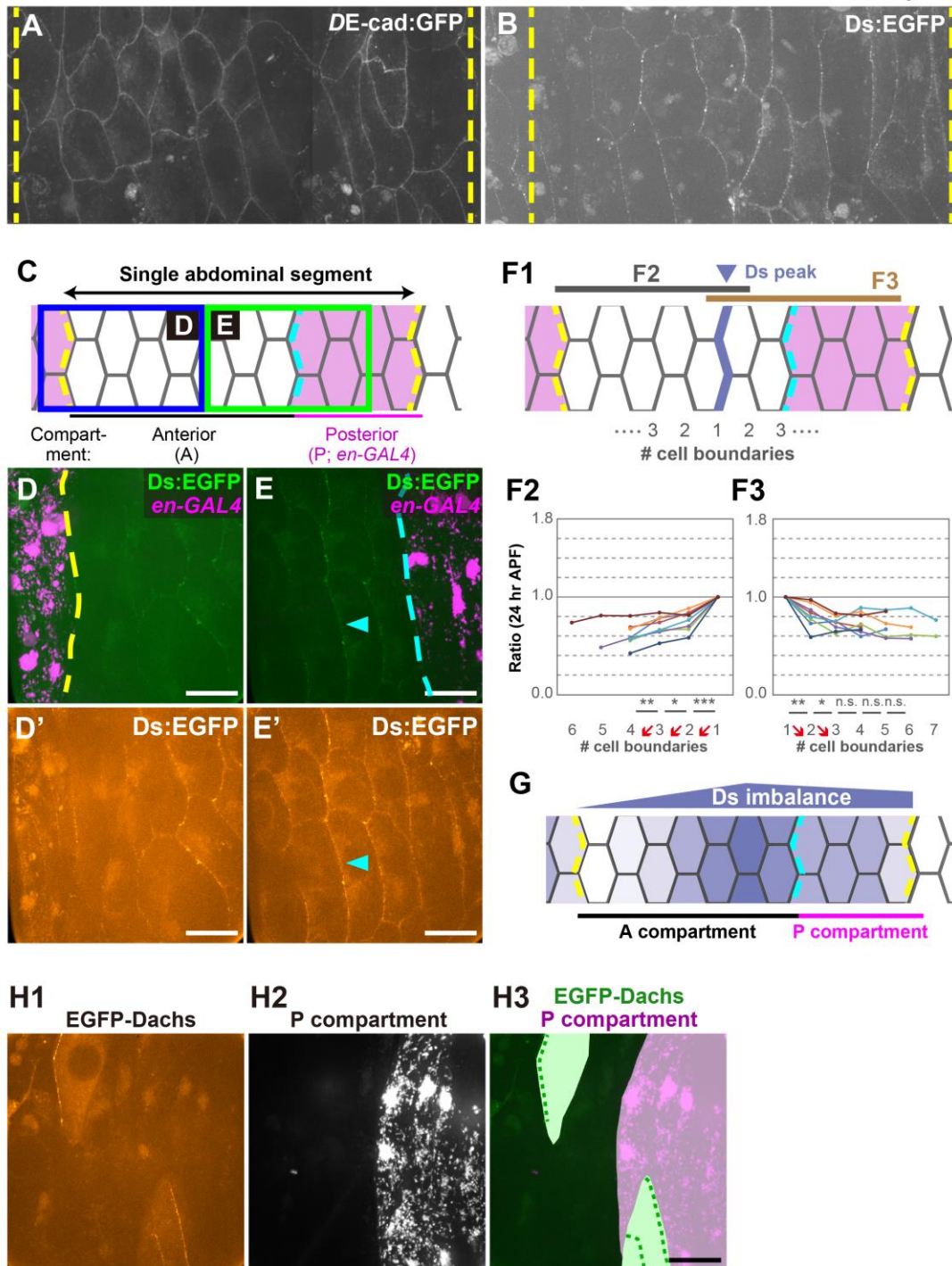
Figure 4. Imbalance of Ds amounts between LECs along the A-P axis within each abdominal segment

(**A** and **B**) An image of an abdominal segment of the *DE-cad:GFP* (**A**) or *ds:EGFP* (**B**) knock-in strain at 26 hr APF, which was made by connecting four images along the A-P axis. Yellow lines represent segment borders in this and subsequent Figures.

(**C**) A diagram of an abdominal segment, where the posterior compartment (*en-Gal4* positive cells) is highlighted by magenta. Images corresponding to the blue and green boxed regions are shown in **D-D'**, and in **E-E'**, respectively. Cyan broken lines represent A/P compartment borders in this and subsequent Figures
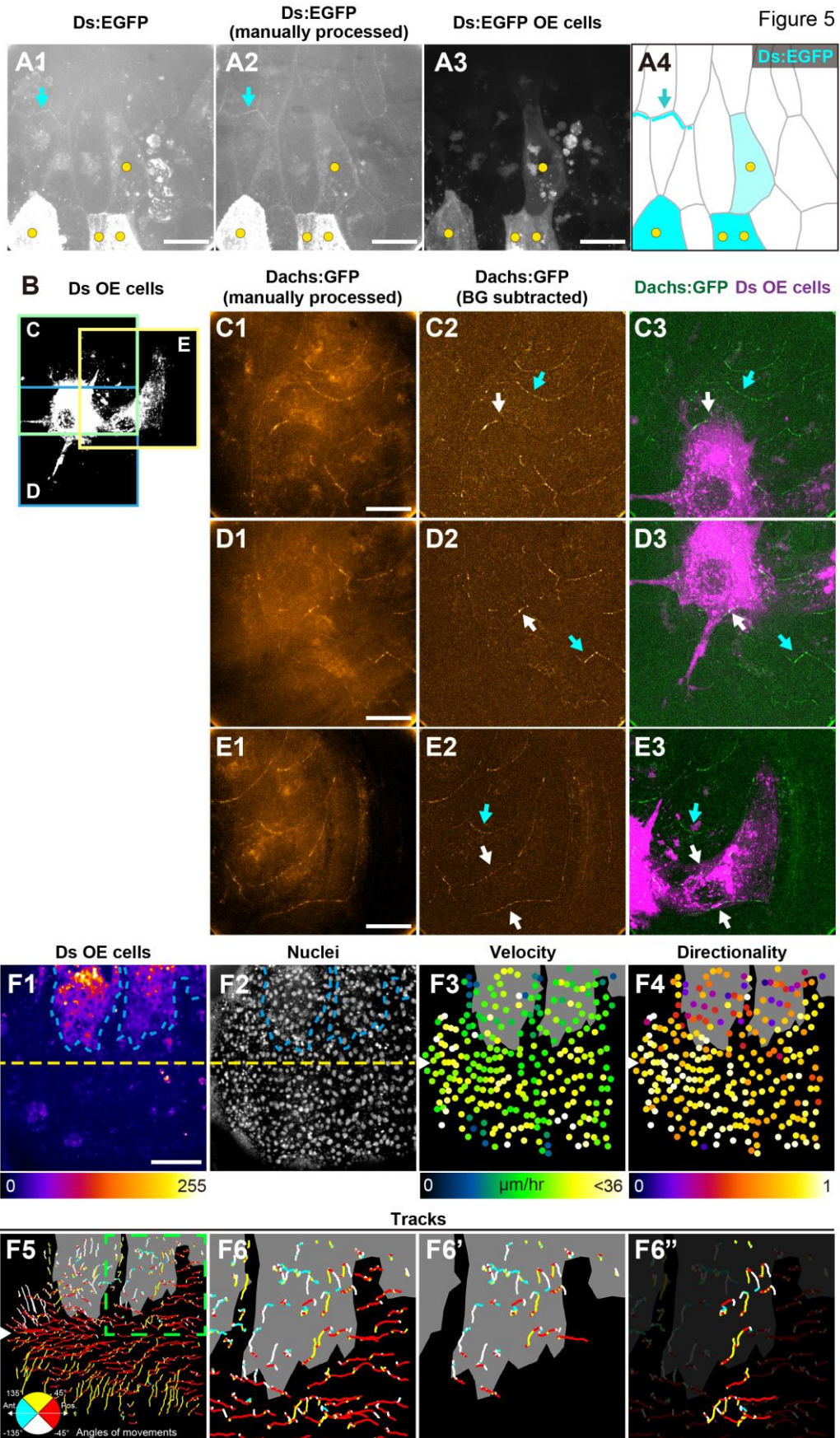
(**D-E'**) LECs of distinct regions marked in **C** at 26 hr APF. Signals of Ds:EGFP (green in **D** and **E**; **D'** and **E'**) which were merged with those of posterior compartments (magenta in **D** and **E**; *en-GAL4*).

(**F1-F3**) Quantification of the amount of Ds at cell boundaries along the A-P axis. The average intensity of signals of Ds:EGFP on each cell boundary along the D-V axis (labeled with # cell boundaries in **F1**) was calculated, those values were normalized against those on the Ds-peak boundaries (pointed with blue arrowheads; cell boundaries #1 in **F1-F3**), and normalized values in underlined regions in **F1** were plotted on line graphs (**F2** and **F3**; see details in Figure **S6** and STAR methods). (**F2-F3**) Imbalance was statistically tested between indicated adjacent cell boundaries (paired t-test; ***: p<0.001, **: p<0.01, *: p<0.05, n.s.: not significant). Red down arrows illustrate the statistically significant imbalance of Ds:EGFP. Note that the intensity of Ds becomes weaker towards the segment borders at least in the region anterior to the Ds peak (**F2**).

(**G**) The imbalance of the Ds amounts along the A-P axis in the segment is illustrated on top of the diagram of an abdominal segment. Note that the peak lies two cells anterior to the A/P compartment border.

(**H**) EGFP:Dachs (**H1**; light green in **H3**) was clonally expressed in LECs, imaged at 24 hr APF, and merged with those of posterior compartments (*en-GAL4, UAS-mmRFP*; **H2** and magenta in **H3**). Note that EGFP:Dachs was polarized at opposite cell edges in the anterior and posterior compartments. Another example of the clone is shown in Figure S7**H**.

Scale bars: 30 µm. See also Figure **S6**.

Figure 5

Ds:EGFP   Ds:EGFP (manually processed)   Ds:EGFP OE cells

A1   A2   A3   A4   Ds:EGFP

B Ds OE cells

Dachs:GFP (manually processed)   Dachs:GFP (BG subtracted)   Dachs:GFP   Ds OE cells

Ds OE cells   Nuclei   Velocity   Directionality

0   255   0   μm/hr   <36   0   1

Tracks

135° Ant.   45° Pos.
-135°   -45°   Angles of movements

38

Figure 5. Effects of artificial Ds imbalance on Ds or Dachs localization and LEC movements

(**A1-A4**) The effect on localization of Ds:EGFP. (**A1**) A maximum intensity projection of the original images of Ds:EGFP signals. (**A2**) Signals derived from more basal planes were manually subtracted before projection. (**A3**) An image of a marker for Ds:EGFP-overexpressing (OE) cells. (**A4**) An illustration of the Ds:EGFP OE cells (colored in cyan and marked with yellow dots here and in **A1**-**A3**), cell boundaries (gray lines), and Ds:EGFP ectopically enriched at D-V cell boundaries (cyan lines here and cyan arrows in **A1**, **A2**, and **A4**) that are located one-cell apart from a Ds:EGFP OE cell. The manual processing highlights the ectopic localization of Ds:EGFP (cyan arrows in **A1** and **A2**).

(**B-E3**) The effect on localization of Dachs:GFP. (**B**) Ds OE cells were labeled with a clone marker, mCherry:CAAX. Boxed regions **C**, **D**, and **E** were imaged and shown in **C1-C3**, **D1-D3**, and **E1**-**E3**, respectively. (**C1**, **D1**, and **E1**) Signals of autofluorescence and Dachs:GFP from more basal planes were manually subtracted from maximum intensity projections. (**C2**, **D2**, and **E2**) From images of **C1**, **D1**, and **E1**, backgrounds were subtracted by applying "Subtract Background" in ImageJ to 16 bit images (Rolling Ball Radius: 50 pixels). (**C3**, **D3**, and **E3**) Dachs:GFP signals of **C2**, **D2**, and **E2** are colored in green; and the clone marker, in magenta. White arrows mark Dachs:GFP at the outermost boundaries of the *ds* OE clones, whereas cyan arrows those at boundaries that were one-cell apart from the clones.

(**F1-F6"**) The effect on LEC migration. A dorsal view of a pupa at 25 hr APF. Clones of Ds:EGFP OE LECs were labeled with mCherry:CAAX (**F1**), while nuclei of all LECs were with His2Av:GFP (**F2**). Clones in the right hemisegment are outlined with blue broken lines (**F1** and **F2**) or filled with gray color (**F3-F6"**). Yellow dotted lines (**F1** and **F2**) or white triangles (**F3-F5**) indicate the positions of the dorsal midlines. Intensities of the clone marker reflect the *ds* expression level, and they are color-coded in **F1**. Note that Ds:EGFP overexpression level was higher in the more ventrally positioned OE cells. Mean velocity (**F3**) or directionality (**F4**) of LEC movements during 25-28 hr APF, which were calculated based on manual tracking data (**F5-F6"**; see also Figure S2**C** and **C'**). Color dots in **F3** and **F4** mark the positions of nuclei at 25 hr APF and their colors indicate the values of the velocity or the directionality as shown at the bottom of the panels. In **F5-F6"**, trajectories of LECs during 25-28 hr APF are shown by lines, and their colors indicate angles of the movements as in the inset of **F5**. The boxed region in **F5** is enlarged in **F6-F6"**. Trajectories of Ds OE cells are highlighted in **F6'**. Yellow trajectories in **F6** (highlighted in **F6"**) indicate that those LECs migrated up on the ectopic hill of overexpressed Ds, away from the midline, which is the reverse orientation of the control

cells.

Scale bars: 30 µm in **A1-E3**; 200 µm in **F1**.
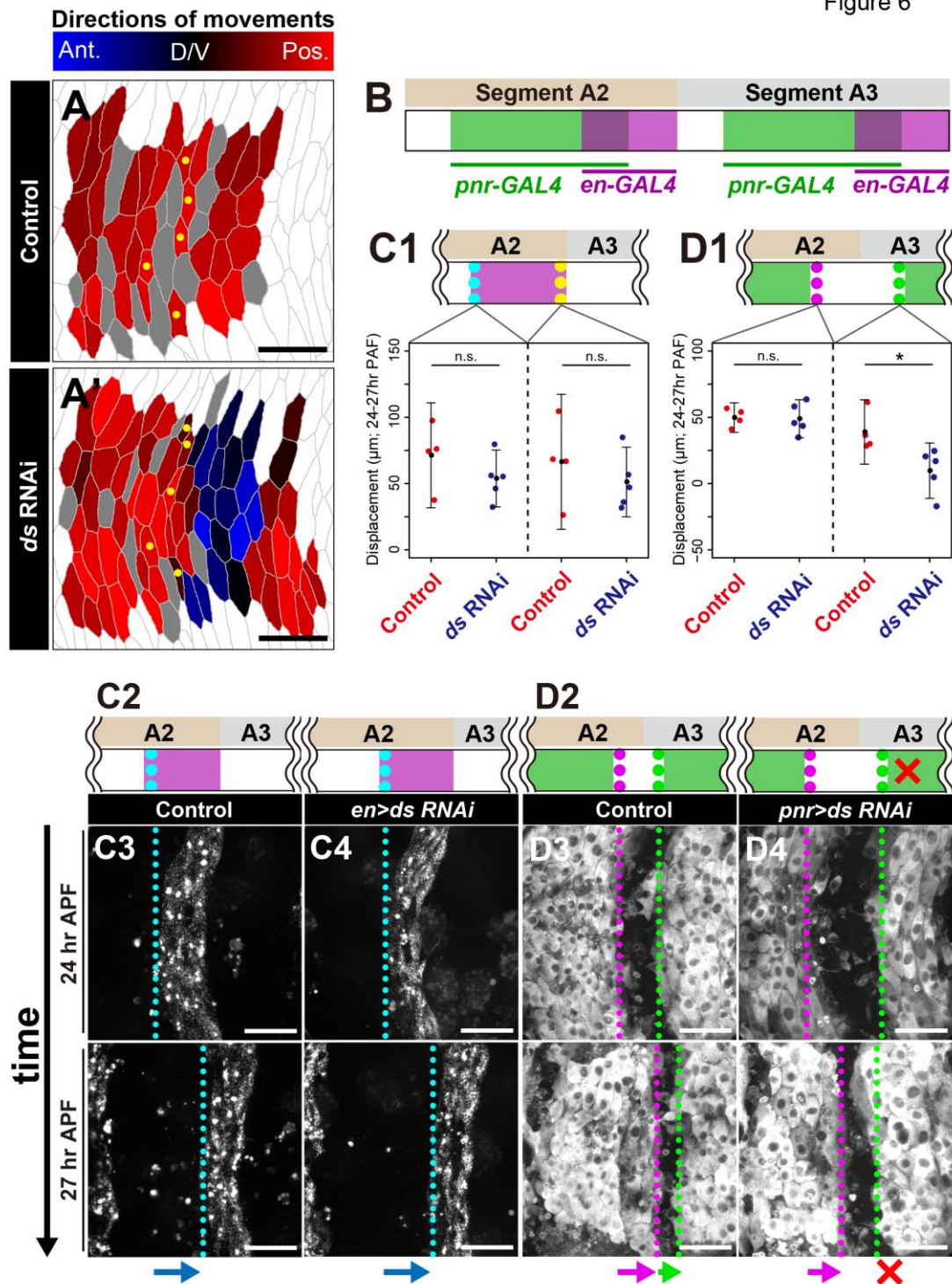
Figure 6

Figure 6. LECs that migrated in a Ds-dependent manner were located in the anterior compartment

(**A** and **A'**) Directions of LEC movements during 23-27 hr APF are color coded as indicated by the scale on top of the panels. Images are cell-boundary tracings of LECs at

23 hr APF for which the results of the data analysis are merged. Yellow dots mark LECs along the segment boundary (See STAR methods and Figure S1D1-D3 for details of how we mapped LECs along the segment boundary). *ds* knockdown caused abnormal migration of LECs most likely only in a subset of the anterior compartment of the segment (blue cells in **A'**), while all of control LECs migrated posteriorly (**A**). Gray cells underwent apoptosis during the recording.

(**B**) Diagram illustrating the spatial relationship of the *pnr* domain (green; *pnr-GAL4*) to the *en* domain (magenta; *en-GAL4*) in segment A2 and A3.

(**C1** and **D1**) Diagrams of regional knockdown of *ds* in the *en* domain (**C1**) or in the *pnr* domain (**D1**), and their effects on LEC migration. We manually traced the anterior and posterior borders of *en* (**C1**) or *pnr* (**D1**) domains and calculated the displacement of the averaged coordinate of each border along the A-P axis between 24 and 27 hr APF. Note that only the displacement of the anterior edge of the *pnr* domain was affected by *ds* knockdown (green broken line in **D1**; *****: Welch's t-test, $p < 0.05$). Data are shown as a dot plot with the mean (black dot) $\pm$ 95% confidence interval (CI).

(**C2-D4**) Snapshots taken at 24 hr APF (top) and at 27 hr APF (bottom). (**C2-C4**) *ds* knockdown in the *en* domain did not abrogate posterior migration of the domain (aqua broken lines and blue arrows). (**D2-D4**) In contrast, *ds* knockdown in the *pnr* domain arrested the migration of its anterior border (green broken lines and red cross), but not the posterior border (magenta broken lines and magenta arrows).

Scale bars: 100 µm. See also Movie **S5** and **S6**.

Figure 7
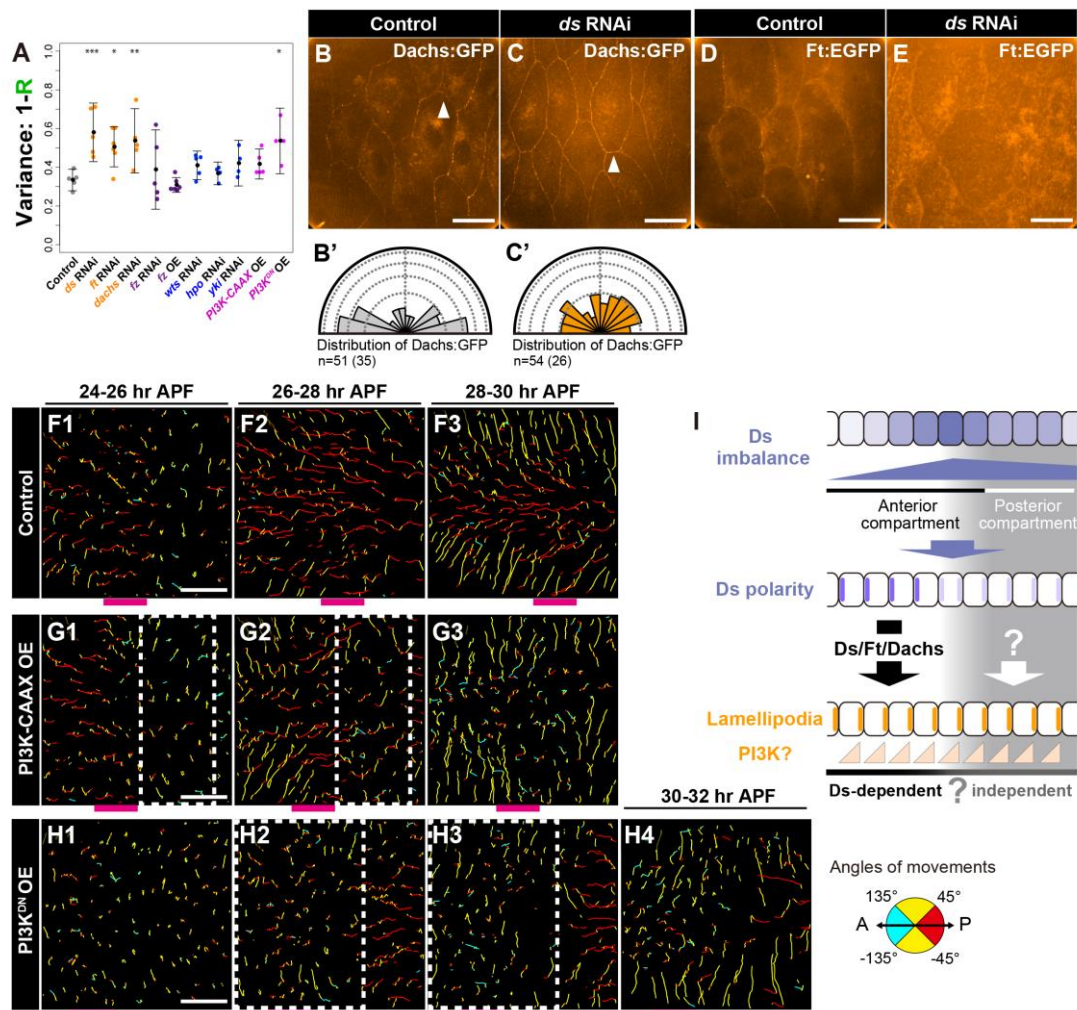
Figure 7. Deciphering the molecular mechanism of Ds-dependent migration

(**A**) A plot of circular variances of LEC movements in pupae of the control and with the indicated genetic conditions. The representative two-hour time window was selected for each pupa. Data are shown as a dot plot with the mean (black dot) $\pm$ the 95% CI. The data sets are identical to those in Figure S1**C**. Dunnett's test; ***: p<0.001, **: p<0.01, *: p<0.05.

(**B-E**) Polarized localizations of Dachs:GFP and Ft:GFP depend on Ds. Images of Dachs:GFP-expressing LECs (**B** and **C**) and Ft:EGFP-expressing LECs (**D** and **E**) at 26hr APF. Arrowheads point at D-V cell boundaries. Directional distributions of polarity axes of the protein localizations are plotted on rose diagrams (**B'** and **C'**). Polarized localization of Dachs:GFP (**B** and **B'**) was lost when *ds* was knocked down (**C** and **C'**). Tight localization of Ft:EGFP at the cell boundaries (**D**) was lost when *ds* was knocked down (**E**). See other explanations in the legend of Figure 2**A**-2**B'**.

43

(**F1**-**H4**) Trajectories of control LECs (**F1-F3**), and PI3K-CAAX or PI3K^{DN} misexpressed LECs (**G1-G3** or **H1-H4**) during indicated 2 hr intervals. The data sets of the control are identical to those in Figure **2E1-E3**. PI3K-CAAX or PI3K^{DN} misexpression abrogated the posterior migration of LECs irrespective of whether they locate in the anterior or the posterior compartment (indicated by white boxes in **G1-G2** or **H2**-**H3**). Magenta bars: estimated positions of the posterior compartment. Scale bar: 30µm in **B-E** and 100 µm in **F1-H4**.

(**I**) Model for the mechanism by which Ds drives posterior migration of LECs. (Top) Cross-sectional diagram of LECs that are aligned along the A-P axis in each abdominal segment. They express Ds differentially (Ds imbalance). (Middle) This Ds imbalance polarizes Ds localization in each LEC (Ds polarity), and Ds-enriched cell boundaries are indicated with thick bars (shaded in Ds-independent LECs). (Bottom) This Ds polarity, together with Ft and Dachs, direct lamellipodia formation at posterior cell boundaries, which requires PI3K (its hypothetical subcellular localization/activity is indicated with orange triangles); and this mechanism works in a subset of LECs in the anterior compartment of each segment (thick black arrow). Exact borders of Ds-dependent LECs are not precisely defined (gray question mark at the bottom; details are described in the text related to Figure 6). Migration of LECs in the posterior compartment does not depend on Ds, and its driving mechanism is unknown (shaded).

See also Movie **S7**.

STAR Methods

EXPERIMENTAL MODEL AND SUBJECT DETAILS

Drosophila strains

Pupae were kept at 25°C and imaged at stages indicated in the Result section of the main text, Figures and legends of Figures. *UAS-fj:mCherry*, *UAS-fj^{GGG}:mCherry*, *UAS-ds:EGFP,* and *UAS-ft:EGFP* were generated in this study. All the stocks are listed in Key Resources Table. Exact genotypes of individual animals used in Figures are described below:

Figure 1

(A', A'', C1-C4, and E) *His2Av:GFP^{S65T}*

(D1-D4, F, and *ds* RNAi in G) *hs-flp22/X; Ay-GAL4, UAS-mCherry:CAAX/+; UAS-ds RNAi/His2Av:GFP^{S65T}*

(Control in G) *hs-flp22/X; Ay-GAL4, UAS-mCherry:CAAX/+; His2Av:GFP^{S65T}/+*

(*w* RNAi in G) *hs-flp22/X; Ay-GAL4, UAS-mCherry:CAAX/+; UAS-w RNAi/His2Av:GFP^{S65T}*

Figure 2

(A and A') *ds:EGFP, FRT-40A/DE-cadherin:mTomato*

(B and B') *DE-cadherin:GFP/DE-cadherin:mTomato*

(C and C') *hs-flp22/X; Ay-GAL4, UAS-mCherry:CAAX/+; fat:EGFP, FRT82B/+*

(D and D') *hs-flp22/X; Ay-GAL4, UAS-mCherry:CAAX/GS-ds; fat:EGFP, FRT82B/+*

(E1-3 and Control in G) *hs-flp22/X; Ay-GAL4, UAS-mCherry:CAAX/+; His2Av:GFP^{S65T}/+*

(F1-3 and *ds* OE in G) *hs-flp22/X; Ay-GAL4, UAS-mCherry:CAAX/GS-ds; His2Av:GFP^{S65T}/+*

Figure 3

(A and A') *UAS-fj^{GGG}:mCherry/ds:EGFP, FRT-40A*; *tubulin-GAL4/+*

(B and B') *UAS-fj:mCherry/ds:EGFP, FRT-40A; tubulin-GAL4/+*

(C and C') *hs-flp22/X; Ay-GAL4, UAS-mCherry:CAAX/+; fat:EGFP, FRT82B/UAS-w-RNAi*

(D and D') *hs-flp22/X; Ay-GAL4, UAS-mCherry:CAAX/+; fat:EGFP, FRT82B/UAS-fj-RNAi*

(Fj^{GGG} OE in E) *UAS-fj^{GGG}:mCherry/+; tubulin-GAL4/His2Av:GFP^{S65T}*

(Fj^{WT} OE in E) *UAS-fj:mCherry/+; tubulin-GAL4/His2Av:GFP^{S65T}*

(Control in F-G' and H1-H3) *hs-flp22/X; Ay-GAL4, UAS-mCherry:CAAX/+; His2Av:GFP^{S65T}/+*

(*fj* RNAi in F-G' and I1-I3) *hs-flp22/X; Ay-GAL4, UAS-mCherry:CAAX/+; His2Av:GFP^{S65T}/UAS-fj-RNAi*

Figure 4

(A) *DE-cadherin:GFP/engrailed-Gal4, UAS-myr-mRFP*

(B, F2 and F3) *ds:EGFP, FRT-40A*

(D-E') *ds:EGFP, FRT-40A/engrailed-Gal4, UAS-myr-mRFP*

(H1-H3) *hs-flp22/X; engrailed-Gal4, UAS-myr-mRFP/Act>stop>EGFP-dachs*

Figure 5

(A1-A4) *hs-flp22/X; Ay-GAL4, UAS-mCherry:CAAX/ ds:EGFP, FRT-40A; UAS-ds:EGFP/+*

(B-E3) *hs-flp22/X; Ay-GAL4, UAS-mCherry:CAAX/GS-ds; dachs:GFP/+*

(F1-6") *hs-flp22/X; Ay-GAL4, UAS-mCherry:CAAX/His2Av:EGFP ;UAS-ds:EGFP/+*

Figure 6

(A) *hs-flp22/X; Ay-GAL4, UAS-mCherry:CAAX/+; scribble:GFP/+*

(A') *hs-flp22/X; Ay-GAL4, UAS-mCherry:CAAX/+; scribble:GFP /UAS-ds-RNAi*

(Control in C1 and C3) *engrailed-GAL4, UAS-myr-mRFP/+; His2Av:GFP^{S65T}/+*

(*ds* RNAi in C1 and C4) *engrailed-GAL4, UAS-myr-mRFP/+; His2Av:GFP^{S65T}/UAS-ds RNAi*

(Control in D1 and D3) *UAS-mCD8:3xEGFP/+; pannier-GAL4/+*

(*ds* RNAi in D1 and D4) *UAS-mCD8:3xEGFP/+; pannier-GAL4/UAS-ds-RNAi*

Figure 7

(A) Control: *hs-flp22/X; Ay-GAL4, UAS-mCherry:CAAX/+; His2Av:GFP^{S65T}/+*

RNAi or OE: *hs-flp22; Ay-GAL4, UAS-mCherry:CAAX; His2Av:GFP^{S65T}/UAS-RNAi or OE on X, 2nd or 3rd* (see Key Resources Table)

(B and B') *hs-flp22/X; Ay-GAL4, UAS-mCherry:CAAX/+; dachs:GFP/+*

(C and C') *hs-flp22/X; Ay-GAL4, UAS-mCherry:CAAX/+; dachs:GFP/UAS-ds-RNAi*

(D) *hs-flp22/X; Ay-GAL4, UAS-mCherry:CAAX/+; fat:EGFP, FRT82B/+*

(E) *hs-flp22/X; Ay-GAL4, UAS-mCherry:CAAX/+; fat:EGFP, FRT82B/UAS-ds-RNAi*

(F1-F3) *hs-flp22/X; Ay-GAL4, UAS-mCherry:CAAX/+; His2Av:GFP^{S65T}/+*

(G1-G3) *hs-flp22/UAS-PI3K-CAAX; Ay-GAL4, UAS-mCherry:CAAX/+; His2Av:GFP^{S65T}/+*

(H1-H4) *hs-flp22/X; Ay-GAL4, UAS-mCherry:CAAX/UAS-PI3K^{DN}; His2Av:GFP^{S65T}/+*

Figure S1

(C) Control: *hs-flp22/X; Ay-GAL4, UAS-mCherry:CAAX/+; His2Av:GFP^{S65T}/+*

RNAi or OE: *hs-flp22; Ay-GAL4, UAS-mCherry:CAAX; His2Av:GFP^{S65T}/UAS-RNAi or OE* on X, 2nd or 3rd (see Key Resources Table)

(D1-D3) *engrailed-Gal4, UAS-myr-mRFP/+; His2Av:GFP^{S65T}/+*

(E1-E4) *ds:EGFP, FRT-40A*

(F1-F3) *pnr-GAL4, UAS-mCherry:CAAX/UAS-w-RNAi*

Figure S2

(A-B', *ds* RNAi in D1-D3, and D4) *hs-flp22/X; Ay-GAL4, UAS-mCherry:CAAX/+; UAS-ds RNAi/His2Av:GFP^{S65T}*

(Control in D1) *hs-flp22/X; Ay-GAL4, UAS-mCherry:CAAX/+; His2Av:GFP^{S65T}/+*

(Left panels in E1-E4)

Control: *hs-flp22/X; Ay-GAL4, UAS-mCherry:CAAX/+; His2Av:GFP^{S65T}/+*

RNAi or OE: *hs-flp22; Ay-GAL4, UAS-mCherry:CAAX; His2Av:GFP^{S65T}/UAS-RNAi or OE* on X, 2nd or 3rd (see Key Resources Table)

(Right panels in E1-E4)

Fj^{GGG} OE: *UAS-fj^{GGG}:mCherry/ds:EGFP, FRT-40A; tubulin-GAL4/+*

Fj^{WT} OE: *UAS-fj:mCherry/ds:EGFP, FRT-40A; tubulin-GAL4/+*

Figure S3

(A and A') *hs-flp22/X; Ay-GAL4, UAS-mCherry:CAAX/+; UAS-GPH/+*

(B1-E) *DE-cadherin:mTomato/+; Kst^{GFSTF}/+*

(F1-F4) *hs-flp22/X; Ay-GAL4, UAS-mCherry:CAAX/+; Kst^{GFSTF}/UAS-w-RNAi*

(G1-H') *hs-flp22/X; Ay-GAL4, UAS-mCherry:CAAX/+; Kst^{GFSTF}/UAS-ds-RNAi*

Figure S4

(Control in A-D) *hs-flp22/X; Ay-GAL4, UAS-mCherry:CAAX/+; scribble:GFP/+*

(*ds* RNAi in A-D) *hs-flp22/X; Ay-GAL4, UAS-mCherry:CAAX/+; scribble:GFP/UAS-ds-RNAi*

(Control in E') *UAS-mCD8:3xEGFP/+; pannier-GAL4/+*

(*ds* RNAi in E')*UAS-mCD8:3xEGFP/+; pannier-GAL4/UAS-ds-RNAi*

Figure S5

(A1 and A2) *UAS-fj^{GGG}:mCherry/+; tubulin-GAL4/His2Av:GFP^{S65T}*

(B1-C2) *UAS-fj:mCherry/+; tubulin-GAL4/His2Av:GFP^{S65T}*

(D1-E4) *fj^{VG1}/UAS-EGFP*

(F-H) *fj^{VG1}/ds:EGFP, FRT-40A; UAS-mCherry:CAAX/+*

Figure S6

(A, C1-C5, and D1-D5) *DE-cadherin:GFP/engrailed-Gal4, UAS-myr-mRFP*

(B, E1-E5 and F1-F5) *ds:EGFP, FRT-40A*

Figure S7

(A-G4) *hs-flp22/X; ubi-mRFP.nls, FRT-40A/ds:EGFP, FRT-40A*

(H1-H3) *hs-flp22/X; engrailed-Gal4, UAS-myr-mRFP/Act>stop>EGFP-dachs*

METHOD DETAILS

Molecular biology

Coding sequences of *fj* and *fj^{GGG}* were cloned from pUASTattB-fj:V5 and pUASTattB-fj^{GGG}:V5 (Ishikawa et al. 2008), respectively, to construct pUASTattB-fj:mCherry and pUASTattB-fj^{GGG}:mCherry. Transgenic stocks were generated by using attP landing site at 22A or 86Fa. Consistent with the previous study (Ishikawa et al. 2008), legs of adult flies were shortened by overexpression of Fj:mCherry under the control of *tubulin-GAL4*, indicating that Fj:mCherry is functional (data not shown). Coding sequences of *ds* and *ft* were cloned from pUAST-ds and pUAST-ft (Matakatsu and Blair 2004), respectively, to construct pUAST-ds:EGFP and pUAST-ft:EGFP. Their transgenic stocks were generated by standard methods. Uniform expression of Ds:EGFP rescued the PCP defect of *ds* mutant wings (*ds^{05142}/ds^{05142}; UAS-ds:EGFP/tubulin-GAL4*), confirming that Ds:EGFP is functional (data not shown).

Live imaging

Live imaging of pupae was performed basically as described in the previous study (Harumoto et al. 2010; Figure 1A). Pupal cases over abdominal segments A2-3 were peeled off and pupae were put on 35-mm glass-bottomed dishes (IWAKI) with the peeled sides down. Images or movies of LECs were acquired with an Olympus IX71 microscope equipped with a spinning-disk confocal scan head (CSU10; Yokogawa) and an EM-CCD camera (DU-888; Andor Technology). Fluorescent proteins were excited with 488 nm and 561 nm beams from diode-pumped solid-state lasers (Coherent Sapphire), and were detected with Semrock FF03 525/50 and Chroma HQ 610/60 band-pass filters, respectively. The following lenses (Olympus) were used: UPLSAPO60XS (60x silicon-oil immersion objective), UPlanFL N 20x/0.45, and UPlanFL N 10x/0.30. To track migrating LECs, time-lapse recordings were performed at 5 min intervals, and LECs of A2 and A3 were imaged as observed in Bischoff 2012 (for example, see Figure S1B and S1F1-F3, and the legends). The above imaging system was driven by MetaMorph software (Molecular Devices). After the live imaging, we confirmed that flies developed to at least the pharate adult. Intensities of signals were color-coded by applying the Lookup Table, "Orange Hot" (e.g., Figure 2A-D) or "Fire" (e.g., Figure 5F1) in ImageJ

to the data.

Preparation of samples of the Drosophila pupal notum for image collection was conducted as previously described (Koto et al. 2009; Classen et al. 2008). Pupae were washed in water and fixed on a glass slide with double-sided tape. Then, the pupal case over the entire notum was peeled off. A small drop of Immersol W 2010 (Zeiss) was put on the glass bottom dish, and the sample was placed in the dish with double-sided tape so that the notum faced the cover-slip. Wet Kimwipe was placed in the dish to prevent drying. Nota of *DE-cadherin:GFP* (Huang et al. 2009) were imaged from 16 to 23 hr APF at 1 min interval with an inverted confocal spinning disk microscope (Olympus IX83 combined with Yokogawa CSU-W1) equipped with an iXon3 EMCCD camera (Andor), an Olympus 60X/NA1.2 SPlanApo water-immersion objective, and a temperature controlled chamber (TOKAI HIT), using IQ 2.9.1 (Andor) (Guirao et al. 2015).

Analysis of angles of LEC movements

To analyze movements of LECs, we tracked nuclei labeled with His2Av:GFP^{S65T}. Trajectories of nuclei could represent not only the movement of the cells *per se* but also that of nuclei within the cells, but it was reported that the latter is negligible (Bischoff 2012). We also manually tracked movements LECs, which were labeled with a cell boundary marker, Scribble:GFP (Buszczak et al. 2007), and confirmed that movements of nuclei represent those of the cells.

Nuclear signals in each frame of the time-lapse recordings were binarized, and particle signals that met the following conditions of size and velocity were tracked automatically by ImageJ plugin "Mtrack2": 128 µm^2～480 µm^2 and ＜12 µm/frame respectively. Angles of the movements of individual nuclei between two consecutive frames (10 min interval) were calculated respective to the A-P axis, summed within arbitrary two-hour time windows, and plotted on rose diagrams composed of 24 bins of 15° each, representing 360° around the starting point of each of the nuclei. The area of each bin represents the number of movements between consecutive frames in that bin as a percentage of the total population of the movements tracked, and concentric circles are drawn with 10% increments between them. The mean angle of the direction of movement is indicated by a green arrow on each rose diagram, and the arrow length "R" represents one minus the circular variance (Figure 1E and 1F). Please note that an angle of the movement can be calculated by using one time frame (n) and the next one (n+1) as far as the same nuclei was tracked between the two frames (Figure S2C). Reliability of our quantification was validated as described in the legend of Figure S2D1-D4. Throughout this study, we used ImageJ for generating movies or images of tracks of LEC nuclei,

calculating angles of movements and intensities, and other image processing; and R for drawing rose diagrams, and calculating circular variances and mean angles of movements.

To quantify how strongly the posterior movement of LECs was aligned in each pupa and to compare those values between different genotypes, the representative values of circular variance of movement angles for each animal were determined as follows: we imaged movements of LECs during at least 24-28 hr APF, calculated circular variances for every possible two-hour window within individual recordings, and determined the time window that scored the smallest circular variance (the longest arrow "R") in each movie. Those circular variances were compared between different genotypes by Dunnett's test (Figure 1G, 2G, 3F, 7A and S1C) or Welch's t-test (Figure 3E). Because we imaged dorsal front views where LECs in the contralateral hemisegments move in opposite directions, the circular variance becomes large during the dorsal migration; therefore, we can specifically evaluate the coordination of posterior movements, not that of dorsal movements. It should be also noted that the exact hr APF of the posterior migration phase is not fixed in each genotype including the wild type, because all pupae do not synchronize the onset of the posterior migration and the timing of the dorsal turn. To more precisely describe the spatio-temporal pattern of LEC movements in different genotypes, the "temporal registration" (Bosveld et al. 2012) of each recording is essential. We have also calculated the evolution of velocities in time to identify the time point of the onset of the migration in each recording. However, it was difficult to specify such a time point, because all LECs did not start the migration simultaneously. More specifically, not only *ds*-depleted but also control LECs (e.g. Figure 2E1) in the more posterior segment tended to initiate the migration later. That is why we calculated the minimum circular variance as an alternative method, which does not rely on the timing of the onset of the migration. *ds* knockdown seemed to reduce the velocity of LECs in the right half of Fig. 1D2. In contrast, velocity of control LECs in the right half of Fig 1C2 and those in the left half seemed comparable. We speculate that this difference between Figure 1D2 and 1C2 is not based on the difference in the genotypes, but on the difficulty in the temporal registration. In other words, all of LECs in the Figure 1C2 and LECs in the left half of Figure 1D2 already started the migration; in contrast, *ds*-depleted LECs in the right half of Fig. 1D2 did not. Please also note Figure 2E1 where control LECs in the right half of image showed slower movements than those in the left half. Although the resolution is limited, we analyzed the spatial characteristics of LEC movement by plotting the relationship between the angle of movements and velocity and also the relationship between the angle of movements and directionality (data not shown). Our data clearly showed that there was no difference in the values of velocity between *ds*-depleted LECs

which moved in the anterior direction and those in the posterior direction during 24-26 hr APF.

Quantification of velocity and directionality of LEC movements (Figure 3G-3G' and S2)

To quantify mean velocity and directionality of LEC movements, it was required to use tracks of individual LECs that were identified consecutively throughout the time window. However, the consecutive tracking was technically challenging in our collective cell migration, because LECs often came in close contact with non-LEC signals or with other LECs, where our auto tracking did not necessarily distinguish individual cells (Figure S2B) and only manual tracking managed to do (Figure S2A). In addition, some LECs underwent apoptosis or moved out of the recording field, which forced tracking terminated. As a consequence, tracks of LECs that were identified consecutively for two hours (2 hr consecutive tracks) by auto tracking (Figure S2B') comprised one-third to one-half of those made by the manual tracking (Figure S2A'). Only those 2 hr consecutive tracks (10 min interval) were used for calculating the directionality and the velocity of LEC movements. Reliability of our quantification was validated as described in the legend of Figure S2D1-D4.

Quantification of the bias in the subcellular distribution of β-heavy Spectrin (β$_H$-Spec)/Karst (Kst) body (Figure S3)

We evaluated the bias in the subcellular distribution of the β$_H$-Spec body (masses of β$_H$-Spec signals in LECs) as follows: First, we outlined the β$_H$-Spec body and the whole cell, and calculated the positions of their centers of mass. Second, a vector from the center of mass of the whole cell to that of the β$_H$-Spec body was drawn and its angle relative to the A-P axis was calculated (ImageJ). Finally the angle distribution was shown by using the rose diagram. The area of each bin represents the number of cells in that bin as a percentage of the total population of the cells examined, and concentric circles are drawn with 10% increments between them. The mean angle of the subcellular distribution of the β$_H$-Spec body is indicated by a green arrow on each rose diagram, and the arrow length "R" represents one minus the circular variance (Figure S3C4, D4, F4 and G4).

Analysis of polarized localization of proteins at cell boundaries

The original quantification method (nematic order; Aigouy et al. 2010) was modified as described (Shi et al. 2014) to determine the axis of nematic order for a single cell (cyan bars in Figure 2A-2D, 3A-3D). Cell boundaries of LECs were traced manually (by using

the line tool in ImageJ; line width: 5 pixels), and x, y coordinates and intensity of each pixel which comprise the cell boundaries were acquired. Intensities of the signals were collected as *I(x, y)*. Then, *I(x, y)* was converted into a polar coordinate form, *I(r, θ); r* indicates the distance between the pixel and the center of the cell, and θ is the angular coordinate of the position of the pixel, where 0° is the posterior direction. The average value of *I(r, θ)* for each bin of 5° (e.g. 2.5°-7.5°, 7.5°-12.5°, etc.) was calculated and was set to $S(\theta_m)$, where θ_m is the center θ value of the bin (e.g. $\theta_m=5°$, 10°, etc.). The polarity of the signals at cell boundaries ϕ ($0° \leq \phi < 180°$) was determined for each cell to fit:

$$\cos 2\phi = Q_1 / \sqrt{Q_1^2 + Q_2^2} \quad , \quad \sin 2\phi = Q_2 / \sqrt{Q_1^2 + Q_2^2} \quad , \quad \text{where} \quad Q_1 = \sum S(\theta_m) \cos 2\theta_m \quad ,$$

$Q_2 = \sum S(\theta_m) \sin 2\theta_m$. Distributions of their angles relative to the A-P axis ($0° \leq \theta \leq 180°$) are drawn in rose diagrams (Figure 2A'-2D', 3A'-3D' and 7B'-7C'). The area of each bin represents the number of cells in that bin as a percentage of the total population of the cells examined, and concentric circles are drawn with 10% increments between them.

Analysis of the difference of Ds:EGFP and *D*E-cad:GFP amounts at cell boundaries along the A-P axis within each abdominal segment (Figure 4F2, 4F3, and S6)

To quantify signals of Ds:EGFP and *D*E-cad:GFP at cell boundaries, images were pre-processed as follows: signals derived from more basal planes were manually cleared before the maximum intensity projection, and background signals were subtracted by applying "Subtract Background" in ImageJ to 16 bit images after projection (Rolling Ball Radius: 5 pixels). Cell boundaries of Ds:EGFP-expressing pupae were traced manually by masking the boundaries with 5 pixel-wide lines, as shown in Figure S6C3, D3, E3, and F3, and intensities of pixels were acquired. In Figure 4F2-F3 and S6C4-F5, the signal intensity of Ds:EGFP or *D*E-cad:GFP on each line was averaged per pixel and its ratio to the averaged intensity on the *ds* peak boundaries (marked with gray arrowheads in Figure S6) was calculated and plotted. In Figure S6A, C1-C5, and D1-D5, we estimated that the position of Ds peak boundaries locates at two cells anterior to the A/P compartment border.

Measurement of width of abdominal segments and the displacement of the *en* and *pnr* domains (Figure 6B-D4 and Figure S4E-E')

LECs of A2 and A3 segments of *UAS-mCD8:3xEGFP/+; pannier-GAL4/+* or *UAS-mCD8:3xEGFP/+; pannier-GAL4/UAS-ds-RNAi* were imaged with a window size of 819.2 x 819.2 µm. Posterior edges of *pnr-GAL4* positive domains (P-edges) were traced, and coordinates of pixels comprising edges were acquired. To evaluate segment width,

we set the ROI with a height of 320 µm around the dorsal midline and calculated the distance between averaged coordinates of P-edges of A2 and A3 within the ROI (Figure S4E). To evaluate the displacement of *en* or *pnr* domain (Figure 6C and 6D), each was labeled with mmRFP or mCD8:3xEGFP and imaged with a window size of 409.6 x 409.6 µm. The indicated edges in Figure 6C1 and D1 were manually traced, and the displacement of the averaged coordinate of each edge along the A-P axis between 24 and 27 hr APF was calculated.

Searching for candidates of Dachs binding-proteins that are required for the posterior migration of LECs

We narrowed down the list of candidate proteins that bind to Dachs myosin (Kwon et al., 2013) by selecting proteins that are implicated in controlling lamellipodia formation in other systems. We knocked down following 10 genes individually to search for those that are necessary for the directional migration of LECs: *zyxin*, *CG10933*, *tumbleweed*, *sticky*, *β-heavy Spectrin (βH-Spec)/Karst (Kst)*, *Swiprosin-1*, *Cortactin*, *α Spectrin*, *pod1* and *Calmodulin*.

Analysis of movement directions, apoptosis, cell rearrangements, cell area changes, and roundness changes of LECs (Figure 6A, A' and S4A-D)

We performed time lapse recordings of LECs that expressed a cell-boundary marker Scribble:GFP during 23-30 or 23-32 hr APF. GFP images were skeletonized to detect cell boundaries by using custom-made plug-ins and macros in ImageJ. From the skeletonized images, neighborship was defined (ImageJ macro), the size of each cell was measured, and roundness of each cell was estimated by fitting an ellipse and represented as the ratio of minor to major axes of the ellipse. LECs were tracked manually using ImageJ plugin "MTrackJ (Meijering et al. 2012)", and parameters (the position of the cell center, the size, the roundness, and the neighborship) were compared between 23 hr and 27 hr APF and denoted as follows:

Direction of movement (Figure 4A and A')

Angles of LEC movements calculated from the displacement of cell centers. LECs along the segment border at 23 hr APF were deduced by the position relative to histoblast nests at 32 hr APF in 23-32hr APF live imaging movies.

Cell size change (Figure S4A-A")

The ratio of area size of each LEC at 27 hr APF to that of the same cell at 23 hr APF.

Roundness change (Figure S4B-B")

The ratio of roundness of each LEC at 27 hr APF to that of the same cell at 23 hr APF.

Neighbors lost per cell (Figure S4C-C")

The ratio of the number of neighbor relations that were lost by cell rearrangements during 23-27 hr APF to the total number of cells at 23 hr APF.

Cell elimination rate (Figure S4D)

The ratio of the number of dead cells during 23-27 hr APF to the total number of cells at 23 hr APF.

Temporally and spatially restricted expression of transgenes in LECs

We used an *Ay-Gal4* stock (*hs-flp22; Ay-GAL4, UAS-mCherry:CAAX/CyO*; Ito et al. 1997) to express transgenes in temporally and spatially restricted manners in LECs. Heat-shock treatments of white pupae for 30 minutes at 37°C in a water bath resulted in expression of transgenes in most, if not all, LECs but rarely in histoblast nests (e.g. the expression of *mCherry:CAAX* in the genotype of Figure 1D1-D4; data not shown). This all-or-none pattern of expression is presumably because LECs are polyploid cells and have multiple copies of the genome; therefore, recombination occurs more frequently in LECs than in diploid histoblast cells (Bischoff 2012). When we made mosaic patches of LECs that expressed transgenes, white pupae were heat shocked for 10 minutes at 37°C in a water bath (Figure "*ds* RNAi" in movie S2 and S4) or larvae were heat shocked for 5 minutes at 37 °C in water bath (Figure 5B-E3, S3A-A' and "control" in movie S2) Alternatively, we used the IR-LEGO-200 system (Kamei et al. 2009) as described in a previous study (Terada et al. 2016; 20mW for 4sec x 2 times at the white pupa stage; "*ds* OE" in movie S4). To visualize lamellipodia and quantify its localization (Figure S3A-A'), it is required to generate ideally single, or a few at most, GPH-expressing LECs that are isolated from one another. Although we tested a number of different conditions for the heat-shock induction, we found it technically challenging to collect a large number of such GPH-expressing cells. Figure S3A-A' and Movie S2 show the best time-lapse recordings of the wild type and *ds*-depleted cells, respectively, in our experiments. To generate an ectopic imbalance of the Ds expression along the dorso-ventral axis, we heat shocked LECs locally by dropping hot paraffin (65°C) onto pupae at 5 hr APF and removing the drop after 10 seconds (Figure 5F1-F6') or by pressing a warm soldering iron (47°C) against white pupae for 5 seconds (Figure 5A1-A4). To clonally express EGFP-Dachs in LECs (Figure 4H1-H3 and S7H1-H3), we mated *hs-flp22/Y; en-GAL4, UAS-mmRFP/+* males with *Act>stop>EGFP-Dachs* (Brittle et al., 2012) females. White pupae were heat shocked for 5 minutes at 37°C in a water bath.

Immunohistochemistry

54

Immunohistochemistry was performed as described (Wang and Yoder 2011). Primary antibodies or other materials used in this study and dilutions were as follows: mouse anti-Engrailed monoclonal antibody (4D9, Patel et al. 1989, DSHB and a gift from C. Hama) at 1:10 dilution, rabbit anti-GFP polyclonal antibody (A6455, Life Technologies) at 1:300 dilution, phalloidin, Alexa Fluor 546 conjugate (Molecular Probes) at 1:200 dilution, and VECTASHIELD Mounting Medium with DAPI (Vector Laboratories). Images of DAPI were acquired with a Nikon C1 laser-scanning confocal microscope.

Mosaic analysis (Figure S7)

To juxtapose LECs expressing wild-type Ds and those expressing Ds:EGFP under the control of the endogenous *ds* promoter (Brittle et al. 2012), we mated *hs-flp22/Y; ubi-mRFP.nls, FRT40A/+* males with *ds:EGFP, FRT40A* females. Embryos were collected at 3.5-4 hr AEL (after egg laying), heat shocked for 45 min in a water bath at 37°C, rested for 30 min in an incubator at 25°C, and given another heat shock.

QUANTIFICATION AND STATISTICAL ANALYSIS

R was used for all of statistical analysis. Statistical significance was defined as $p < 0.05$. Statistical tests used, exact p-values, sample sizes, mean and 95% confidence intervals (CI) in figures are described below:

Figure 1

(G) The data sets are identical to those in Figure S1C. See the description of Figure S1C in this section.

Figure 2

(G) The data sets are identical to those in Figure S1C. See the description of Figure S1C in this section.

Figure 3

Values of circular variances of movement angles were compared between Fj^{GGG} OE and FJ^{WT} OE pupae.

(E) Welch's t-test; $p = 0.0104$; $n = 11$ (Fj^{GGG} OE) and 11 (Fj^{WT} OE) pupae; mean = 0.29 (Fj^{GGG} OE) and 0.42 (Fj^{WT} OE); 95% CI of the mean: ± 0.039 (Fj^{GGG} OE) and ± 0.089 (Fj^{WT} OE).

Without the datum of the Fj^{WT} OE pupa that gave the largest value of variance (marked with an arrowhead):

Welch's t-test; p = 0.0035; n = 11 (Fj^{GGG} OE) and 10 (Fj^{WT} OE) pupae; mean = 0.29 (Fj^{GGG} OE) and 0.39 (Fj^{WT} OE); 95% CI of the mean: ± 0.039 (Fj^{GGG} OE) and ± 0.050 (Fj^{WT} OE).

(F) The data sets are identical to those in Figure S1C. See the description of Figure S1C in this section.

(G) The data sets are identical to those in Figure S2E1-E2. See the description of Figure S2E1-E2 in this section.

(G') The data sets are identical to those in Figure S2E3-E4. See the description of Figure S2E3-E4 in this section.

Figure 4

(F2) Ds imbalance was statistically tested between indicated cell boundaries (paired t-test).

Cell boundaries #1 and #2: p = 0.00028; n = 8 pairs; mean of the difference = -0.24; 95% CI of the mean:of the difference: ± 0.043.

Cell boundaries #2 and #3: p = 0.014; n = 8 pairs; mean of the difference = -0.055; 95% CI of the mean:of the difference: ± 0.040.

Cell boundaries #3 and #4: p = 0.0013; n = 8 pairs; mean of the difference = -0.094; 95% CI of the mean:of the difference: ± 0.085.

(F3) Ds imbalance was statistically tested between indicated cell boundaries (paired t-test).

Cell boundaries #1 and #2: p = 0.0035; n = 8 pairs; mean of the difference = -0.19; 95% CI of the mean:of the difference: ± 0.10.

Cell boundaries #2 and #3: p = 0.029; n = 8 pairs; mean of the difference = -0.083; 95% CI of the mean:of the difference: ± 0.072.

Cell boundaries #3 and #4: p = 0.91; n = 8 pairs; mean of the difference = 0.0036; 95% CI of the mean:of the difference: ± 0.078.

Cell boundaries #4 and #5: p = 0.33; n = 6 pairs; mean of the difference = -0.037; 95% CI of the mean:of the difference: ± 0.089.

Cell boundaries #5 and #6: p = 0.94; n = 4 pairs; mean of the difference = -0.0012; 95% CI of the mean: ± 0.043.

Figure 6

Values of the displacement of the anterior and posterior borders of en (C1) or pnr (D1) domains along the A-P axis (μm) were compared between control and *ds* RNAi pupae.

(C1; left panel) Welch's t-test; p = 0.28; n = 4 (Control) and 5 (*ds* RNAi) pupae; mean =

71.3 (Control) and 53.8 (*ds* RNAi) μm; 95% CI of the mean: ± 39.6 (Control) and ± 21.4 (*ds* RNAi) μm.

(C1; right panel) Welch's t-test; p = 0.45; n = 4 (Control) and 5 (*ds* RNAi) pupae; mean = 66.4 (Control) and 51.2 (*ds* RNAi) μm; 95% CI of the mean: ± 50.9 (Control) and ± 26.3 (*ds* RNAi) μm.

(D1; left panel) Welch's t-test; p = 0.89; n = 4 (Control) and 5 (*ds* RNAi) pupae; mean = 49.7 (Control) and 48.9 (*ds* RNAi) μm; 95% CI of the mean: ± 11.1 (Control) and ± 14.4 (*ds* RNAi) μm.

(D1; right panel) Welch's t-test; p = 0.030; n = 4 (Control) and 5 (*ds* RNAi) pupae; mean = 38.9 (Control) and 9.72 (*ds* RNAi) μm; 95% CI of the mean: ± 24.3 (Control) and ± 20.9 (*ds* RNAi) μm.

Figure 7

(A) The data sets are identical to those in Figure S1C. See the description of Figure S1C in this section.

Figure S1

(C) Values of circular variances of indicated genotypes were compared with those of control (Dunnett's test).

Control: n = 5 pupae; mean = 0.33; 95% CI of the mean: ± 0.056

w RNAi: p = 1.0; n = 5 pupae; mean = 0.36; 95% CI of the mean: ± 0.064

ds RNAi: p = 0.00036; n = 5 pupae; mean = 0.58; 95% CI of the mean: ± 0.15

ds OE: p <0.001 ; n = 5 pupae; mean = 0.74; 95% CI of the mean: ± 0.070

ft RNAi: p = 0.019; n = 6 pupae; mean = 0.51; 95% CI of the mean: ± 0.10

dachs RNAi: p = 0.0054; n = 5 pupae; mean = 0.54; 95% CI of the mean: ± 0.17

fj RNAi: p = 0.39; n = 5 pupae; mean = 0.44; 95% CI of the mean: ± 0.060

fz RNAi: p = 0.97; n = 5 pupae; mean = 0.39; 95% CI of the mean: ± 0.20

fz OE: p = 1.0; n = 6 pupae; mean = 0.31; 95% CI of the mean: ± 0.038

wts RNAi: p = 0.79; n = 5 pupae; mean = 0.41; 95% CI of the mean: ± 0.074

hpo RNAi: p = 1.0; n = 4 pupae; mean = 0.37; 95% CI of the mean: ± 0.058

yki RNAi: p = 0.71; n = 4 pupae; mean = 0.42; 95% CI of the mean: ± 0.12

PI3K-CAAX OE: p = 0.70; n = 5 pupae; mean = 0.42; 95% CI of the mean: ± 0.077

PI3K^{DN} OE: p = 0.010; n = 4 pupae; mean = 0.54; 95% CI of the mean: ± 0.17

pk OE: p = 1.0; n = 5 pupae; mean = 0.31; 95% CI of the mean: ± 0.092

sple OE: p = 0.075; n = 5 pupae; mean = 0.49; 95% CI of the mean: ± 0.10

Figure S2

(D4; left panel) Values of the directionality were compared among indicated three groups (Tukey's test).

p = 0.70 (2 hr tracks by manual-Tracked by auto); 0.87 (2 hr tracks by manual-Not tracked by auto); 0.49 (Tracked by auto-Not tracked by auto)

2 hr tracks by manual: n = 358 cells; mean = 0.73; 95% CI of the mean: ± 0.021.

Tracked by auto: n = 120 cells; mean = 0.71; 95% CI of the mean: ± 0.038.

Not tracked by auto: n = 238 cells; mean = 0.74; 95% CI of the mean: ± 0.025.

(D4; right panel) Values of the velocity (µm/hr) were compared among indicated three groups (Tukey's test).

p = 0.92 (2 hr tracks by manual-Tracked by auto); 0.97 (2 hr tracks by manual- Not tracked by auto); 0.85 (Tracked by auto - Not tracked by auto).

2 hr tracks by manual: n = 358 cells; mean = 26.7; 95% CI of the mean: ±0.684.

Tracked by auto: n = 120 cells; mean = 26.9; 95% CI of the mean: ± 1.20.

Not tracked by auto: n = 238 cells; mean = 26.5; 95% CI of the mean: ± 0.839.

(E1; left panel) Values of the directionality of indicated genotypes were compared with those of control (Dunnett's test).

Control: n = 214 cells; mean = 0.53; 95% CI of the mean: ± 0.029.

ds RNAi: p = 1.0; n = 224 cells; mean = 0.54; 95% CI of the mean: ± 0.027.

ft RNAi: p = 1.0; n = 238 cells; mean = 0.53; 95% CI of the mean: ± 0.028.

d RNAi: p = 0.10; n = 207 cells; mean = 0.48; 95% CI of the mean: ± 0.029.

fj RNAi: p = 0.21; n = 191 cells; mean = 0.49; 95% CI of the mean: ± 0.030.

wts RNAi: p = 0.077; n = 233 cells; mean = 0.48; 95% CI of the mean: ± 0.027.

hpo RNAi: p < 0.001 ; n = 176 cells; mean = 0.42; 95% CI of the mean: ± 0.031.

ds OE: p = 0.00012; n = 274 cells; mean = 0.45; 95% CI of the mean: ± 0.026.

PI3K-CAAX OE: p = 0.027; n = 200 cells; mean = 0.59; 95% CI of the mean: ± 0.033.

PI3K^{DN} OE: p < 0.001; n = 219 cells; mean = 0.40; 95% CI of the mean: ± 0.025.

(E1; right panel)

Welch's t-test; p = 0.391; n = 482 (Fj^{GGG} OE) and 465 (Fj^{WT} OE) cells; mean = 0.67 (Fj^{GGG} OE) and 0.66 (Fj^{WT} OE); 95% CI of the mean: ± 0.020 (Fj^{GGG} OE) and ± 0.019 (Fj^{WT} OE).

(E2; left panel) Values of the velocity of indicated genotypes were compared with those of control (Dunnett's test).

Control: n = 214 cells; mean = 18.0; 95% CI of the mean: ± 0.790.

ds RNAi: p = 0.82; n = 224 cells; mean = 17.4; 95% CI of the mean: ± 0.754.

ft RNAi: p = 0.60; n = 238 cells; mean = 18.8; 95% CI of the mean: ± 0.738.

d RNAi: p = 0.073; n = 207 cells; mean = 16.6; 95% CI of the mean: ± 0.748.

fj RNAi: p = 1.0; n = 191 cells; mean = 18.2; 95% CI of the mean: ± 0.814.

wts RNAi: p = 0.024; n = 233 cells; mean = 16.4; 95% CI of the mean: ± 0.739.

hpo RNAi: p < 0.001; n = 176 cells; mean = 14.3; 95% CI of the mean: ± 0.691.

ds OE: p < 0.001; n = 274 cells; mean = 14.6; 95% CI of the mean: ± 0.540.

PI3K-CAAX OE: p < 0.001; n = 200 cells; mean = 23.8; 95% CI of the mean: ± 1.21.

PI3K^{DN} OE: p < 0.001; n = 219 cells; mean = 12.0; 95% CI of the mean: ± 0.546.

(E2; right panel)

Welch's t-test; p = 0.0041; n = 482 (Fj^{GGG} OE) and 465 (Fj^{WT} OE) cells; mean = 25.4 (Fj^{GGG} OE) and 24.1 (Fj^{WT} OE); 95% CI of the mean: ± 0.673 (Fj^{GGG} OE) and ± 0.566 (Fj^{WT} OE).

(E3; left panel) Values of the directionality of indicated genotypes were compared with those of control (Dunnett's test).

Control: n = 124 cells; mean = 0.81; 95% CI of the mean: 0.021.

ds RNAi: p < 0.001; n = 138 cells; mean = 0.68; 95% CI of the mean: ± 0.036.

ft RNAi: p < 0.001; n = 157 cells; mean = 0.70; 95% CI of the mean: ± 0.029.

d RNAi: p < 0.001; n = 112 cells; mean = 0.66; 95% CI of the mean: ± 0.036.

fj RNAi: p < 0.001; n = 111 cells; mean = 0.70; 95% CI of the mean: ± 0.039.

wts RNAi: p < 0.001; n = 155 cells; mean = 0.69; 95% CI of the mean: ± 0.031.

hpo RNAi: p < 0.001; n = 102 cells; mean = 0.67; 95% CI of the mean: ± 0.044.

ds OE: p < 0.001; n = 189 cells; mean = 0.48; 95% CI of the mean: ± 0.033.

PI3K-CAAX OE: p = 0.26; n = 126 cells; mean = 0.76; 95% CI of the mean: ± 0.033.

PI3K^{DN} OE: p < 0.001; n = 222 cells; mean = 0.61; 95% CI of the mean: ± 0.029.

(E3; right panel)

Welch's t-test; p < 0.001; n = 406 (Fj^{GGG} OE) and 349 (Fj^{WT} OE) cells; mean = 0.82 (Fj^{GGG} OE) and 0.78 (Fj^{WT} OE); 95% CI of the mean: ± 0.013 (Fj^{GGG} OE) and ± 0.016 (Fj^{WT} OE).

(E4; left panel) Values of the velocity of indicated genotypes were compared with those of control (Dunnett's test).

Control: n = 124 cells; mean = 33.7; 95% CI of the mean: ± 1.23.

ds RNAi: p < 0.001; n = 138 cells; mean = 28.7; 95% CI of the mean: ± 1.19.

ft RNAi: p < 0.001; n = 157 cells; mean = 28.9; 95% CI of the mean: ± 1.03.

d RNAi: p < 0.001; n = 112 cells; mean = 27.2; 95% CI of the mean: ± 1.18.

fj RNAi: p = 0.41; n = 111 cells; mean = 32.2; 95% CI of the mean: ± 1.08.

wts RNAi: p < 0.001; n = 155 cells; mean = 26.8; 95% CI of the mean: ± 1.12.

hpo RNAi: p < 0.001; n = 102 cells; mean = 25.4; 95% CI of the mean: ± 1.36.

ds OE: p < 0.001; n = 189 cells; mean = 21.9; 95% CI of the mean: ± 0.838.

PI3K-CAAX OE: p = 0.17; n = 126 cells; mean = 31.8; 95% CI of the mean: ± 1.62.

PI3K^{DN} OE: p < 0.001; n = 222 cells; mean = 18.6; 95% CI of the mean: ± 0.871.

(E4; right panel)

Welch's t-test; p < 0.001; n = 406 (Fj^{GGG} OE) and 349 (Fj^{WT} OE) cells; mean = 35.3 (Fj^{GGG} OE) and 32.1 (Fj^{WT} OE); 95% CI of the mean: ± 0.676 (Fj^{GGG} OE) and ± 0.802 (Fj^{WT} OE).

Figure S4

See the section "Analysis of movement directions, apoptosis, cell rearrangements, cell area changes, and roundness changes of LECs" in STAR Methods for details of parameters below:

(A") Values of "Cell size change" were compared between control and *ds* RNAi pupae. Welch's t-test; p = 0.064; n = 259 (control) and 307 (*ds* RNAi) cells; mean = 1.10 (control) and 1.02 (*ds* RNAi); 95% CI of the mean: ± 0.0602 (control) and ± 0.0558 (*ds* RNAi).

(B") Values of "Roundness change" were compared between control and *ds* RNAi pupae. Welch's t-test; p = 0.36; n = 259 (control) and 307 (*ds* RNAi) cells; mean = 1.51 (control) and 1.46 (*ds* RNAi); 95% CI of the mean: ± 0.0829 (control) and ± 0.0763 (*ds* RNAi).

(C") Values of "Neighbors lost per cell" were compared between control and *ds* RNAi pupae.

Welch's t-test; p = 0.11; n = 5 (control) and 5 (*ds* RNAi) pupae; mean = 0.0368 (control) and 0.0849 (*ds* RNAi); 95% CI of the mean: ± 0.0462 (control) and ± 0.0585 (*ds* RNAi).

(D) Values of "Cell elimination rate" were compared between control and *ds* RNAi pupae. Welch's t-test; p = 0.54; n = 5 (control) and 5 (*ds* RNAi) pupae; mean = 0.0915 (control) and 0.111 (*ds* RNAi); 95% CI of the mean: ± 0.249 (control) and ± 0.216 (*ds* RNAi).

(E') Values of segment width (μm) at 23 hr APF were compared with those at 27 hr APF. Control: paired t-test; p= 0.48; n = 11 pupae; mean of the difference = 3.71; 95 % CI of the mean of the difference: ± 11.3.

ds RNAi: paired t-test; p= 0.97; n = 9 pupae; mean of the difference = -0.24; 95 % CI of the mean of the difference: 12.7.

Figure S6

(C4) *D*E-cadherin imbalance was statistically tested between indicated cell boundaries (paired t-test).

Cell boundaries #1 and #2: p = 0.00084; n = 12 pairs; mean of the difference = 0.070; 95% CI of the mean:of the difference: ± 0.034.

Cell boundaries #2 and #3: p = 0.0030; n = 12 pairs; mean of the difference = 0.088; 95% CI of the mean:of the difference: ± 0.051.

Cell boundaries #3 and #4: p = 0.079; n = 12 pairs; mean of the difference = 0.050; 95% CI of the mean:of the difference: ± 0.057.

Cell boundaries #4 and #5: p = 0.50; n = 11 pairs; mean of the difference = 0.024; 95% CI of the mean:of the difference: ± 0.076.

Cell boundaries #5 and #6: p = 0.037; n = 6 pairs; mean of the difference = 0.14; 95% CI of the mean:of the difference: ± 0.13.

(D4) *D*E-cadherin imbalance was statistically tested between indicated cell boundaries (paired t-test).

Cell boundaries #1 and #2: p = 0.072; n = 12 pairs; mean of the difference = 0.056; 95% CI of the mean:of the difference: ± 0.062.

Cell boundaries #2 and #3: p = 0.43; n = 12 pairs; mean of the difference = 0.035; 95% CI of the mean:of the difference: ± 0.095.

Cell boundaries #3 and #4: p = 0.12; n = 12 pairs; mean of the difference = 0.055; 95% CI of the mean:of the difference: ± 0.071.

Cell boundaries #4 and #5: p = 0.029; n = 12 pairs; mean of the difference = 0.083; 95% CI of the mean:of the difference: ± 0.073.

Cell boundaries #5 and #6: p = 0.0070; n = 12 pairs; mean of the difference = 0.12; 95% CI of the mean:of the difference: ± 0.082.

Cell boundaries #6 and #7: p = 0.96; n = 6 pairs; mean of the difference = 0.0043; 95% CI of the mean:of the difference: ± 0.21.

(E4) Ds imbalance was statistically tested between indicated cell boundaries (paired t-test).

Cell boundaries #1 and #2: p = 0.0023; n = 8 pairs; mean of the difference = -0.098; 95% CI of the mean:of the difference: ± 0.050.

Cell boundaries #2 and #3: p = 0.0055; n = 8 pairs; mean of the difference = -0.055; 95% CI of the mean:of the difference: ± 0.033.

Cell boundaries #3 and #4: p = 0.026; n = 8 pairs; mean of the difference = -0.059; 95% CI of the mean:of the difference: ± 0.050.

Cell boundaries #4 and #5: p = 0.0041; n = 7 pairs; mean of the difference = -0.12; 95% CI of the mean:of the difference: ± 0.065.

Cell boundaries #5 and #6: p = 0.049; n = 5 pairs; mean of the difference = -0.065; 95% CI of the mean:of the difference: ± 0.065.

(F4) Ds imbalance was statistically tested between indicated cell boundaries (paired t-test).

Cell boundaries #1 and #2: p = 0.00070; n = 8 pairs; mean of the difference = -0.12; 95% CI of the mean:of the difference: ± 0.049.

Cell boundaries #2 and #3: p = 0.12; n = 8 pairs; mean of the difference = -0.026; 95% CI of the mean:of the difference: ± 0.035.

Cell boundaries #3 and #4: p = 0.36; n = 8 pairs; mean of the difference = -0.024; 95% CI of the mean:of the difference: ± 0.057.

Cell boundaries #4 and #5: p = 0.0054; n = 7 pairs; mean of the difference = -0.066; 95% CI of the mean:of the difference: ± 0.038.

Cell boundaries #5 and #6: p = 0.80; n = 5 pairs; mean of the difference = 0.0089; 95% CI of the mean:of the difference: ± 0.090.

(C5) *D*E-cadherin imbalance was statistically tested between indicated cell boundaries (paired t-test).

Cell boundaries #1 and #2: p = 0.0046; n = 13 pairs; mean of the difference = 0.10; 95% CI of the mean:of the difference: ± 0.064.

Cell boundaries #2 and #3: p = 0.11; n = 13 pairs; mean of the difference = 0.038; 95% CI of the mean:of the difference: ± 0.048.

Cell boundaries #3 and #4: p = 0.056; n = 13 pairs; mean of the difference = 0.084; 95% CI of the mean:of the difference: ± 0.087.

Cell boundaries #4 and #5: p = 0.61; n = 11 pairs; mean of the difference = 0.020; 95% CI of the mean:of the difference: ± 0.085.

(D5) *D*E-cadherin imbalance was statistically tested between indicated cell boundaries (paired t-test).

Cell boundaries #1 and #2: p = 0.10; n = 12 pairs; mean of the difference = -0.029; 95% CI of the mean:of the difference: ± 0.035.

Cell boundaries #2 and #3: p = 0.0063; n = 12 pairs; mean of the difference = 0.088; 95% CI of the mean:of the difference: ± 0.057.

Cell boundaries #3 and #4: p <0.001; n = 12 pairs; mean of the difference = 0.15; 95% CI of the mean:of the difference: ± 0.048.

Cell boundaries #4 and #5: p = 0.24; n = 11 pairs; mean of the difference = 0.034; 95%

CI of the mean:of the difference: ± 0.062.

Cell boundaries #5 and #6: p = 1.0; n = 4 pairs; mean of the difference = 0.00060; 95% CI of the mean:of the difference: ± 0.15.

(E5) The data sets are identical to those in Figure 4F2. See the description of Figure 4F2 in this section.

(F5) The data sets are identical to those in Figure 4F3. See the description of Figure 4F3 in this section.

KEY RESOURCES TABLE

REAGENT or RESOURCE	SOURCE	IDENTIFIER
Antibodies		
Mouse anti-Engrailed monoclonal antibody; 4D9	Patel et al. 1989; DSHB	Antibody Registry ID: AB_528224
Rabbit anti-GFP polyclonal antibody	Life Technologies	Cat#A6455
Bacterial and Virus Strains		
N/A	N/A	N/A
Biological Samples		
N/A	N/A	N/A
Chemicals, Peptides, and Recombinant Proteins		
Alexa Fluor 546 conjugate	Molecular Probes	Cat#A22283
VECTASHIELD Mounting Medium with DAPI	Vector Laboratories	Cat#H-1200
Critical Commercial Assays		
N/A	N/A	N/A
Deposited Data		

N/A	N/A	N/A
Experimental Models: Cell Lines		
N/A	N/A	N/A
Experimental Models: Organisms/Strains		
D. melanogaster; Ay-GAL4	Ito et al, 1997	FlyBase: FBti0012290
D. melanogaster; engrailed(en)-GAL4	Bloomington Drosophila Stock Center	FlyBase: FBti0003572
D. melanogaster; four-jointed(fj)-GAL4; fj[VG1]	Tang and Sun 2002	FlyBase: FBti0024272
D. melanogaster; pannier(pnr)-GAL4; pnr[MD237]	Calleja et al., 1996	FlyBase: FBti0004011
D. melanogaster; tubulin(tub)-GAL4	Lee and Luo, 1999	FlyBase: FBti0012687
D. melanogaster; DE-cadherin:GFP; shg[GFP]	Huang et al., 2009	FlyBase: FBti0168565
D. melanogaster; DE-cadherin:mTomato; shg[mTomato]	Huang et al., 2009	FlyBase: FBti0168570
D. melanogaster; dachs:GFP; d:GFP[VK19]	Bosveld et al. 2012	FlyBase: FBal0269880
D. melanogaster; EGFP:dachs; Act>stop>EGFP-dachs	Brittle et al., 2012	N/A
D. melanogaster;dachsous:EGFP	Brittle et al., 2012	N/A
D. melanogaster;fat:EGFP	Brittle et al., 2012	N/A
D. melanogaster;scribble:GFP; scribble[CA07683]	Buszczak et al., 2007	FlyBase: FBti0099928
D. melanogaster;His2Av:GFP[S65T]	Clarkson and Saint, 1999	FlyBase: FBal0104781
D. melanogaster;20xUAS-IVS-mCD8:GFP	Bloomington Drosophila Stock Center	FlyBase: FBti0131936

D. melanogaster;UAS-mCD8:3xEGFP	Shimono et al., 2009	N/A
D. melanogaster;UAS-EGFP	Bloomington Drosophila Stock Center	FlyBase: FBti0013987
D. melanogaster;UAS-mCherry:CAAX	Kakihara et al., 2008	FlyBase: FBtp0041366
D. melanogaster;UAS-myr-mRFP	Bloomington Drosophila Stock Center	FlyBase: FBti0027895
D. melanogaster;ubi-mRFP.nls	Bloomington Drosophila Stock Center	FlyBase: FBti0141172
D. melanogaster;UAS-w-RNAi; *w[GL00094]*	Bloomington Drosophila Stock Center	FlyBase: FBti0144194
D. melanogaster;UAS-ds-RNAi; *ds[HMS00759]*	Bloomington Drosophila Stock Center	FlyBase: FBti0140473
D. melanogaster;UAS-ft-RNAi; *ft[HMS00932]*	Bloomington Drosophila Stock Center	FlyBase: FBti0144840
D. melanogaster;UAS-d-RNAi; *d[HMS01096]*	Bloomington Drosophila Stock Center	FlyBase: FBti0140791
D. melanogaster;UAS-fj-RNAi; *fj[HMS01310]*	Bloomington Drosophila Stock Center	FlyBase: FBti0140934
D. melanogaster;UAS-fz-RNAi; *fz[HMS01308]*	Bloomington Drosophila Stock Center	FlyBase: FBti0140932
D. melanogaster;UAS-fz1-1	Boutros et al., 2000	FlyBase: FBti0148929
D. melanogaster;UAS-wts-RNAi; *wts[HMS00026]*	Bloomington Drosophila Stock Center	FlyBase: FBti0144688
D. melanogaster;UAS-hpo-RNAi; *hpo[JF02740]*	Bloomington Drosophila Stock Center	FlyBase: FBti0128842
D. melanogaster;UAS-yki-RNAi; *yki[JF03119]*	Bloomington Drosophila Stock Center	FlyBase: FBti0130373
D. melanogaster;UAS- *yki .S111A.S168A.S250A.V5*	Oh and Irvine, 2009; Bloomington Drosophila Stock Center	FlyBase: FBti0127382
D. melanogaster;UAS-PI3K-CAAX; *Pi3K92E[Scer\UAS.T:Hsap\MYC,T:Hsa* *p\CAAX]*	Leevers et al., 1996	FlyBase: FBti0114085
D. melanogaster;UAS-PI3K^{DN}; *Pi3K92E[D954A.Scer\UAS.T:Hsap\MYC* *]*	Leevers et al., 1996	FlyBase: FBti0114081

D. melanogaster;UAS-pk	Gubb et al., 1999	FlyBase: FBti0148926
D. melanogaster;UAS-sple	Gubb et al., 1999	FlyBase: FBti0148928
D. melanogaster;sple[NP2567]; pk[NP2567]	Hayashi et al., 2002	FlyBase: FBti0034927
D. melanogaster;UAS-GPH	Pickering et al., 2013	
D. melanogaster;dachs[210]	Buckles et al., 2001	FlyBase: FBal0127240
D. melanogaster;dachs[GC13]	Mao et al., 2006	FlyBase: FBal0128007
D. melanogaster;Kst[GFSTF]; kst[MI03134-GFSTF.1]	Nagarkar-Jaiswal et al., 2015	FlyBase: FBti0178294
D. melanogaster;hs-flp22	Chou and Perrimon, 1996	FlyBase: FBti0000785
D. melanogaster;GS-ds	Toba et al., 1999	FlyBase: FBti0072213
D. melanogaster;diap1-GFP.3.5	Zhang et al., 2008	FlyBase: FBal0239744
D. melanogaster;FRT-40A	Xu and Rubin, 1993	FlyBase: FBti0002071
D. melanogaster;FRT-82B	Xu and Rubin, 1993	FlyBase: FBti0002074
D. melanogaster;UAS-ds:EGFP	This study	N/A
D. melanogaster;UAS-fj:mCherry-CAAX	This study	N/A
D. melanogaster;UAS-fjGGG:mCherry-CAAX	This study	N/A
Oligonucleotides		
N/A	N/A	N/A
Recombinant DNA		
pUASTattB-fj:mCherry	This study	N/A
pUASTattB-fj[GGG]:mCherry	This study	N/A
pUAST-ds:EGFP	This study	N/A
Software and Algorithms		
ImageJ	NIH	https://imagej.nih.gov/ij/
R	R Core Team (2016)	https://www.r-project.org/
Other		

N/A	N/A	N/A

Supplemental Movies

Movie S1. Movements of wild type or *ds* knockdown LECs (Related to Figure 1)

Time-lapse recording of nuclei (left column) of wild type (top) or *ds* knockdown (bottom) LECs and their trajectories (right column, see the legend of Figure 1**B** for details). Snapshots from this movie are provided in Figure 1**A"**, 1**C1**-1**C4**, and 1**D1**-1**D4**. Scale bar: 100 µm. Exact genotypes of animals used in this and subsequent movies are described in STAR Methods unless described otherwise.

Movie S2. Localization of GPH at posterior cell boundaries during the posterior migration (Related to Figure 1 and S3)

Z stack of wild-type LECs at 26 hr APF (upper row) or *ds*-knockdown LECs at 26 hr 15 min APF (lower row) that were clonally expressing GPH (left column) and mCherry:CAAX (right column). Images were acquired along the apico-basal cell axis at 0.5 µm intervals. Movie begins from the most apical plane and is shifted basally. White and cyan arrows indicate GPH-enriched and GPH–poor cell boundaries respectively. Scale bar: 30 µm.

Movie S3. The distribution of β-heavy Spectrin (β$_H$-Spec)/Karst (Kst) in migrating LECs (Related to Figure 1 and S3)

Z stack of wild-type LECs at 26 hr APF that were expressing β$_H$-Spec^{GFSTF} (left and green in the right panel) and *D*E-cadherin:mTomato (middle and magenta in the right panel). Images were acquired along the apico-basal cell axis at 0.5 µm intervals. Movie begins from the most apical plane and is shifted basally. White arrows indicate masses of β$_H$-Spec signals (β$_H$-Spec bodies). Scale bar: 30 µm.

Movie S4. A clone-autonomous defect of *ds* knockdown or overexpression on posterior migration (Related to Figure 1)

Time-lapse recording of LECs where *ds* was clonally knocked down (left; *ds* RNAi) or overexpressed (right; *ds* OE; see details for STAR Methods). *ds* knockdown or overexpressing LECs are labeled with mCD8:GFP or mCherry:CAAX (magenta in the right panel). Arrow: *ds* overexpressing LECs that moved abnormally. The magenta bar in the first seven frames of the right movie labels the estimated position of the posterior compartment. Scale bar: 50 µm (left panel) and 100 µm (right panel). Genotype: *hs-flp22/X or Y; Ay-GAL4, UAS-mCherry:CAAX/+; 20xUAS-IVS-mCD8:GFP/UAS-ds RNAi* (*ds* RNAi). *hs-flp22/X or Y; Ay-GAL4, UAS-mCherry:CAAX/GS-ds; His2Av:GFP^{S65T}/+*

(*ds* OE).

Movie S5. Movements of *en* domains in wild type and *ds* knockdown LECs (Related to Figure 6)

Time-lapse recording of *en* domains labeled with myr-mRFP. Data sets of control (left panel) and *ds* knockdown LECs (right panel) are included (see the legend of Figure 6**B-C4** for details). Snapshots from this movie are provided in Figure 6**C3** and **C4**. Scale bar: 100 µm.

Movie S6. Movements of *pnr* domains in wild-type and *ds* knockdown LECs (Related to Figure 6)

Time-lapse recording of *pnr* domains that were labeled with mCD8:3xEGFP. Data sets of control (left panel) and *ds* knockdown (right panel) are included (see the legend of Figure 6**D1-D4** for details). Snapshots from this movie are provided in Figure 6**D3** and **D4**. Scale bar: 100 µm.

Movie S7. Movements of *ft* or *dachs* knockdown LECs (Related to Figure 7)

Time-lapse recording of nuclei of *ft* (top) or *dachs* (bottom) knockdown LECs (left panel) and their trajectories (right panel, see the legend of Figure 1B for details). Scale bar: 100 µm.

Supplemental Figures

A

Pupal case
Cuticle
Lamellipodia
LECs

Apical
Basal

Anterior
Posterior

Anterior
Posterior

B

A2 A3

C

Variance

*** *** * ** *

Control, *w* RNAi, *ds* RNAi, *ds* OE, *ft* RNAi, *dachs* RNAi, *fj* RNAi, *fz* RNAi, *fz* OE, *wts* RNAi, *hpo* RNAi, *yki* RNAi, *PI3K-CAAX* OE, *PI3K^DN* OE, *pk* OE, *sple* OE

Later stage

Nuclei

D1

Earlier stage

Nuclei

D2

Nuclei
Posterior compartment

D3

18 hr APF

E1

24 hr APF

E2

26 hr APF

E3

30 hr APF

E4

Ds:EGFP

pnr-GAL4

F1

Engrailed (En)

F2

pnr-GAL4 En

F3

Control

72

Figure S1. Anatomical configuration of the tissues and LECs, and Ds:EGFP distributions at different time points (Related to Figure 1, 2, 3, 6 and 7).

(**A**) Diagrams of the dorsal front view of a pupa (left) and the cross sectional view of an abdominal subregion (blue box) to highlight the epidermal tissue architecture (right). The cuticle (cyan) lies between the pupal case (brown) and the LECs. LECs adhere to the cuticle (Ninov et al., 2010) and lamellipodia (orange) are formed at the posterior apical surface of LECs, which implies that forces exerted by lamellipodia on the cuticle drive the LECs (Bischoff, 2012). Anterior (A) is to the left and posterior (P) is to the right and all photos are dorsal front views hereafter, unless described otherwise.

(**B**) Anatomy of the Drosophila abdomen. A diagram of the dorsal view of the Drosophila abdomen that consists of eight segments. Yellow dotted lines indicate the segment borders. In this study, we focused on the abdominal segment A2 and A3. Acquired images of the boxed region are shown in **F1-F3**.

(**C**) A plot of circular variances of LEC movements in pupae of the control and with the indicated genetic conditions. The representative two-hour time window was selected for each pupa. Data are shown as a dot plot with the mean (black dot) $\pm$ the 95% CI. Dunnett's test; ***: p<0.001, **: p<0.01, *: p<0.05. In addition to *dachs* RNAi, we observed LEC movements in *dachs* mutants (*dachs²¹⁰/dachs^{GC13}*; Mao et al., 2006; Buckles et al., 2001) and found the similar defect (data not shown). As we discuss in the end of the section "A subset of LECs in the anterior compartment depend on Ds for their posterior migration, but LECs in the posterior compartment do not" in Results, we overexpressed *pk* (*pk* OE in **C**) or *sple* (*sple* OE in **C**) in LECs to verify whether the hypothetical Sple/Pk dependent mechanism underlies the difference between Ds-dependent and independent migration of LECs. Our working hypothesis would be that Sple is predominanly expressed in the Ds uphill (overlapped with the anterior compartment), where Ds controls the migration of LEC by way of Sple. As a consequence, *sple* is necessary for the posterior migration of LEC, which may be disturbed by ectopic expression of *pk*. However our results suggest that the hypothetical Sple/Pk dependent mechanism does not make a significant contribution to the *ds*-dependent and independent migration of LECs. Neither *sple* nor *pk* mutants exhibited significant defects in LEC migration (data not shown). Overexpression of *pk* did not, either (*pk* OE in **C**). Overexpression of *sple* reversed the direction of the migration of LECs in the anterior compartment that endogenously expresses *sple* (visualized by using an enhancer trap strain *pk^{NP2567}*), but not in the posterior compartment

73

where *pk* is presumably dominant (data not shown; *sple* OE in **C**).

(**D1-D3**) Estimation of approximate positions of posterior compartments with the help of time-lapse recordings of pupae that expressed *His2Av:GFP[S65T]* (a nuclear marker; green in **D3**). We first observe frames at later stages (e.g. at 29 hr APF like **D1**), and mark nuclei of LECs on the segment border (cyan dots and the yellow line in **D1**) on the basis of the relative position to expanding histoblast nests (asterisks in **D1**). We then retrospectively tracked those marked nuclei at earlier stages (e.g. at 24 hr APF in **D2** and **D3**), which allows us to presume positions of segment borders. At the early stage, it is known that the A/P compartment border is approximately mapped at three-four cells anterior to the segment border (see **F2**). Taken together, we can estimate the approximate position of the posterior compartment (magenta bars at the bottom of **D2**), which is verified by a marker for the posterior compartment (*en-Gal4>mmRFP*; magenta in **D3**).

(**E1-E4**) The subcellular localization of Ds:EGFP at different time points. Before LECs started to migrate (**E1**; 18 hr APF), the Ds:EGFP localization at cell boundaries was not apparently polarized as shown by signals at D-V cell boundaries (an arrow) and punctate Ds:EGFP signals (white arrowheads) were seen in the cytoplasm. Once LECs initiated posterior migration, the Ds:EGFP localization at cell boundaries became polarized at the anterior-posterior cell boundaries (**E2** and **E3**; 24 and 26 hr APF, respectively; see an example of quantification of 26 hr data in Figure 2**A'**) and the punctate signals in the cytoplasm disappeared (**E3** and **E4**; 26 and 30 hr APF, respectively). Scale bars: 30 µm.

(**F1-F3**) A control 24 hr APF pupae which was double labeled for the *pnr* domain (**F1**; *pnr-GAL4>mCherry:CAAX*) and for the posterior compartment by using the anti-Engrailed (En) antibody (**F2**). The En staining defines A/P compartment borders (cyan dotted lines), segment borders (yellow dotted lines), and the posterior compartments (magenta bars at the bottom). In the merged image of the control pupa (**F3**), the *pnr* domain (green) straddles the A/P compartment border and comprises large portions of both the anterior compartment and the posterior compartment (magenta partly overlapped with green). Scale bars: 100µm.
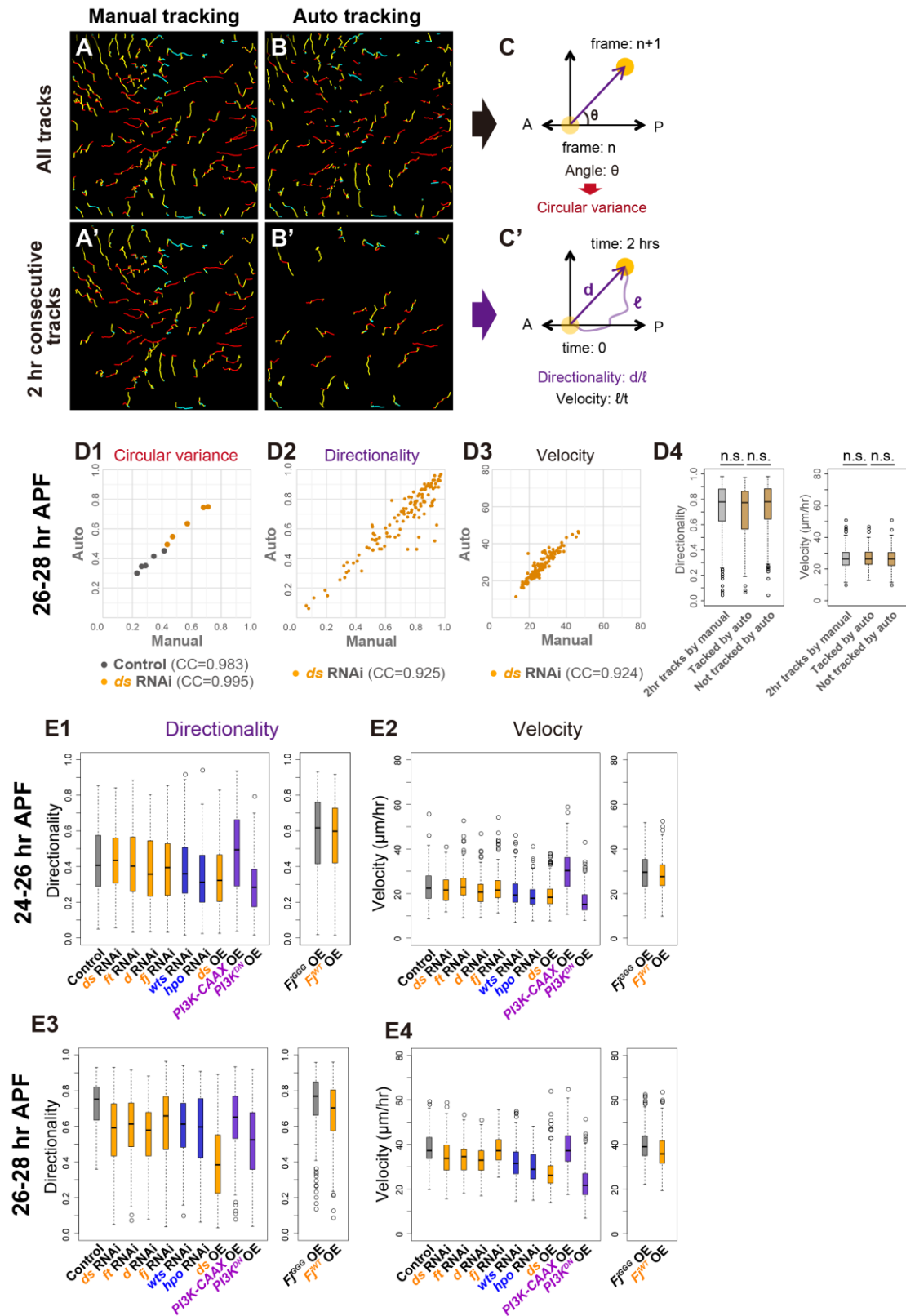
Figure S2. Quantification of angles, velocities and directionalities of LEC

movements (Related to Figure 1, 2, 3, 5 and 7).

(**A-C'**) Having started from a recording of *ds*-depleted LECs during 26-28 hr APF (after puparium formation), we made two datasets of tracks by using either manual tracking (**A** and **A'**) or our auto tracking method (**B**, and **B'**; see STAR METHODS for details). To compare the two datasets and validate our auto tracking data (see next in **D1-D4**), we calculated the following parameters regarding movements of individual LEC nuclei: angle (θ in **C**), directionality (the ratio of the net displacement to the total path length; d/l in **C'**) and mean velocity (l/t in **C'**), by using each dataset.
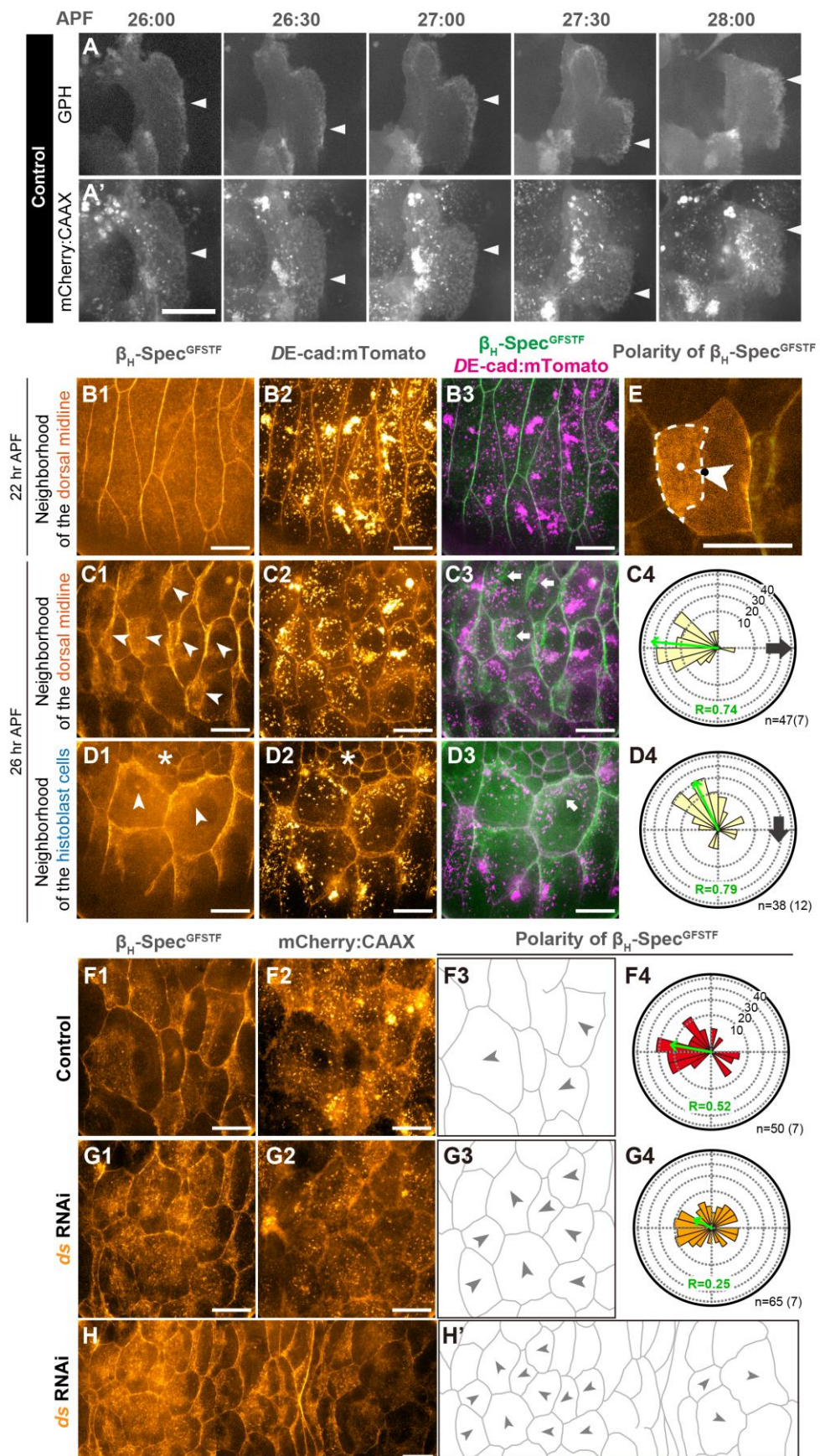
Whether each LEC nuclei was successfully tracked throughout the two hours or not, an angle was calculated by using one time frame (n) and the next one (n+1) as far as the same nuclei was tracked between the two frames (**C**). So, essentially all tracks in each recording (**A** and **B**) were used for calculating the circular variance of angles of LEC movements. In contrast, in quantifying the mean velocity and the directionality (the directionality in particular), it was required to use tracks of individual LECs that were identified consecutively throughout the time window (**C'**). However, this was technically challenging in collective cell migration, because LECs often came in close contact with non-LEC signals or with other LECs, where our auto tracking did not necessarily distinguish individual cells (**B**) and only manual tracking managed to do (**A**). In addition, some LECs underwent apoptosis or moved out of the recording field, which forced tracking terminated. As a consequence, tracks of LECs that were identified consecutively for two hours (2 hr consecutive tracks; new Figure S2B') by auto tracking comprised one-third to one-half of those made by the manual tracking (new Figure S2A'). The number of the 2 hr consecutive auto tracks was 32 (**B'**) in contrast to 79 2 hr consecutive manual tracks (**A'**). As explained next, we validated our auto tracking method and used only those 2 hr consecutive tracks for calculating the directionality and the velocity of LEC movements (**C'**).

(**D1-D4**) Validation of our auto tracking method. (**D1**) Regarding circular variances of angles, we used all tracks for the calculation, and compared the values of the manual datasets with those of the auto datasets. (**D2-D3**) In the auto tracking dataset, we selected the 2 hr consecutive tracks (the 2 hr consecutive auto tracks) and compared their values of the directionality and the velocity with those of the correspondent 2 hr consecutive manual tracks (**D2** and **D3**, respectively). Each data point represents the value of each pupa (**D1**) or each nucleus (**D2** and **D3**). Data of control (gray dots in **D1**) or *ds*-depleted pupae (orange dots in **D1-D3**) are shown. Note large correlation coefficients (CCs) in all

76

of the comparisons of the parameter values obtained by the two methods (0.924-0.995 in **D1-D3**). (**D4**) To assess whether extracted 2 hr consecutive auto tracks may represent all tracks or not, we collected total 358 2 hr consecutive manual tracks from 5 *ds*-depleted pupae ("2 hr tracks by manual" in **D4**). Out of those, 120 were identified consecutively also by the auto tracking ("Tracked by auto") whereas the remaining 238 were not ("Not tracked by auto"). No statistically significant difference in values of directionality or velocity was found among the indicated three groups (n.s.: not significant; Tukey's test). Overall, our auto tracking method is reliable to analyze LEC movements.

(**E1-E4**) The directionality (**E1** and **E3**) and the mean velocity (**E2** and **E4**) of LEC movements in various genotypes at the indicated APF, which were obtained by using 2 hr consecutive auto tracks. Data are shown as box-and-whisker plots. n = 100-300 cells (4-6 pupae), except for Fj^{GGG} OE and Fj^{WT} OE where n were 350-500 cells (11 pupae).

APF 26:00 26:30 27:00 27:30 28:00 Figure S3

Control

A GPH

A' mCherry:CAAX

| β$_H$-Spec^{GFSTF} | DE-cad:mTomato | β$_H$-Spec^{GFSTF} DE-cad:mTomato | Polarity of β$_H$-Spec^{GFSTF} |

22 hr APF — Neighborhood of the dorsal midline

B1 **B2** **B3** **E**

26 hr APF

Neighborhood of the dorsal midline

C1 **C2** **C3** **C4** R=0.74 n=47(7)

Neighborhood of the histoblast cells

D1 * **D2** * **D3** **D4** R=0.79 n=38 (12)

| β$_H$-Spec^{GFSTF} | mCherry:CAAX | Polarity of β$_H$-Spec^{GFSTF} |

Control

F1 **F2** **F3** **F4** R=0.52 n=50 (7)

ds RNAi

G1 **G2** **G3** **G4** R=0.25 n=65 (7)

ds RNAi

H **H'**

78

Figure S3. The distribution of GPH and β-heavy Spectrin (βH-Spec)/Karst (Kst) in migrating LECs and the effect of *ds* knockdown (Related to Figure 1).

(**A** and **A'**) Snapshots of migrating LECs that were clonally co-expressing a lamellipodia marker, GPH, and a membrane marker, mCherry:CAAX. APF (after puparium formation) is indicated on top of the snapshots. GPH was enriched at the posterior cell edges, whereas mCherry:CAAX was not (arrowheads).

(**B1-E**) Two-color imaging of βH-Spec (βH-Spec^{GFSTF}; **B1**, **C1**, **D1**, and **E**; green in **B3**, **C3**, and **D3**) and *D*E-cadherin:mTomato (*D*E-cad:mTomato; **B2**, **C2**, and **D2**; magenta in **B3**, **C3**, and **D3**) of the wild-type LECs. The subcellular distribution of βH-Spec dynamically changed before and after the onset of the migration. (**B1-B3**) At 22 hr APF, approximately 2 hours before LECs started posterior migration, βH-Spec was uniformly distributed at the apical surface and cell boundaries in each LEC. (**C1-D3**) LECs in the posterior migration phase (**C1-C3**) and those in the dorsal migration phase (**D1-D3**). At the rears inside migrating LECs, masses of βH-Spec signals are often seen (pointed with arrows in **C3** and **D3**, outlined with a white broken line in **E,** and designated as "βH-Spec bodies"). Asterisks (**D1** and **D2**) mark histoblast cells. (**C4**, **D4,** and **E**) We evaluated the bias in the subcellular distribution of the βH-Spec body as follows: We first outlined the βH-Spec body (white broken line in **E**) and calculated the position of the center of its mass (white dot in **E**). Arrowheads are placed at the centers of mass of individual LECs (black dot in **E**) and point at the centers of mass of the βH-Spec body. Angles of the arrowheads are plotted on rose diagrams (**C4** and **D4**). The mean angles are represented by green arrows and the arrow length "R" indicates one minus circular variance. The rose diagram consists of 24 bins of 15° each and dotted concentric circles are drawn in 10% increments. Indicated at the lower right-hand corner of each diagram is the number of cells analyzed and that of pupae from which the data were collected (in parentheses). Black arrows on the right indicate directions of LEC migration. Note that the green and black arrows point in the opposite directions, which supports the notion that βH-Spec is a landmark for the front-rear cell axis.

(**F1-H'**) Comparison of the subcellular distribution of βH-Spec^{GFSTF} in the control LECs (**F1-F4**) and *ds* knockdown LECs (**G1-H'**). LECs of the both genotypes expressed βH-Spec^{GFSTF} (**F1** and **G1**) and a membrane marker mCherry:CAAX (**F2** and **G2**). (**F3**, **G3**, and **H'**) mCherry:CAAX signals were used to trace cell boundaries (gray lines) and the front-rear cell axis of each LEC is indicated (arrowheads) as described above. Angular

distributions of the cell axis were calculated and plotted on rose diagrams (**F4** and **G4**). Detailed explanations of the rose diagrams are in the legend above. (**H**) A bigger image including **G1** and spanning the adjacent segment. (**H'**) Tracings of cell boundaries and cell axes. The brightness of **H** is increased than that in **G1** to highlight weaker signals of β_H-Spec^{GFSTF}. Magenta bars: estimated positions of the posterior compartment. Misoriented LECs are found in the anterior compartment and they are most likely LECs that depend on Ds for their posterior migration (Ds-dependent LECs; see Figure 7**I**). Scale bars: 30 µm.
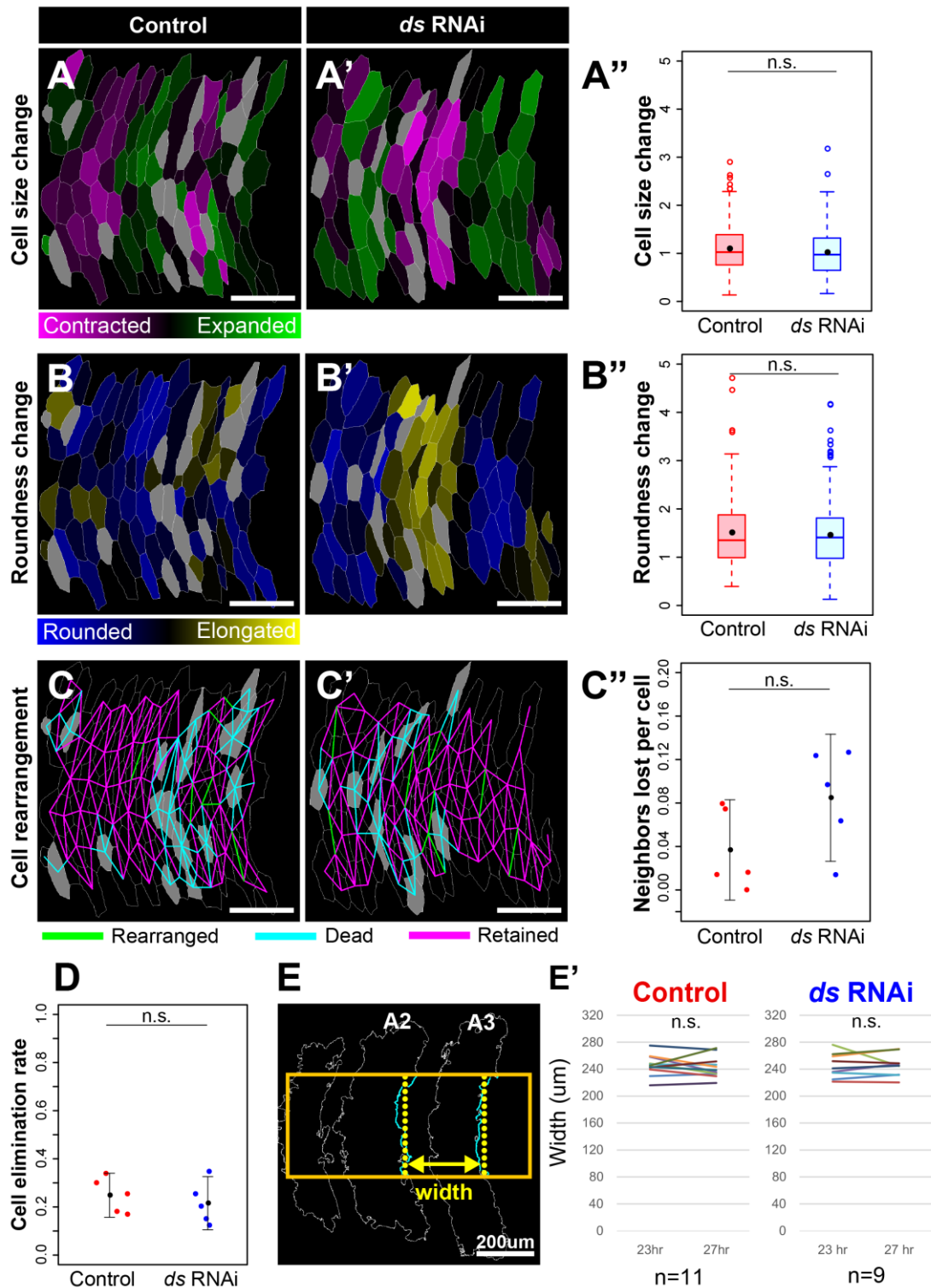
Figure S4. Effects of *ds* knockdown on changes of the cell size and roundness, cell rearrangement, apoptosis, and the segment width during the posterior-migration phase (Related to Figure 1).

(**A-D**) Cell size change (**A-A"**), roundness change of LECs (**B-B"**), cell rearrangement (**C-C"**), and occurrence of apoptosis (cell elimination rate in **D**) during the posterior-migration phase (23-27hr APF, see STAR methods for details). Images are cell-boundary tracings of LECs at 23 hr APF for which the results of the data analysis are merged. Gray cells died during the recordings. (**A-A"**) Magenta LECs contracted while green LECs expanded between 23 and 27 hr APF. (**A"**) Data of the cell size change are presented as a box-and-whisker plot with the mean (black dots). n (LECs)= 259 (5 control pupae) and 307 (5 *ds* knockdown pupae). (**B-B"**) Blue LECs became less elongated while yellow LECs became elongated between the two time points. (**B"**) Box-and-whisker plot of the ratio of the roundness change of each LEC. n (LECs)= 259 (5 control pupae) and 307 (5 *ds* knockdown pupae). (**C-C"**) Adjacent LECs whose cell centers are connected by magenta lines retained adjacent relationships, while others lost the neighbor relationship by cell death (cyan) or by cell rearrangements (green). (**C"**) Data of neighbors lost per cell are presented as a dot plot with the mean (black dots) ± 95% CI. n (pupae)= 5 (control) and 5 (*ds* knockdown). The values of neighbors lost per cell during the posterior migration of LECs are far smaller than those during the germ band extension of the Drosophila embryo (about 2.0 in 30 minutes; Paré et al., 2014) and those during the deformation of the notum (0.03-0.08 in 1 hr; data not shown). (**D**) Data for the cell elimination rate are presented as a dot plot with the mean (black dots) ± 95% CI. n (pupae)= 5 (control) and 5 (*ds* knockdown). (**A"**, **B"**, **C"**, and **D**) Wilcoxon rank sum test. n.s.: not significant.

(**E** and **E'**) Segment widths (distance between the yellow dotted lines in **E**) did not significantly change between the two time points indicated, whether *ds* was knocked down or not (**E'**; n.s.: paired t-test).
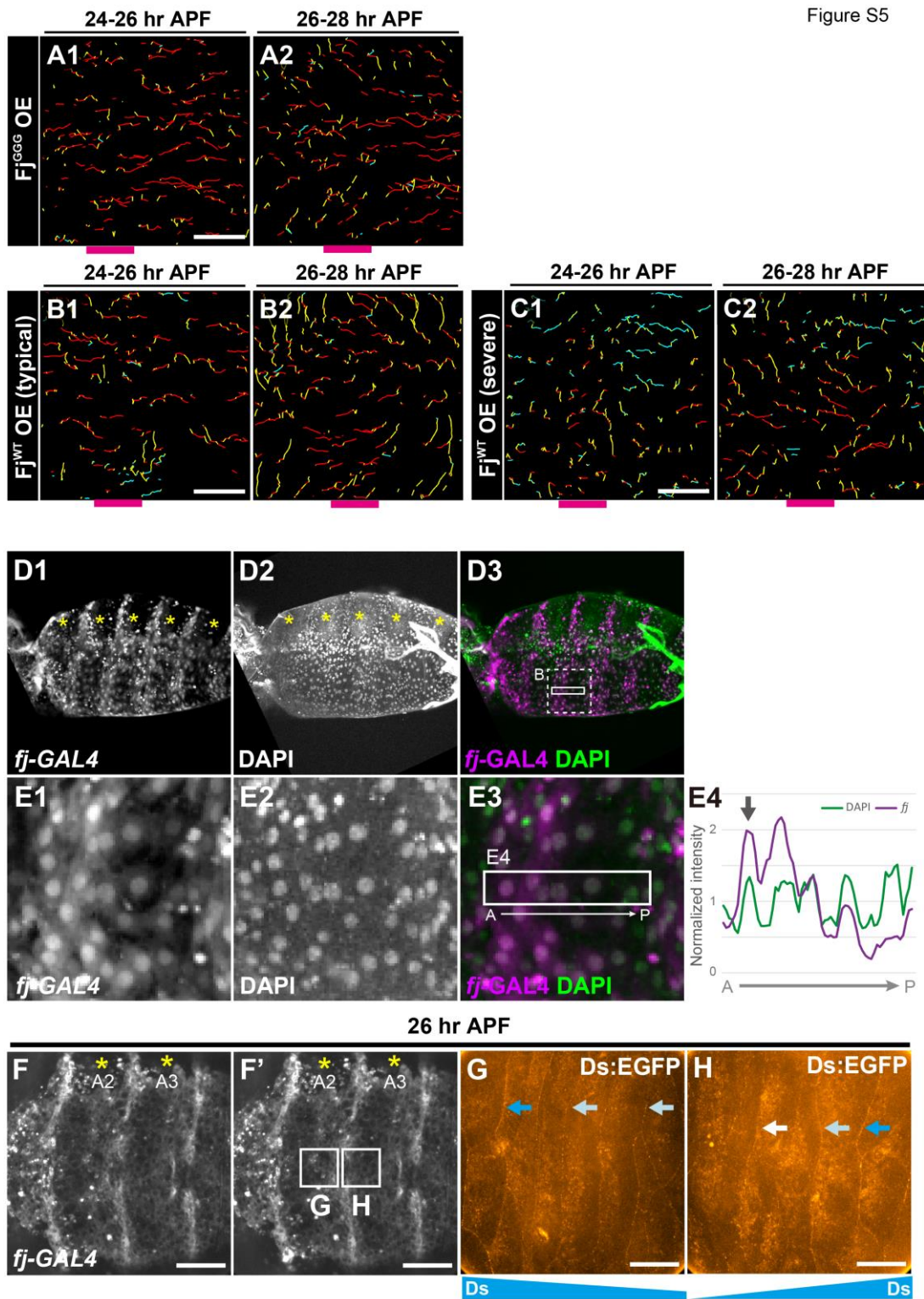
Figure S5. Effects of Fj overexpression on LEC migration and a difference of the *fj* expression level between LECs along the A-P axis (Related to Figure 3 and 4).

(**A-C**) The overexpression of Fj^{GGG}:mCherry hardly affected posterior movements of LECs (**A1-A2**; compare with Figure 1**C2-C3**). In contrast, that of Fj^{WT}:mCherry made the movement less biased (**B1-C2**). The data from two Fj^{WT}:mCherry-expressing pupae are shown: a pupae exhibiting a typical phenotype (**B1-B2**) and another giving the most severe defect (**C1-C2**; the data point marked by an arrowhead in Figure **3E**). See detailed explanations of markings in the legend of Figure 1**B**-1**D**.

(**D1-E4**) A 24 hr APF pupa was labeled for *fj* expression (**D1** and **E1**; magenta in **D3** and **E3**, *fj[VG1]>EGFP*) and for nuclei by using DAPI (**D2** and **E2**; green in **D3** and **E3**). A region highlighted by a dotted box is enlarged in **E1-E3**. (**E4**) Intensities of EGFP and DAPI signals along the A-P axis were quantified by applying "plot profile" in ImageJ to a rectangular ROI (a white box in **E3**). Their intensities were normalized by the average intensity of EGFP or DAPI within the ROI, and resultant normalized intensities were plotted against the distance along the A-P axis. Each peak (an arrow indicates a peak) corresponds to individual nuclei.

(**F-H**) LECs expressing mCherry:CAAX under the control of *fj-GAL4* and Ds:EGFP at 26 hr APF (**F** and **F'**; the same images). Yellow asterisks mark histoblast nests. Note that *fj-GAL4* positive LECs lie between histoblast nests, which suggests that the *fj* peak is around the segment border. We also noticed that the *fj* expression pattern changed temporally. *fj* expression was tightly restricted along the segment borders at 18 hr APF (data not shown), but later became broader and lower along the A-P axis (**F**). High-magnification images of the boxed regions in **F'** are shown in **G** and **H**. Note that Ds:EGFP signals at cell boundaries are high in LECs where *fj* expression level is low and vice versa, which suggests that Fj and Ds have counter-gradients.

Scale bars: 200 µm (**F** and **F'**), 100 µm (**A1-C2**) and 30 µm (**G** and **H**)

Figure S6

85
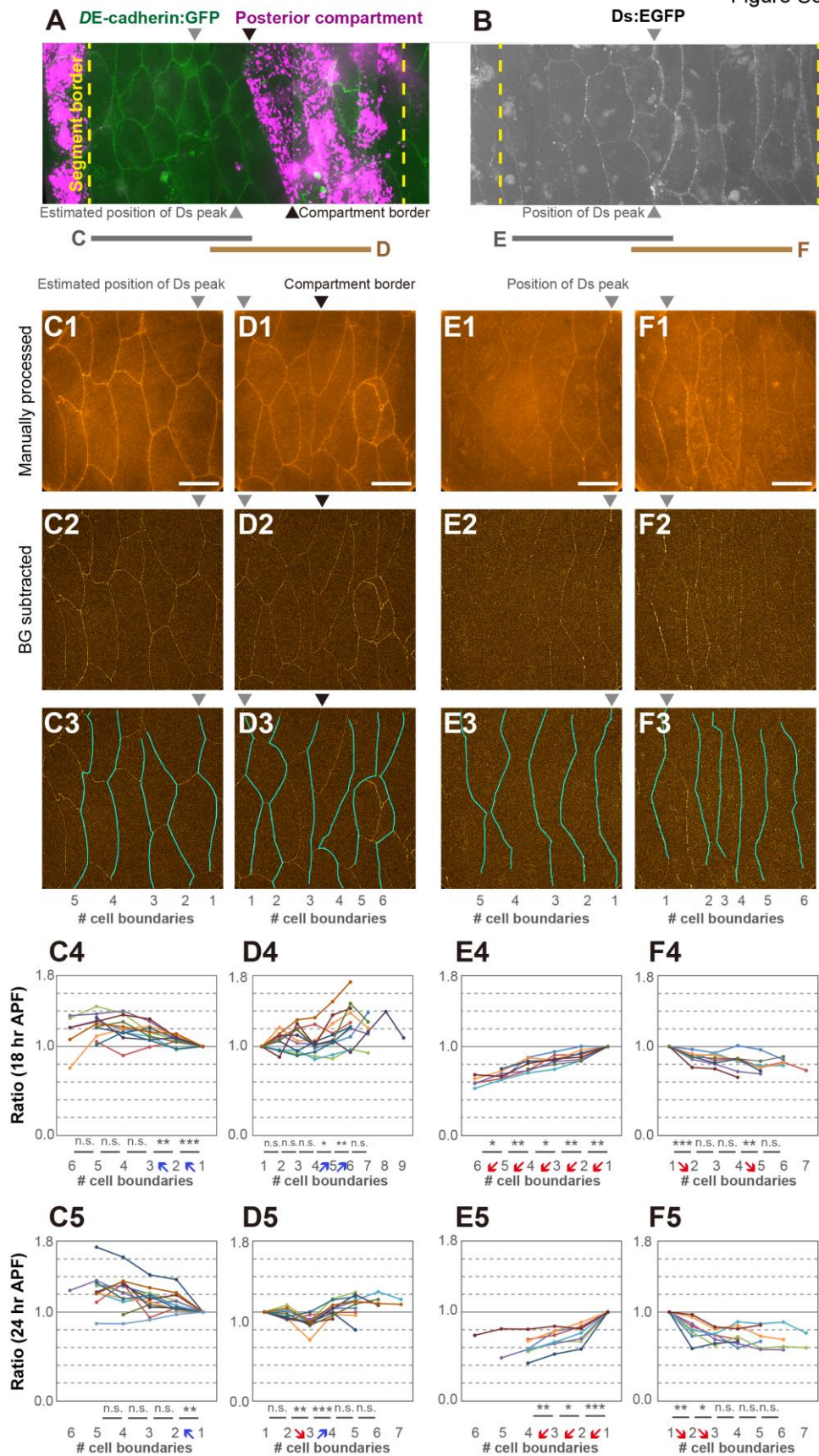
Figure S6. Amounts of Ds or *D*E-cadherin at cell boundaries along the A-P axis within each abdominal segment (Related to Figure 4).

(**A** and **B**) An image of an abdominal segment of the *D*E-cadherin:GFP (green in **A**) or *ds:EGFP* (**B**) knock-in strain at 26 hr APF, which was made by connecting four images along the A-P axis. Posterior compartments (*en-Gal4* positive cells) were labeled with magenta in **A**. We have shown in Figure 4**E**-4**E'** that the amount of Ds at cell boundaries is peaked at cell boundaries one to two cells anterior (marked with gray arrowheads hereafter) to the A/P compartment border (marked with black arrowheads hereafter) in each abdominal segment. Yellow dotted lines: positions of the segment borders.

(**C-F**) LECs of distinct regions that are underlined in **A** and **B** at 24 hr APF. Images of *D*E-cadherin:GFP (**C1-C5** and **D1-D5**) or Ds:EGFP (**E1-E5** and **F1-F5**). (**C1**, **D1**, **E1** and **F1**) To highlight signals at cell boundaries, signals of autofluorescence and *D*E-cadherin:GFP or Ds:EGFP from more basal planes were manually subtracted from maximum-intensity projections. (**C2**, **D2**, **E2** and **F2**) From images of **C1**, **D1**, **E1** and **F1**, respectively, backgrounds were subtracted by applying "Subtract Background" in ImageJ to 16 bit images (Rolling Ball Radius: 5 pixels).

(**C3**, **D3**, **E3** and **F3**) **C3**, **D3**, **E3**, and **F3** are duplicates of panels **C2**, **D2**, **E2** and **F2**, respectively, except for that *D*E-cadherin:GFP or Ds:EGFP signals at A-P cell boundaries were traced by the cyan lines. We were able to identify the junctions that are labeled with very weak Ds:EGFP signals, by using original images of individual optical sections prior to image processing (background subtraction) and/or maximum-intensity projections. The average intensity per pixel on each line was calculated (labeled with # cell boundaries at the bottom of each panel), those values were normalized against those on the Ds-peak boundaries (marked with gray arrowheads; cell boundaries #1 in **C3-F5**), and normalized values in the underlined regions in **A** and **B** were plotted on line graphs (**C4-F5**; see details in STAR methods).

(**C4-F5**) Data from different pupae at 18 hr APF (**C4**, **D4**, **E4** and **F4**) or 24 hr APF (**C5**, **D5**, **E5** and **F5**) are color coded in each graph. Imbalance was statistically tested between indicated cell boundaries (paired t-test; ***: p<0.001, **: p<0.01, *: p<0.05, n.s.: not significant). n = 12 (**C4**), 12 (**D4**), 8 (**E4**), 8 (**F4**), 13 (**C5**), 12 (**D5**), 8 (**E5**) and 8 (**F5**) pupae. Note that the statistically significant imbalance of Ds was detected over a wider range in the anterior compartment, where the LEC migration depends on Ds, than in the

posterior compartment (**E4-F4** and **E5-F5**), while such imbalances are not seen for *D*E-cadherin:GFP (e.g. compare **C5** and **E5**). Red down or blue up arrows illustrate the statistically significant imbalance of Ds:EGFP or *D*E-cadherin:GFP.

To verify the Ds imbalance, it is ideal to perform two-color imaging by co-expressing Ds:EGFP and a red fluorescent protein-tagged membrane marker in the same larvae and normalize the Ds:EGFP signal at cell boundaries. To search for such an appropriate red marker, we imaged *D*E-cadherin:mTomato, *D*E-cadherin:mCherry, and Bazooka:mCherry. Unfortunately all of them showed strong punctate signals in the cytosol, which made normalization impractical (e.g. Figure S3**C2** and **D2**; data not shown). Therefore we have used *D*E-cadherin:GFP for quantitative comparison with Ds:EGFP.

Scale bars: 30 µm.
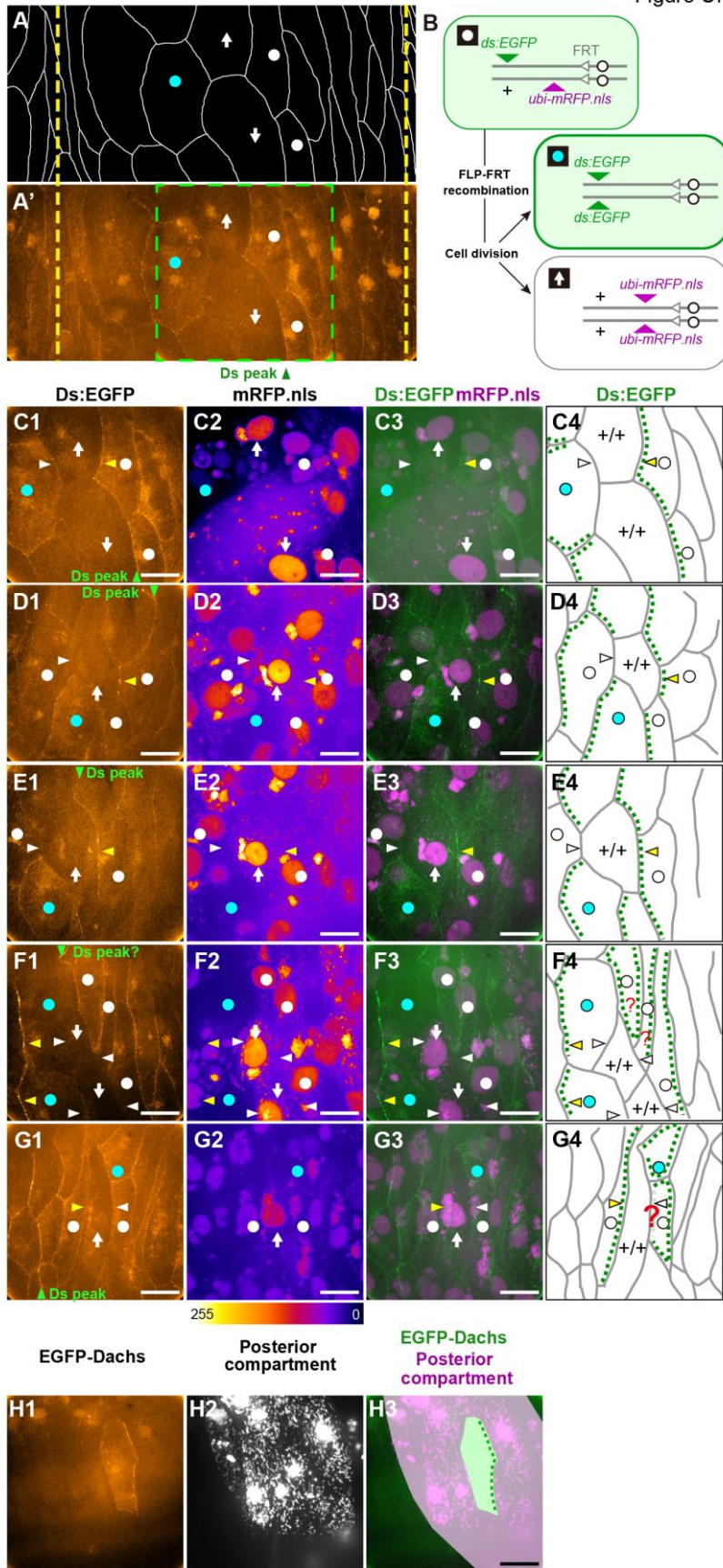
Figure S7

Figure S7. Localization of Ds and Dachs myosin in LECs anterior and posterior to the Ds-peak cells (Related to Figure 2, 4, 6, and 7).

(**A-G4**) Mosaic analysis of posteriorly-migrating LECs, to determine in which cell boundary Ds is preferentially located. Data (**A**, **A'**, and **C1-G4**) and the schema of the mosaic analysis (**B**).

(**A-A'**) Cell boundaries of LECs were traced manually and are demarcated by white lines. (**A'**) The original image of **A** that was made by connecting three consecutive images along the A-P axis. The genotype of the pupa is essentially heterozygous for both *ds:EGFP* (expressing Ds:EGFP under the control of the endogenous *ds* promoter) and *ubi-mRFP.nls* (expressing nuclear targeted mRFP under the control of the *ubiquitin* promoter), and two cells of this genotype are marked with white dots. Mitotic recombination between the two chromosomes generated LECs expressing only non-EGFP Ds (white arrows) and adjacent LECs expressing only Ds:EGFP (cyan dot; see **B** for detailed genotypes of marked LECs and more details in STAR methods). Yellow dotted lines represent approximate positions of segment borders; and green arrowheads identify peak amounts of Ds within the segments. The green-boxed region in **A'** is highlighted in **C1-C4**.

(**B**) Schematic representation of the mosaic analysis (Brittle et al., 2012). FLP-FRT recombination in a cell heterozygous for both *ds:EGFP* and *ubi-mRFP.nls* (white dot) yields two different types of cells; one harbors two copies of *ds:EGFP* only (cyan dot), and the other has two copies of *ubi-mRFP.nls* only (white arrow). Epidermal cells divide only a few times at the embryonic stage (three times on average) and never afterwards (Vincent and O'Farrell, 1992). In addition, precise quantitative evaluation of the subcellular localization of Ds:EGFP was possible only when the mosaic clones were generated within the regions of one-two cell width on both sides of the Ds peak (green arrowheads), otherwise the Ds:EGFP signal is too dim to quantify (e.g., see Figure 4**D'**). Therefore, it is technically challenging to collect a large number of appropriate samples. Nevertheless some of our clones would be at least visually suggestive of the localization (**A-G4**).

(**C1-G4**) Ds:EGFP (**C1**, **D1**, **E1**, **F1**, **G1**, and green in the merged images), mRFP.nls (**C2**, **D2**, **E2**, **F2**, **G2**, and magenta in the merged images), and interpretations of the Ds:EGFP localization (dotted green lines in **C4, D4, E4, F4,** and **G4**). (**C1-C4**) Between the LECs at the Ds peak (white dots) and their anterior adjacent LECs that had no copy of *ds:EGFP*

(white arrows), cell boundaries were rich in Ds:EGFP (yellow arrowhead). On the other hand, cell boundaries were negative for Ds:EGFP (white arrowhead) between LECs that lacked *ds:EGFP* (white arrows) and anterior adjacent LECs that had two copies of *ds:EGFP* (cyan dot). The Ds:EGFP localization in individual LECs is illustrated as in **C4**. In LECs anterior to the Ds peak (green arrowheads), Ds:EGFP seemed to be enriched at the anterior cell boundaries (other examples are shown in **D1**-**E4**). (**F1-G4**) Images of the region posterior to the Ds peak (**F1** and **G1**). Here, Ds:EGFP seemed to be enriched more at the posterior cell boundary as illustrated in **F4**, but it was difficult to make a conclusion (? in **F1** and **G1**). These data were obtained from different pupae. These findings in LECs are consistent with what has been shown along the proximal-distal axis in the wing disc of third instar larvae, which generates a Ds slope with proximal high and distal low abundance, and Ds subcellularly localized at the distal cell boundaries (Brittle et al. 2012).

(**H1**-**H3**) EGFP-Dachs (**H1**; green in **H3**) was clonally expressed in LECs, imaged at 24 hr APF, and merged with a marker for the posterior compartments (*en-GAL4, UAS-mmRFP*; **H2**; magenta in **H3**). Note that EGFP-Dachs was polarized at the posterior cell edge in the posterior compartments. See also Figure 4**H1**-**H3**. Scale bars: 30 µm.